STRUCTURE FUNCTIONS IN NEUTRINO AND ANTINEUTRINO NEON INTERACTIONS IN BEBC

Kevin Ernest Varvell

Wolfson College

A thesis submitted for the degree of Doctor of Philosophy at the University of Oxford

Nuclear Physics Laboratory, Oxford. September 1985.

Structure Functions in Neutrino and Antineutrino Neon Interactions in BEBC

K.E. Varvell
Wolfson College, University of Oxford

Submitted for the Degree of Doctor of Philosophy, September 1985

ABSTRACT OF THESIS

A study of data from the WA59 experiment at CERN is presented, in which the Big European Bubble Chamber (BEBC) filled with a 75% molar liquid Neon/Hydrogen mixture was exposed to the Wide Band neutrino and antineutrino beams derived from the Super Proton Synchrotron (SPS).

The total neutrino and antineutrino cross sections per unit neutrino energy for charged current (CC) scattering from an isoscalar target were calculated for the energy range $10 < E < 300$ GeV, and found to be

$$\sigma^{\nu}/E = (.609 \pm .008(stat.) \pm .044(syst.)) \times 10^{-38} cm^2/GeV$$
$$\sigma^{\overline{\nu}}/E = (.307 \pm .003(stat.) \pm .025(syst.)) \times 10^{-38} cm^2/GeV$$

The cross sections were found to be consistent with a linear rise with increasing neutrino (antineutrino) energy E, as predicted by the simple quark-parton model of nucleon structure.

The differential cross sections for neutrino and antineutrino charged current scattering were used to calculate the isoscalar nucleon structure functions F_2 and xF_3 as functions of the kinematical variables Bjorken x and Q^2, the square of the 4-momentum transfer from the lepton to hadron system. Deviations from the simple quark-parton model prediction of scaling were observed, taking the qualitative form predicted by the currently accepted theory of the strong interaction, Quantum Chromodynamics (QCD). The structure functions were compared with previous measurements and found to be in good agreement.

The possibility of utilising the measured values of F_2 and xF_3 for quantitative tests of QCD was investigated. On the assumption of perturbative QCD as the sole cause of scaling violation for $Q^2 > 2$ GeV^2/c^2, the evolution equation technique was applied in next-to-leading order to the non-singlet structure function xF_3, and to xF_3 in combination with the singlet structure function F_2. The sensitivity of the procedure to systematic effects in the extraction of the structure functions was investigated. On the basis of the singlet fits, the data can be described by perturbative QCD with a value of $\Lambda_{\overline{MS}}$, the parameter setting the level of scaling violation, of 92±51 MeV/c. Non-singlet fits alone to the present data cannot discriminate between this value of $\Lambda_{\overline{MS}}$ and higher values of the order 400-500 MeV/c.

ACKNOWLEDGMENTS

I am very grateful to my supervisor, John Wells, for his encouragement and guidance through 3 years at Oxford, and for his continued interest in the whereabouts of this thesis after that.

I wish to thank Professors Don Perkins and Ken Allen for the hospitality of the Nuclear Physics Laboratory, and all the members of the Neutrino Group under Gerald Myatt for a pleasant working atmosphere. Special thanks go to Gino Saitta for an untiring willingness to help budding programmers/physicists, and for much friendship and good humour, and to Gerard Corrigan, with whom I shared an office and countless fruitful discussions.

Willie Black, Nick West and Carrie Story know all there is to know about the DEC10 and programming in general, and I thank them for letting some of that knowledge rub off on a frequent visitor to their offices. Thanks also to the scanning, technical and secretarial staff of the Nuclear Physics Laboratory, and to the incomparable tea ladies.

It has been very enjoyable working in the WA59 collaboration and I thank Wilbur Venus and the rest of WA59 for being such a good bunch academically and otherwise. Particular thanks go to Mandy Cooper-Sarkar, Wilbur, Andy Parker and Andrew Sansum, who also worry about structure functions and have been a delight to work with.

I would like to thank Dick Roberts at the Rutherford Laboratory for making available his evolution equation programme, and Peter Kasper for the challenge of his Monte Carlo.

Thanks are due to the many friends made at Oxford who contributed much to an enjoyable stay. In this regard I would like to thank Gerard Corrigan (again) and Jennie Lynch for more friendship and support than I can ever hope to repay.

For 3 years at Oxford I was supported by a University of Western Australia Hackett Overseas Studentship, without which I would be thanking none of the above.

CONTENTS

Chapter 1

INTRODUCTION

1.1 A BRIEF OVERVIEW

Neutrino experiments in the West Area at CERN, utilising beams drawn from the Super Proton Synchrotron (SPS), have been performed since 1977. The present work is concerned with one such experiment, denoted WA59, involving an exposure of the Big European Bubble Chamber (BEBC) filled with a mixture of liquid neon and hydrogen to the "wideband" neutrino and antineutrino beams.

One of the motivations for experiments of this type is the investigation of the underlying structure of nucleons and the nature of the strong interaction. Leptons provide a convenient probe of the nucleon, possessing no structure themselves and interacting only weakly in the case of neutrinos and weakly and electromagnetically in the case of electrons and muons. Both types of interaction are now believed well understood in terms of the standard model of Weinberg, Salam and Glashow [1]. In the case of the strong interaction, however, the situation is not as clear. Outstanding success in describing the structure of the nucleon has been obtained with the Quark-Parton Model [2], much of this success being through the predictions of this model for the form of the nucleon structure functions measured in lepton-nucleon scattering experiments. A candidate theory describing the interactions between quarks now exists, known as Quantum Chromodynamics (QCD). At

present, however, it is difficult to make clean predictions with QCD which can be readily tested by experiment. It is hoped that by the accurate measurement of nucleon structure functions over as large a kinematic domain as possible some attempt at the verification of the predictions of QCD may be made.

The present analysis is concerned with such a measurement of structure functions. The reactions considered are the inclusive scattering of neutrinos and antineutrinos by nucleons

$$\begin{aligned} \nu N &\rightarrow \mu^- X \\ \bar{\nu} N &\rightarrow \mu^+ X \end{aligned} \tag{1.1}$$

where N denotes a nucleon (proton or neutron) and X a final state consisting in general of highly excited hadronic matter. Such reactions are denoted as Charged Current (CC) interactions. Previous studies of the above reactions have been performed at CERN in an exposure of BEBC to the SPS Narrow Band neutrino beam in combination with low energy data from the GARGAMELLE bubble chamber exposed to the PS neutrino beam [3], and also in the GARGAMELLE chamber following its move to the SPS beam [4]. The WA59 experiment was performed with the intention of measuring structure functions over a wide kinematic domain with a substantial increase in statistics. The systematics of combining data from different experiments is not present in the current analysis. Other measurements have been performed by the high statistics counter experiments of the CDHS[1][5] and CHARM[2][6] collaborations in the West Area at CERN, and the CCFRR[3][7] collaboration at Fermilab. The kinematic regimes covered by these experiments do not correspond exactly to those of WA59, however, enabling the present measurements to make a contribution to the body of data on structure functions.

The layout of this thesis is as follows. In the remainder of this chapter, a summary of those aspects of neutrino-nucleon scattering of interest in the context of structure functions will be given. An introduction to the kinematics, and an outline of the derivation of the scattering cross section in terms of the structure functions $2xF_1$, F_2 and xF_3 will be

[1] CERN-Dortmund-Heidelberg-Saclay
[2] CERN-Hamburg-Amsterdam-Rome-Moscow
[3] Caltech-Columbia-Fermilab-Rochester-Rockefeller

found in Section 1.2. The Quark-Parton Model, so successful in describing many aspects of lepton-nucleon scattering, is the subject of Section 1.3. A brief outline of Quantum Chromodynamics will be given in Section 1.4, along with possible means of testing it with neutrino scattering data. In Section 1.5 the choice of scaling variable with which to analyse the data will be considered. Section 1.6 contains a note on the effect on the structure functions of measurements on a complex nucleus, important in the light of recent experimental results.

Chapter 2 will describe the experimental details, production of a neutrino beam, the bubble chamber and muon detection system, and the processing chain necessary to obtain a data set suitable for analysis. In Chapter 3 the treatment of this data set to produce an unbiased set of charged current events correctly distributed in chosen kinematic variables will be dealt with. Using this set of events, total cross sections for neutrino and antineutrino scattering are calculated in Chapter 4. Chapter 5 is concerned with the extraction of the structure functions F_2 and xF_3 over the available kinematic plane, and comparison of these structure functions with other measurements. Quantities of interest related to F_2 and xF_3, the structure function integrals and quark and antiquark densities, are presented in Chapter 6, along with a preliminary study of the evolution of the structure functions with Q^2. Chapter 7 is a discussion of the results of the analysis as a whole and a few thoughts for the future.

1.2 NEUTRINO SCATTERING FROM A NUCLEON TARGET

In the Standard Model of Weinberg, Salam and Glashow, the charged current reactions of equation (1.1) may be considered to proceed via the exchange of a single virtual charged intermediate vector boson. This process is represented by the Feynman diagram of Fig. 1.1. In this figure, $k = (E, \mathbf{k})$ represents the 4-momentum of the incident neutrino (antineutrino), $k' = (E', \mathbf{k}')$ that of the outgoing muon, and $p = (m, 0)$, $p' = (E_h, \mathbf{p_h})$ and $q = (q_o, \mathbf{q})$ the 4-momenta of the target nucleon, hadron final state and exchanged boson respectively, in the laboratory frame. m is the nucleon mass.

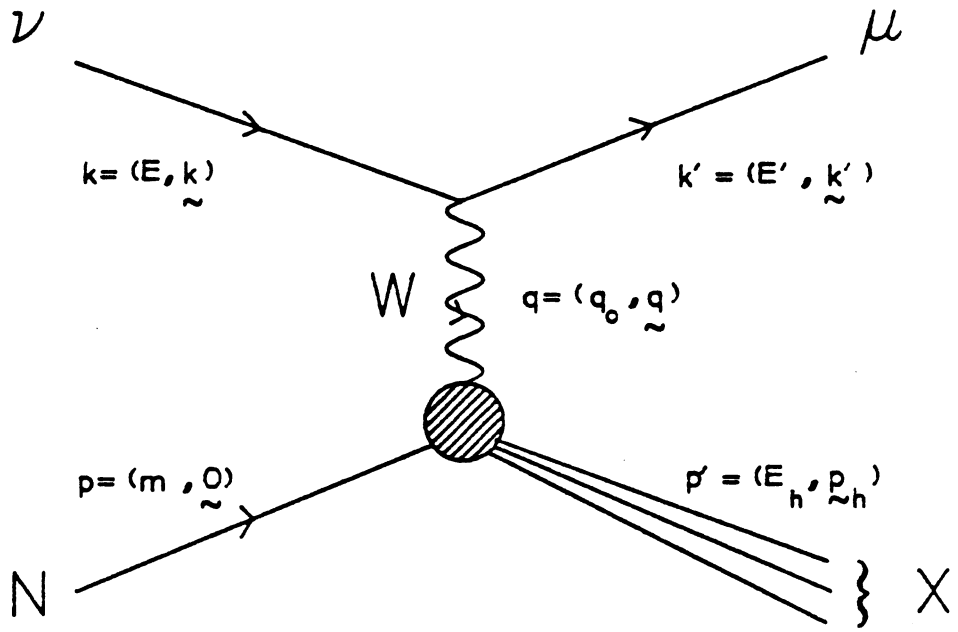

FIG 1.1 FEYNMAN DIAGRAM FOR NEUTRINO NUCLEON CHARGED CURRENT SCATTERING

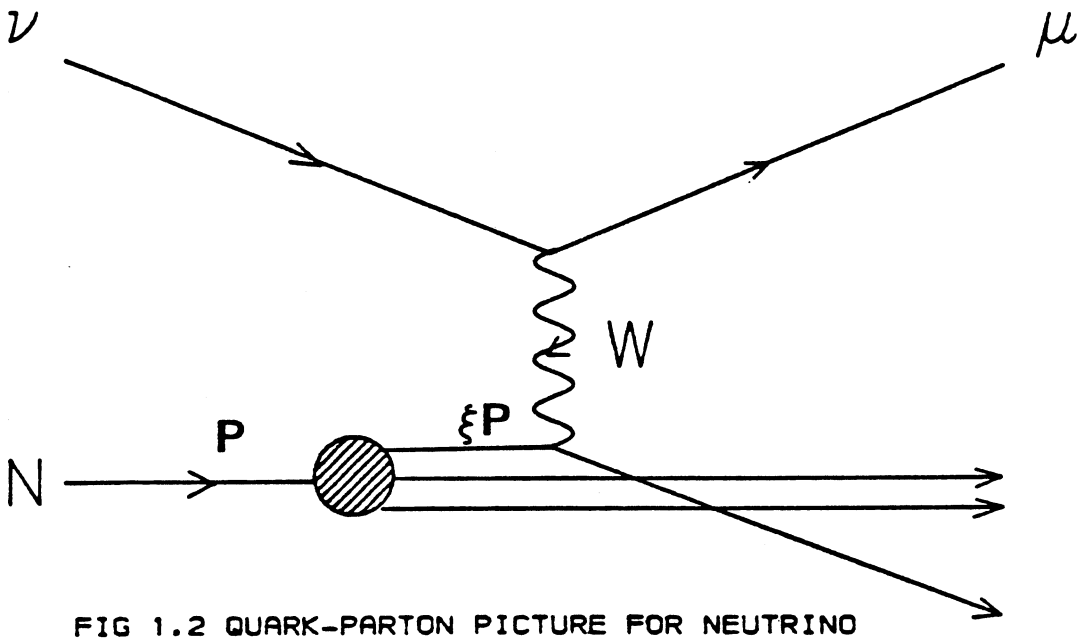

FIG 1.2 QUARK-PARTON PICTURE FOR NEUTRINO NUCLEON CHARGED CURRENT INTERACTION

The cross section for neutrino-nucleon scattering, written in terms of the energy E' of the outgoing muon and the angle θ between the muon and the incoming neutrino, is given by [8]

$$\frac{d^2\sigma}{d\Omega dE'} = \frac{G^2}{(2\pi)^2}\left(\frac{{m_W}^2}{{m_W}^2 - q^2}\right)^2 \frac{E'}{E} L_{\mu\nu} W^{\mu\nu} \tag{1.2}$$

where G is the Fermi coupling constant and m_W the W boson mass. $L_{\mu\nu}$ is the lepton tensor and is explicitly calculable from the neutrino-muon vertex, having the form

$$L_{\mu\nu} = k_\mu k'_\nu + k'_\mu k_\nu - g_{\mu\nu} k.k' \pm i\epsilon_{\mu\nu\lambda\sigma} k^\lambda k'^\sigma \tag{1.3}$$

where the + sign refers to neutrino scattering and the − sign to antineutrino scattering.

The hadronic tensor $W^{\mu\nu}$, involving the final state X, cannot be calculated from first principles due to our ignorance of the dynamics of bound state hadronic systems. A general form for $W^{\mu\nu}$ may be written in terms of tensors constructed from the target and current 4-vectors

$$W^{\mu\nu} = W_1 g^{\mu\nu} + \frac{W_2}{m} p^\mu p^\nu - i\frac{W_3}{2m^2}\epsilon^{\mu\nu\alpha\beta} p_\alpha q_\beta + W_4 \frac{q^\mu q^\nu}{m^2} + \frac{W_5}{m^2}(p^\mu q^\nu + q^\mu p^\nu) + i\frac{W_6}{2m^2}(p^\mu q^\nu - q^\mu p^\nu) \tag{1.4}$$

W_1 to W_6 are structure functions, which contain information on the strong interaction dynamics of the target. They are functions of the independent Lorentz scalars p.q, q.q. In the energy region pertaining to the present experiment, terms proportional to the muon mass may be safely neglected. This effectively eliminates the structure functions W_4, W_5 and W_6 upon forming the contraction $L_{\mu\nu}W^{\mu\nu}$, leaving the expression for the differential cross section in terms of W_1, W_2 and W_3 as follows

$$\frac{d^2\sigma}{d\Omega dE'} = \frac{G^2}{2\pi^2} E'^2 \left(\frac{{m_W}^2}{{m_W}^2 - q^2}\right)^2 \left\{2W_1 \sin^2\frac{\theta}{2} + W_2 \cos^2\frac{\theta}{2} \pm W_3 \left(\frac{E+E'}{m}\right)\sin^2\frac{\theta}{2}\right\} \tag{1.5}$$

The term involving W_3 reflects parity violation in weak interactions and is not present in electron or muon scattering from a nucleon target.

Before proceeding it will be necessary to define the kinematic variables in terms of which lepton-nucleon scattering is generally discussed. The following Lorentz scalars are commonly defined

$$\nu = \frac{p.q}{m} \tag{1.6}$$

$$Q^2 = -q.q > 0 \tag{1.7}$$

In the laboratory frame ν is simply the energy transfer $E - E'$ from the neutrino to the muon, and Q^2 is given by

$$Q^2 = 4EE' \sin^2 \frac{\theta}{2} \tag{1.8}$$

Two further variables encountered are

$$x = \frac{Q^2}{2m\nu} \tag{1.9}$$

$$y = \frac{\nu}{E} \tag{1.10}$$

x is the Bjorken scaling variable [9] central to the quark-parton model to be discussed in the following section. The invariant mass squared of the hadronic system is given by

$$W^2 = m^2 + Q^2 \left(\frac{1}{x} - 1\right) \tag{1.11}$$

Relations between the structure functions may be obtained by considering the scattering process in terms of the absorption cross sections for right-handed, left-handed and scalar W bosons, σ_R, σ_L and σ_S. In terms of these quantities W_1, W_2 and W_3 may be written

$$\begin{aligned} W_1 &= \frac{K}{\pi G\sqrt{2}}(\sigma_R + \sigma_L) \\ W_2 &= \frac{K}{\pi G\sqrt{2}} \left(\frac{Q^2}{Q^2 + \nu^2}\right) (\sigma_R + \sigma_L + 2\sigma_S) \\ W_3 &= \frac{K}{\pi G\sqrt{2}} \left(\frac{2m}{\sqrt{\nu^2 + Q^2}}\right) (\sigma_R - \sigma_L) \end{aligned} \tag{1.12}$$

where K is a flux factor.

The requirement that the cross sections σ_R, σ_L and σ_S be non-negative leads to the so-called "positivity constraints" [10]

$$0 \leq \frac{1}{2m}\sqrt{\nu^2 + Q^2}|W_3| \leq W_1 \leq \left(1 + \frac{\nu^2}{Q^2}\right) W_2 \tag{1.13}$$

If the structure functions W_1, W_2 and W_3 are redefined through the relations

$$\begin{aligned} W_1 &= F_1 \\ \frac{\nu W_2}{m} &= F_2 \\ \frac{\nu W_3}{m} &= F_3 \end{aligned} \tag{1.14}$$

the following commonly encountered form for the differential cross section is obtained in terms of x and y

$$\frac{d^2\sigma^{\nu,\bar{\nu}}}{dxdy} = \frac{G^2 mE}{\pi}\left(\frac{{m_W}^2}{{m_W}^2+Q^2}\right)^2 \left\{2xF_1^{\nu,\bar{\nu}}(x,Q^2)\frac{y^2}{2} + F_2^{\nu,\bar{\nu}}(x,Q^2)\left(1-y-\frac{mxy}{2E}\right) \pm xF_3^{\nu,\bar{\nu}}(x,Q^2)y\left(1-\frac{y}{2}\right)\right\} \tag{1.15}$$

The introduction of the superscripts ν, $\bar{\nu}$ emphasises that the structure functions will be different for neutrino-nucleon and antineutrino-nucleon scattering, and the explicit dependence of the structure functions on the variables x and Q^2 is shown.

The discussion to this point has not taken into account the identity of the target nucleon. In the present experiment the neon-hydrogen mixture provides an essentially "isoscalar" target consisting of equal numbers of protons and neutrons. In principle we must therefore consider a total of twelve structure functions, three for each of the initial systems νp, νn, $\bar{\nu}p$, $\bar{\nu}n$. In practice, it is usual to view the nucleons in terms of quarks (which we will consider in the following section), in which case by neglecting the strange (and charmed) sea we have the charge symmetry conditions

$$\begin{aligned} F_i^{\bar{\nu}p} &= F_i^{\nu n} \\ F_i^{\nu p} &= F_i^{\bar{\nu} n} \end{aligned} \tag{1.16}$$

where i = 1,2,3. Forming the cross section for scattering from an isoscalar target

$$\frac{d^2\sigma^{\nu,\bar{\nu}I}}{dxdy} = \frac{1}{2}\left(\frac{d^2\sigma^{\nu,\bar{\nu}p}}{dxdy} + \frac{d^2\sigma^{\nu,\bar{\nu}n}}{dxdy}\right) \tag{1.17}$$

and defining

$$F_i^{\nu,\bar{\nu}I} = \frac{1}{2}\left(F_i^{\nu,\bar{\nu}p} + F_i^{\nu,\bar{\nu}n}\right) \quad i = 1,2,3 \tag{1.18}$$

we have, through (1.16), that

$$F_i^{\nu I} = F_i^{\bar{\nu} I} \tag{1.19}$$

In this approximation the number of independent structure functions reduces to three.

1.3 THE QUARK-PARTON MODEL

In Section 1.2, no assumptions as to the specific nature of the target nucleon were made until we wished to reduce the number of independent structure functions, in which case it was necessary to talk in terms of quarks. We will now consider the scattering process (1.1) in terms of the constituent model of the nucleon known as the quark-parton model. This model has enjoyed outstanding success in describing the phenomenology of lepton-nucleon scattering. What follows is a brief review of the essential features of the model, for a more detailed description the reader is referred to Feynman [2].

In the quark-parton model, neutrino-nucleon scattering occurs via the incoherent scattering, in the impulse approximation, of the W boson from pointlike spin 1/2 constituents of the nucleon. These constituents are taken to consist of 3 "valence" quarks, carrying the quantum numbers of the nucleon, and a "sea" of quark-antiquark pairs. The quark-parton picture of the scattering process is schematically represented in Fig. 1.2. The current q is absorbed by a single parton carrying a fraction ξ of the nucleon momentum. Considered in an "infinite momentum" Lorentz frame, one in which the transverse momentum of the partons is small in comparison with the longitudinal momentum, and in which quark and nucleon masses may be neglected, it can be shown that

$$\xi \simeq \frac{Q^2}{2m\nu} \equiv x \tag{1.20}$$

Thus Bjorken's x variable, in such an approximation, is a measure of the fractional momentum of the nucleon carried by the struck quark.

The quark-parton model makes several predictions which are in good general agreement with present data. As a consequence of the pointlike nature of the partons, Bjorken [9] predicted in 1969 the phenomenon of scaling, or the absence of a momentum scale entering into the description of the scattering process. In terms of the structure functions this implies that in the Bjorken limit $Q^2 \to \infty$, $\nu \to \infty$ such that x remains finite,

$$F_i(x, Q^2) \to F_i(x) \qquad i = 1, 2, 3 \tag{1.21}$$

Scaling is observed to hold in an approximate sense in all available lepton-nucleon scattering data, the small deviations from exact scaling being attributed to interactions between quarks, the subject of the next section. For the remainder of this section we will assume that scaling holds exactly.

If the scattering of neutrinos and antineutrinos from a nucleon target occurs entirely off spin 1/2 constituents, corresponding to the vanishing of the scalar W absorption cross section σ_S, it is found in the Bjorken limit that

$$2xF_1(x) = F_2(x) \tag{1.22}$$

This relation is known as the Callan-Gross relation [11] and will be important in the extraction of structure functions as discussed in Chapter 5.

As a consequence of scaling, it can be seen by integrating (1.15) over x and y that the total neutrino and antineutrino cross sections rise linearly with neutrino (antineutrino) energy. Averaging over all experiments gives the following values for the cross section per unit energy [12]

$$\begin{aligned} \sigma^{\nu}/E &= (0.63 \pm 0.02) \times 10^{-38} cm^2/GeV \\ \sigma^{\overline{\nu}}/E &= (0.30 \pm 0.01) \times 10^{-38} cm^2/GeV \end{aligned} \tag{1.23}$$

Values for these cross sections for the present experiment will be given in Chapter 4.

It is possible through the quark-parton model to obtain relations between the structure functions F_2 and xF_3 and the momentum distributions of quarks and antiquarks in the nucleon. Denoting the momentum distributions of up, down, strange and charmed quarks in the proton by $xu(x)$, $xd(x)$, $xs(x)$ and $xc(x)$ respectively, with similar notation for antiquarks, and defining the total quark and antiquark momentum distributions by

$$\begin{aligned} xq(x) &= x\{u(x) + d(x) + s(x) + c(x)\} \\ x\overline{q}(x) &= x\{\overline{u}(x) + \overline{d}(x) + \overline{s}(x) + \overline{c}(x)\} \end{aligned} \tag{1.24}$$

the differential cross section for neutrino and antineutrino scattering from an isoscalar target can be written (dropping the explicit functional dependence on x)

$$\begin{aligned} \frac{d^2\sigma^{\nu}}{dxdy} &= \frac{G^2 mE}{\pi}\left(\frac{{m_W}^2}{{m_W}^2 + Q^2}\right)^2 x\{[q + (s-c)] + (1-y)^2[\overline{q} - (\overline{s} - \overline{c})]\} \\ \frac{d^2\sigma^{\overline{\nu}}}{dxdy} &= \frac{G^2 mE}{\pi}\left(\frac{{m_W}^2}{{m_W}^2 + Q^2}\right)^2 x\{[\overline{q} + (\overline{s} - \overline{c})] + (1-y)^2[q - (s-c)]\} \end{aligned} \tag{1.25}$$

Assuming the Callan-Gross relation in (1.15), neglecting the term in $mxy/2E$ and comparing with (1.25) leads to the relations

$$\begin{aligned} F_2(x) &= x[q + \overline{q}] \\ xF_3(x) &= x[q - \overline{q}] \end{aligned} \tag{1.26}$$

From (1.26) it is clear that $xF_3(x)$ is a measure of the valence quark momentum distribution, since by writing $q(x) = q_v(x) + q_s(x)$ as the sum of valence and sea quark distributions we have $q_s(x) = \overline{q}(x)$. The Gross-Llewellyn-Smith sum rule [10] predicts the number of valence quarks in the nucleon

$$\int_0^1 \frac{xF_3(x)}{x} dx = 3 \tag{1.27}$$

which is consistent with measured values of this quantity [13]. The total momentum carried by quarks and antiquarks is given by

$$\int_0^1 F_2(x) dx$$

The naive quark-parton model would predict the value of 1 for this quantity, whilst experimental values are of order 0.5 [14]. Thus approximately one-half of the momentum of nucleons is carried by partons which do not feel the weak interactions. These partons are associated with the mediators of the strong force, gluons, to which the small deviations from scaling observed in deep inelastic lepton scattering are also attributed. We now turn our attention to these scaling deviations.

1.4 QUANTUM CHROMODYNAMICS

The naive quark-parton model of the preceding section treats the quark and antiquark constituents of the nucleon as essentially free (non-interacting) objects. In this section the dynamics of quark interactions will be briefly discussed. At present the favoured candidate for a theory of the strong interactions is the non-Abelian gauge field theory known as Quantum Chromodynamics, or QCD. The force between quarks is mediated by an octet of massless vector gluons which couple to the "colour" charge of quarks and antiquarks, in the same way that the electromagnetic force between charged particles is carried by the

massless vector photon in Quantum Electrodynamics (QED). In contrast to QED, however, the additional coupling of the gluon to itself, brought about by the gluons possessing colour charge (the photon in QED is uncharged) results in a different asymptotic behaviour of the theory. QCD predicts that the strength of the effective coupling between quarks and gluons, commonly expressed in terms of a "running" coupling constant $\alpha_s(Q^2)$, decreases with increasing Q^2, a phenomenon given the name "asymptotic freedom". Naively this means that in the limit of large Q^2 the size of the coupling constant becomes sufficiently small for perturbative calculations to become possible. The quark-parton model picture of non-interacting quarks is also given a qualitative basis at large Q^2 in terms of asymptotic freedom.

It is not appropriate here to discuss QCD at length, detailed reviews of the subject exist in the literature [15]. The following remarks are restricted to aspects relating to lepton-nucleon scattering and nucleon structure.

The pattern of scaling violation observed in neutrino-nucleon scattering data may be understood intuitively as follows. The presence of gluons within the nucleon suggests that as the Q^2 with which the nucleon is probed increases, it becomes possible to resolve a quark for example into a quark and a bremsstrahlung gluon. The 4-momentum fraction x of the struck quark will on average be lower in this case than at a lower Q^2 value (the quark having given up some of its 4-momentum to the radiated gluon). Thus the quark momentum distributions as a function of x, and consequently the structure functions, would be expected to soften as Q^2 increases. Stated another way, as a function of Q^2, the structure functions would be expected to rise with Q^2 at low x and decrease with Q^2 at high x. This behaviour is indeed observed in available electron-nucleon, muon-nucleon and neutrino-nucleon scattering data [16] [17] [3].

Quantitatively, perturbative QCD predicts that the departures from scaling in Q^2 will be logarithmic, with structure functions varying as $\ln(Q^2/\Lambda^2)$ where Λ sets the scale of the violation and is not predicted by the theory. Several approaches to the problem of confronting the QCD prediction for the form of the scaling violation with the available data have been adopted, dividing naturally into three methods.

In the simplest "moment" approach, the Cornwall-Norton [18] moments of structure functions are calculated from the measured structure functions, defined as follows

$$M_i^n(Q^2) = \int_0^1 x^{n-2} F_i(x, Q^2) dx \qquad n = 2, 3, ... \tag{1.28}$$

where $F_i = F_2$ or xF_3. QCD makes an explicit prediction for the form of these moments. In the case of the flavour "non-singlet" structure function xF_3, this takes the reasonably simple form

$$M_3^n(Q^2) = C/[\ln(Q^2/\Lambda^2)]^{d_n} \tag{1.29}$$

where C is a constant and the d_n are known as the "anomalous dimensions" and are calculable from the theory. In practice a more complicated form of the moments than (1.29) is generally used in order to account for so-called "target mass effects". This will be discussed in section 1.5.

A second approach to the problem is to attempt to find a functional form for the structure functions which fits the data over the x, Q^2 plane. The most commonly encountered parametrization of this type is that of Buras and Gaemers [19]. As an example, in this scheme valence quark distributions may be represented by the functional form

$$xF_3(x, Q^2) = \frac{3}{\beta(\eta_1, \eta_2 + 1)} x^{\eta_1(\bar{s})} (1 - x)^{\eta_2(\bar{s})} \tag{1.30}$$

where

$$\eta_1 = \eta_{01} + \eta_{11} \bar{s} \frac{4}{25}$$

and

$$\eta_2 = \eta_{02} + \eta_{12} \bar{s} \frac{4}{25}$$

with

$$\bar{s} = \ln \frac{\ln(Q^2/\Lambda^2)}{\ln(Q_0^2/\Lambda^2)}$$

Fits to the structure function data determine the parameters η_{01}, η_{11}, $\eta 02$, η_{12} and Λ. Q_0^2 is an arbitrary value of Q^2, and β the Euler Beta function.

The final approach mentioned here involves the numerical solution of the integro-differential Altarelli-Parisi equations [20], which describe the evolution of the quark distributions with Q^2. Again taking the example of xF_3, we have

$$Q^2 \frac{dxF_3(x,Q^2)}{dQ^2} = \frac{\alpha_s(Q^2)}{2\pi} \int_x^1 \frac{dw}{w} xF_3(w,Q^2) P_{qq}\left(\frac{x}{w}\right) \tag{1.31}$$

The "splitting" function $P_{qq}(x/w)$ is explicitly calculable in QCD and is related to the probability of a quark of momentum fraction w emitting a gluon of momentum fraction x/w of the quark momentum. $\alpha_s(Q^2)$ can in principle be calculated perturbatively in QCD. As an example of this method, Abbott and Barnett [21] choose a functional form for xF_3 at some fixed Q_0^2 and "evolve" to other Q^2 using (1.30), determining the parameters Λ and those of the assumed function from a fit to the data over the whole available x, Q^2 plane.

It should be emphasised that the above predictions for the form of the scaling violation are true only in the limit Q^2 large. At finite Q^2, the situation is complicated by the presence of so-called "higher twist" effects [22] due to departures from the simple quark-parton model picture of the scattering process. Examples of higher twist effects include coherent phenomena such as resonance production and elastic scattering, in fact all processes in which gluons are exchanged between struck and spectator quarks. Describing higher twist effects requires knowledge of bound state nucleon wave functions and it is not possible to perform a perturbative calculation in the manner of "leading twist" (twist 2) QCD. Corrections to, for example, the moment prediction of (1.29) are believed to be of order $1/Q^2$ [21] and therefore become potentially important in the lower Q^2 regime. Identifying the relative contribution of logarithmic and power law contributions to the observed deviations from scaling remains one of the tasks of structure function analyses and requires precise measurements over a wide kinematic region.

1.5 THE CHOICE OF SCALING VARIABLE

In the preceding discussion of neutrino-nucleon scattering, contact between the description of the process in terms of structure functions and the quark-parton model has been made in terms of Bjorken's scaling variable, x, which is taken in the Bjorken limit to be an approximation to the fraction of the nucleon momentum carried by the struck quark. In reality the kinematic region available to present experiment is far from the Bjorken limit, and it has been argued that allowance must be made in interpreting the data for the non-zero mass of the nucleon [23]. A better approximation to a "true" (and unknown) scaling variable is believed to be obtained if the analysis is performed in terms of the Nachtmann variable [24]

$$\xi = \frac{2x}{1+\sqrt{1+4m^2x^2/Q^2}} \tag{1.32}$$

which takes into account the finite mass of the target nucleon. In the limit of small x and large Q^2 the scaling variables ξ and x become equivalent.

Attempts to incorporate target mass effects into the analysis of structure functions expressed in terms of x and Q^2 have been made [25] by replacing (1.28) with the corresponding Nachtmann moment. For xF_3 this has the form

$$M_3^n(Q^2) = \int_0^1 \frac{\xi^{n+1}}{x^3} xF_3(x,Q^2) \frac{1+(n+1)\sqrt{1+4m^2x^2/Q^2}}{n+2} dx \tag{1.33}$$

In Chapter 6 both the Cornwall-Norton and Nachtmann moments of F_2 and xF_3 will be calculated.

1.6 STRUCTURE FUNCTIONS IN A COMPLEX NUCLEUS

Recent experimental results have indicated that the nucleon structure functions obtained in muon and electron scattering experiments vary according to the nature of the target nucleus [26] [27]. If such a phenomenon were to occur in the kinematic regime of neutrino scattering experiments, differences may be expected in the structure functions measured on, for example, iron (CDHS), marble (CHARM), neon and deuterium (WA59,

WA25 in BEBC). To reliably search for such differences by comparison of structure functions measured from these different targets requires careful and detailed control over the systematics of the respective experiments, and is not attempted in the present work. The problem has been addressed using the WA59 data set by comparison of cross sections for neon and deuterium in reference [28].

In the context of the present work the following remarks are made. Nucleons bound in nuclei, as opposed to free protons in a hydrogen target, are subject to Fermi motion within the nucleus. Historically in extraction of structure functions corrections for this effect have been made in order to obtain a nucleon structure function measured effectively from a stationary nucleon. Such corrections are necessarily model dependent, and if the possibility of nuclear effects on the structure function are allowed, Fermi motion could in principle be interpreted as one such nuclear effect. In the present analysis the effect of inclusion or omission of a reasonable model for Fermi motion on the structure functions obtained is considered.

For similar reasons the effect of applying radiative corrections when extracting the structure functions will be investigated.

Chapter 2

THE EXPERIMENT

2.1 INTRODUCTION

Many of the experimental details relevant to the WA59 experiment are shared with other neutrino experiments performed in the West Area at CERN, a feature of the minute interaction cross section of neutrinos with matter being that several experiments can concurrently utilise the same beam. The ensuing description is divided up in the following manner. Those details pertaining to the neutrino experiments as a whole, notably the production of the beam and flux monitoring, are described in Section 2.2. The characteristics of BEBC and the External Muon Identifier (EMI) can be found in Section 2.3, while the final section, 2.4, covers those details specific to the WA59 experiment.

2.2 THE NEUTRINO BEAM

The following discussion concerns the production of the neutrino beam starting from the proton beam in the Super Proton Synchrotron (SPS), and the method of deducing the resulting neutrino flux.

2.2.1 PRODUCTION OF THE BEAM

A schematic diagram of the CERN neutrino beam line is shown in Fig. 2.1. In simple terms, a muon neutrino beam is produced by the bombardment of a suitable target with high energy protons. Some of the secondary hadrons from this bombardment have weak decay modes producing muon neutrinos. By appropriately selecting these hadrons in momentum and charge prior to decay, and by the use of shielding downstream of the decay region to absorb all particles except neutrinos, a relatively clean beam of muon neutrinos of suitable characteristics can be obtained.

In the CERN neutrino facility, a spill of protons of energy up to 450 GeV is obtained every 12s from the Super Proton Synchrotron (SPS). Each spill consists of a pulse of duration approximately 2ms and containing the order of 10^{13} protons. These are directed 400m to the neutrino cave to strike one of two beryllium targets T9 or T11, depending on the type of neutrino beam (respectively Wide Band or Narrow Band, see below) required.

The secondary hadrons emerging from the target are predominantly pions and kaons. Of these, it is the decays of the charged pions and kaons which are responsible for the majority of muon neutrinos, as follows

$$\begin{aligned} \pi^+ &\rightarrow \mu^+\nu_\mu, \pi^- \rightarrow \mu^-\overline{\nu}_\mu \quad (BR\ 100\%) \\ K^+ &\rightarrow \mu^+\nu_\mu, K^- \rightarrow \mu^-\overline{\nu}_\mu \quad (BR\ 63.5\%) \end{aligned} \tag{2.1}$$

Two types of neutrino beams have been used at CERN, depending on the method of focussing of the parent pions and kaons prior to decay. For the Narrow Band Beam, a beam of high energy parents of correct sign and well defined momentum is selected using a series of quadrupole magnets. A neutrino energy spectrum enhanced at high energy and with a strong correlation between energy and angle made with the beam axis is obtained at the expense of the total neutrino flux. For the Wide Band Beam, two coaxial magnetic lenses, known as horn and reflector, and situated 92m apart, produce a magnetic field which has the effect of focussing parents of one sign and defocussing those of opposite sign, over a wide range of energies. A maximal flux of neutrinos is obtained, peaked however towards lower energy than in the Narrow Band case and exhibiting none of the

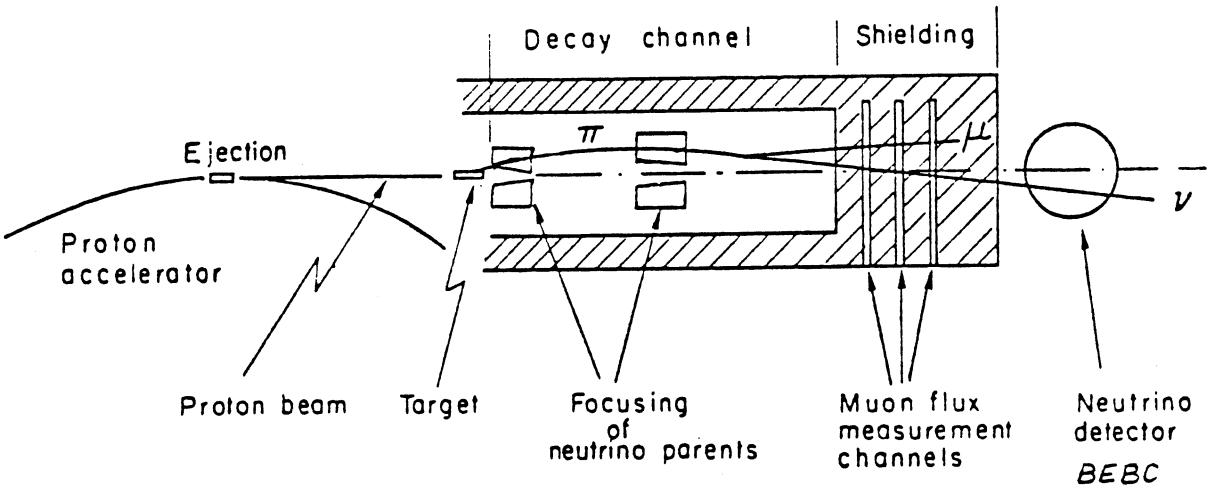

FIG 2.1 SCHEMATIC DIAGRAM OF NEUTRINO BEAM LINE

energy-angle correlation. For the WA59 experiment the Wide Band Beam was used, in order to obtain a high flux of neutrinos.

In both types of beam, the focussed parents leave the neutrino cave and pass into an evacuated decay tunnel of length 290m, during the traversal of which some percentage of parents decay in the modes given above. Downstream of the decay tunnel lies 185m of iron shielding and a further 173m of earth shielding, designed to absorb all undecayed parents and the more highly penetrating muons accompanying the produced neutrinos. At various intervals in the iron shielding are located gaps containing arrays of silicon detectors designed to measure the muon flux, from which the neutrino flux may be inferred in the manner described below.

Beyond the shielding, in the path of the emerging neutrino beam, lie the neutrino detectors. BEBC is situated in total 823m downstream of the target, with the massive counter experiments of the CDHS and CHARM collaborations located in a building some 50m further downstream.

2.2.2 MEASUREMENT OF THE NEUTRINO FLUX

A knowledge of the magnitude of the neutrino flux passing through a detector and its variation with neutrino energy and position in the detector is important for many analyses, including the present one. Whilst it is not possible to measure this flux by counting neutrinos, it is possible to make use of the fact that each muon neutrino produced in the decay of a parent pion or kaon is accompanied by a muon, which can be detected as it is stopped in the shielding following the decay tunnel.

A detailed account of the method of determining the neutrino flux for the wideband beam is given for instance by Giles [29]. In essence, an array of silicon detectors located in each of the first five gaps in the iron shielding is used to determine the absolute flux of muons as a function of position in the gap. For the details of the construction of the detection system, the data acquisition and the calibration of the so-called "Neutrino Flux Monitor" or NFM, the reader is referred to the thesis of Heijne [30]. From the muon flux, it is possible to infer the neutrino flux by use of a Monte Carlo program which models the passage of parents and decay products through the Wide Band beamline, starting with an assumed form for the production spectra of pions and kaons in the beryllium target. These input spectra are adjusted until the muon flux predicted by the Monte Carlo is in agreement with the data. The neutrino flux is then automatically obtained from the two body decay kinematics of the pions and kaons.

The measured values of the neutrino flux for the WA59 experiment are given in section 4.2.

2.3 THE DETECTION SYSTEM

The experimental setup commonly referred to simply as the Big European Bubble Chamber (BEBC) in fact consists of two parts, i) the chamber itself, acting as target, vertex detector and a means of observing, and measuring the momenta of, the individual particles from the interaction, and ii) a counter system known as the External Muon Identifier (EMI), for the identification of muons from the neutrino interaction. These are described respectively in the following two sections.

2.3.1 THE BUBBLE CHAMBER

A plan of BEBC is given in Fig. 2.2. The chamber itself is cylindrical in shape topped with a hemispherical section, into which five cameras, with fish eye optics for greater coverage of the available volume, project. The diameter of the chamber is 3.7m and total height about 4m, producing a volume of approximately $32m^3$. The chamber is cryogenic, and has operated with fillings of liquid hydrogen, liquid deuterium and a liquid neon-hydrogen mixture, at temperatures typically of the order 25K - 30K. Expansion occurs every 12s in line with the extraction of the proton beam, with bubble size approximately 500 microns. The chamber is illuminated by flash and photographs taken with all five cameras (one at high resolution) following each expansion.

Surrounding the chamber are two large superconducting coils, producing a highly uniform vertical magnetic field in the chamber of strength approximately 3.5 tesla. The magnetic field allows determination of the momenta of charged particles from track curvature. Enclosing the magnet is iron shielding, acting to confine the high magnetic field to within the vicinity of the chamber.

2.3.2 THE EMI

Muon identification is provided by two planes of multiwire proportional chambers located downstream of the bubble chamber, as depicted in Fig 2.3 and described in detail in [31]. Nearly all hadrons produced in interactions in the chamber are absorbed by downstream shielding, while muons of energy greater than about 3 GeV penetrate the shielding to register hits in the EMI planes. The "inner plane", located between the chamber walls and the iron shielding enclosing the magnet, consists of 8 overlapping chambers of dimensions 3m x 1m, giving $24m^2$ of sensitive area. These chambers are shielded from hadrons by the magnet material and approximately 0.5m of lead. The "outer plane" is located beyond the iron shielding, and protected in the vicinity of the beam axis by an additional 1.3m of iron. This plane consists of 46 chambers of design similar to the inner plane chambers, located in two semicircles mounted one above the other with a total length of 25m. The outer plane thus has a sensitive area of approximately $150m^2$.

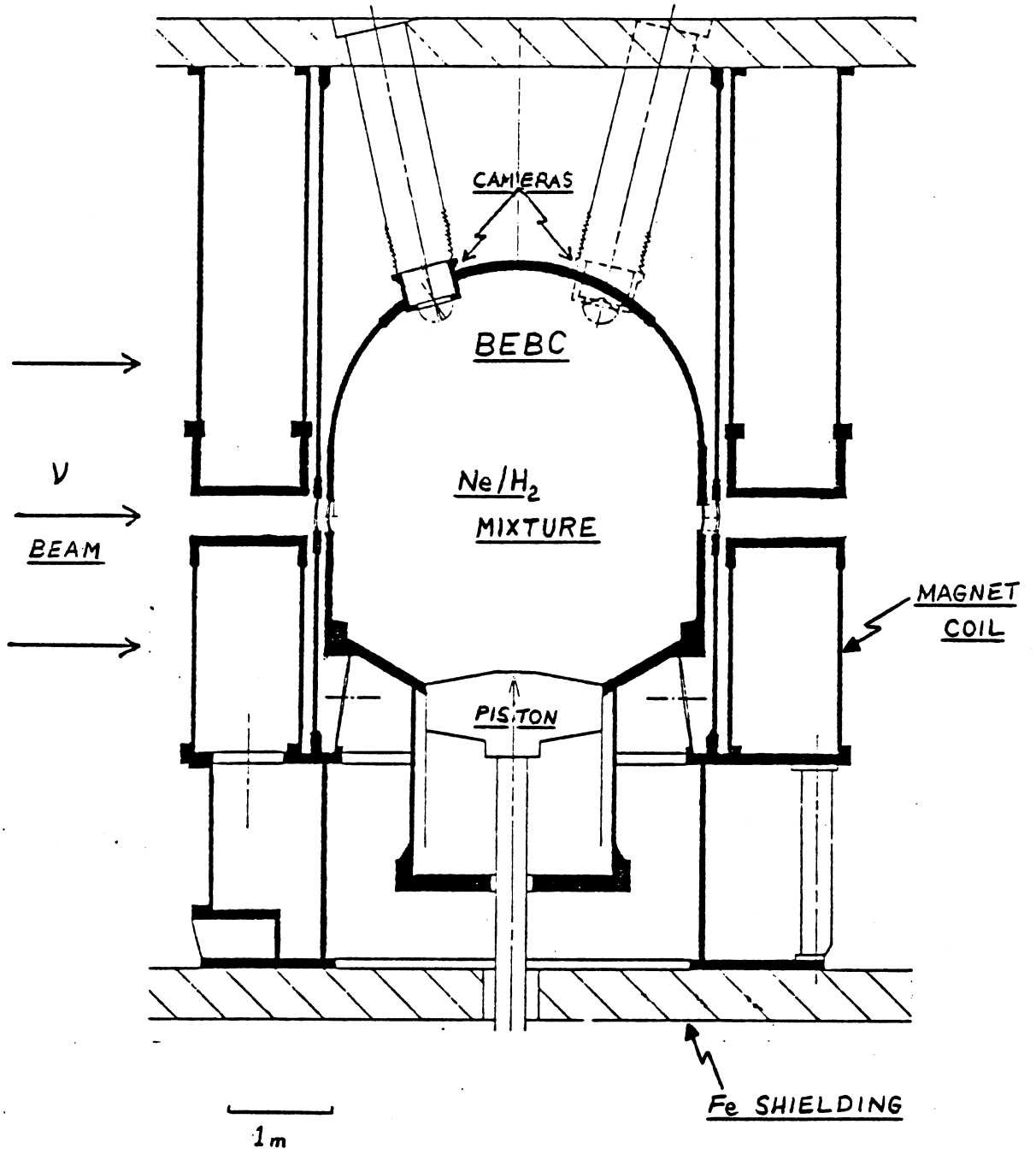

FIG 2.2 PLAN OF THE BIG EUROPEAN BUBBLE CHAMBER (BEBC)

During each beam spill, the hits recorded by the wires of each chamber in a sequence of 250ns "time slots" are recorded in shift registers and subsequently written onto magnetic tape. These "EMI tapes" are used for later off-line identification of muon tracks as

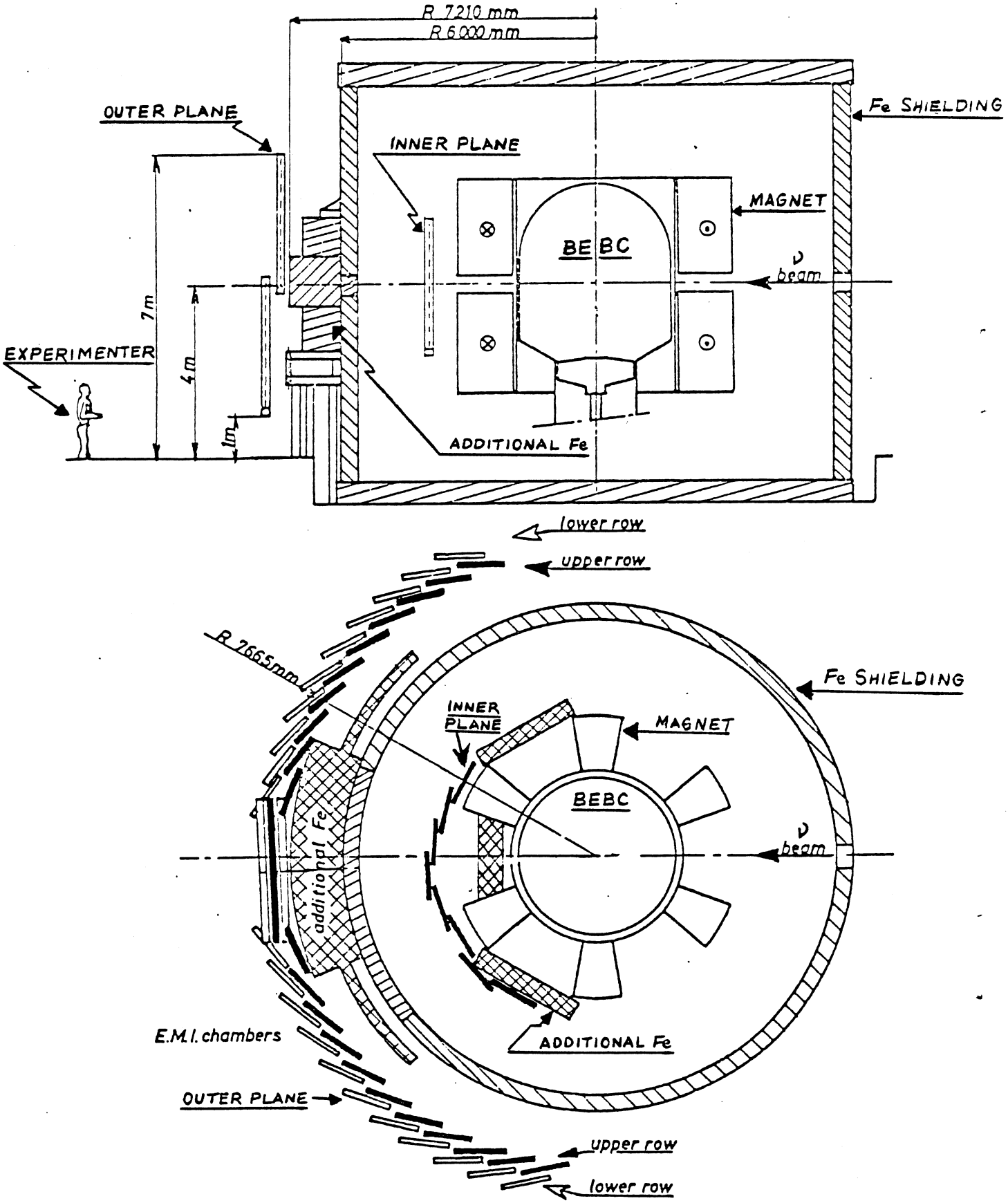

FIG 2.3 LAYOUT OF THE EXTERNAL MUON IDENTIFIER (EMI)

described in Section 2.4.7.

The geometric and electronic efficiencies of the EMI for muon identification are very high for muons of momentum greater than 5 GeV, the minimum momentum considered in this analysis. A discussion of the effect of inefficiency in muon identification on this analysis can be found in Chapter 3.

2.4 THE WA59 EXPERIMENT

The remainder of this chapter is concerned with those experimental considerations specific to the WA59 experiment. Details of the chamber filling and beam conditions relevant to the experimental run are followed by a description of the off-line processing of the bubble chamber film.

2.4.1 THE CHAMBER FILLING

For the WA59 experiment, BEBC was filled with a heavy neon-hydrogen mixture in molar proportions 75% to 25% respectively. This provided a nearly isoscalar target of density .707 g cm^{-3} and radiation length 42cm. The relatively high density of this mixture in comparison to a deuterium or hydrogen filling allowed a higher event rate, whilst the shortness of the radiation length compared to the chamber dimensions allowed an increased probability for the photons from the interaction to convert within the chamber liquid, thereby giving better neutral energy determination. Disadvantages of using a high Z nucleus as the filling included poorer resolution in track measurement, due to multiple Coulomb scattering, the presence of Fermi motion of nucleons within the nucleus, and the problem of large electromagnetic showers, particularly in high energy events, obscuring tracks from the primary vertex.

2.4.2 STATISTICS OF THE EXPERIMENTAL RUN

The CERN Wideband neutrino and antineutrino beams, as described in Section 2.2.1, were used in the WA59 experiment in order to obtain a high neutrino flux and corresponding high event rate. During the 15 day running period in April 1980, 5 days of which were devoted to the neutrino beam and 10 days to antineutrino, a total of approximately $1\times10^{17}(\nu)$ and $7\times10^{17}(\bar{\nu})$ protons on target were obtained. The numbers of bubble chamber photographs exposed were $36315(\nu)$ and $61041(\bar{\nu})$ respectively. These were divided amongst the 12 collaborating laboratories * for off-line processing.

2.4.3 SCANNING

All bubble chamber photographs were twice scanned by trained scanners, using a set of scan rules designed to identify candidate charged current (CC) events. Important criteria for identification were that events should have no incoming charged tracks, and at least one fast leaving minimally ionising track (a muon candidate). All charged tracks, and possible associated neutral particles (gamma conversions, and decays or interactions of hadrons, known respectively as V^0s or n^*s) were recorded by the scanners for later measurement.

In addition to these two main scans of all the film, a further two scans were performed at a later date in order to obtain a more complete sample of low multiplicity events (i.e. events with few charged tracks), which are inherently more difficult to find. In the original double scan of the antineutrino film, events with a single muon and no associated neutrals (candidate elastic events) were not included in the scan rules, making this further "special" scan essential in order to obtain a sample of these events and to estimate a scanning efficiency. Only events with one or two charged tracks (so called 1 or 2 prongs) were included in the scan rules. For these scans, the scanners were instructed to follow back

* 1. Istituto di Fisica dell'Universita e Sezione, Bari. 2. University of Birmingham. 3. Inter-University for High Energies ULB-VUB, Brussels. 4. CERN. 5. Nuclear Research Centre Demokritos. 6. LPNHE, Ecole Polytechnique. 7. Imperial College London. 8. Max-Planck-Institut fur Physik and Astrophysik, Munich. 9. University of Oxford. 10. Rutherford Appleton Laboratory. 11. CEN Saclay. 12. University College London.

to their origin all leaving tracks on a given frame, as it was believed that this was a more efficient method of finding low multiplicity events than the "area" scan method used for the main scans.

As a result of the analysis of the above scans, it was found necessary to perform a third partial scan of the film in order to obtain further information on the scanning efficiencies. This third scan, referred to as the "sector" scan, consisted of a double scan of 10% of the total film sample, involving a systematic and detailed area scan of the photographs logically divided into 11 sectors. These sectors were defined in terms of the boundaries of the panels of BEBC as seen on the photographs. The aim of the scan was to locate a sample of events in the reduced film sample with very high efficiency, against which events obtained in the same film sample in the previous scans could be compared. For these scans film was interchanged amongst the various laboratories.

The "sector scan" described in the preceding paragraph produced an event sample contained in a different volume to that of the main scan. The intersection of this volume with that of the main scan will henceforth be referred to as the "sector scan volume" and will be the one used for the majority of the analysis, as it is only in this volume that the scanning efficiencies were well determined. The ratio of the sector scan volume to the main scan volume was 0.69.

The question of scanning efficiencies will be considered in more detail in Chapter 3.

2.4.4 MEASURING

Following the initial two scans of a section of film, those events satisfying the criteria for a candidate CC event, along with any associated gammas, V^0s or n^*s, were measured on three views. The measuring process involves accurately recording, for each track on each view, the position in two dimensions of a sufficient number of points along the track to enable the GEOMETRY program, described below, to reconstruct the trajectory in three dimensions and thus determine the momentum and charge of the track. In the case of short interacting tracks, for which an accurate measurement might be impossible,

the tracks from the secondary interaction vertex were measured in order to deduce the momentum of the interacting track.

Only those events whose primary vertex proved to be within a fiducial volume of 16.3m^3, depicted in Fig. 2.4, were retained. The fiducial volume requirement ensured that for all events retained the tracks leaving the primary vertex were of sufficient length to enable a good measurement to be made.

2.4.5 THE "GEOMETRY" PROGRAM

Once measurement of the events is completed, the GEOMETRY program is run to determine the momenta of the charged tracks. Given the set of measurements for the charged tracks of an event on three views, a map of the magnetic field strength and direction in the chamber, and the range-momentum information for various charged particle types traversing the chamber liquid, GEOMETRY will attempt to obtain the best fit for the trajectory of each particle under various mass hypotheses. No decision as to the particles' identification (apart from excluding those hypotheses for which no fit is possible) is made at this stage of the chain, all possible "mass fits" being retained on the output GEOMETRY SUMMARY TAPE, or GST, for use by later programs.

2.4.6 CHECK SCANNING AND REMEASUREMENT

At completion of the initial set of measurements and the running of GEOMETRY, each event on the GEOMETRY output was carefully checked by an experienced scanner in conjunction with rescanning the event on the scan table. If the event measurement was unsatisfactory, for instance with charged tracks missing, badly measured or duplicated, or with associated neutrals not measured, the check scanner would call for any necessary remeasurements to be performed. This process of checking, remeasurement and rerunning of GEOMETRY was continued iteratively until all events on the GST were satisfactory.

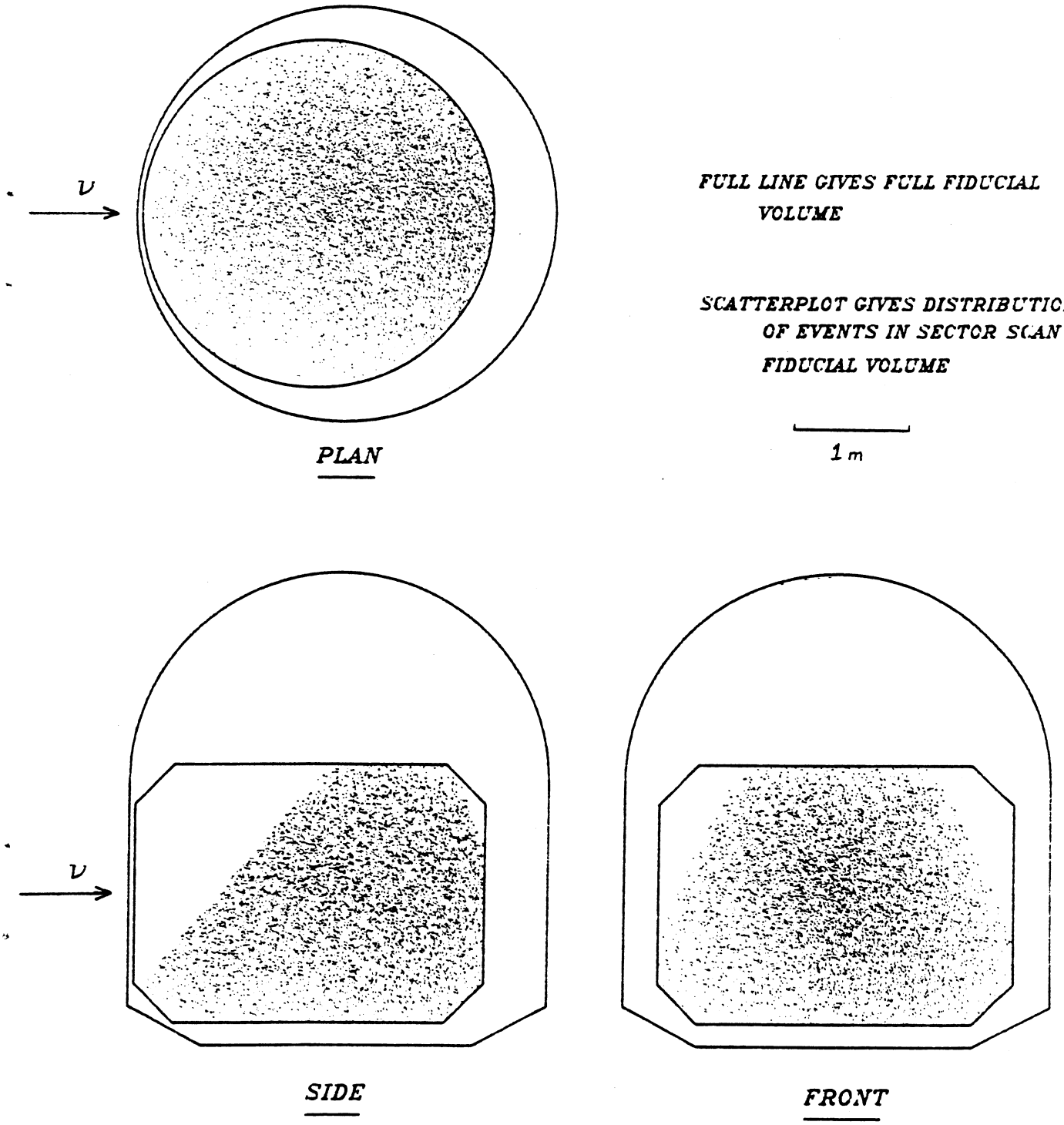

FIG 2.4 WA59 FIDUCIAL VOLUMES

2.4.7 THE "EMI" AND "EMIANA" PROGRAMS

The purpose of the EMI and EMIANA programs is to associate, where possible, those tracks of an event leaving the chamber with hits in the External Muon Identifier. The EMI program extrapolates all leaving tracks of an event through the shielding and other material downstream of the bubble chamber to the two planes of the EMI, thereby predicting hits in certain chambers on the assumption that the track was a muon. Using the information for that frame written onto magnetic tape during the experimental run, the EMI program associates hits recorded in those chambers with the extrapolated track. The EMIANA program is then run in order to make a decision, on the basis of the χ^2 probability of association of these hits with the track in question, whether to accept the muon hypothesis.

Only those tracks with acceptable hits in both inner and outer planes of the EMI were flagged as muons. All other leaving tracks were taken, in the absence of other means of identification, to be pions.

2.4.8 "QUACK" AND "SYNTHESIS"

All of the above steps in the production chain were carried out individually in each of the twelve laboratories. Following the passage of the data through the EMIANA program, all data were collected into a single data set at the CERN laboratory, for the production of a combined DATA SUMMARY TAPE or DST. Producing this final DST involved the running of two further programs. The first, known as QUACK, is a general data quality checking program. The SYNTHESIS program performs, amongst other functions, those of selecting the best mass hypothesis for each track from the GEOMETRY results, deciding on the most likely identity of neutral particles (for instance resolving ambiguities between gamma and V^0 hypotheses), linking associated gammas, $V^0 s$ and $n^* s$ to the primary interaction vertex, and constructing the 3-momentum of short interacting tracks from the measurement of secondaries.

The SYNTHESIS output, or DST, consists of a set of magnetic tapes written in the "HYDRA" format (a data management system developed at CERN), containing for

each event all GEOMETRY, EMI and EMIANA output information, along with some additional event summary information (the so called PHYS structure) produced by SYNTHESIS in a format readily suited for analysis.

Chapter 3

THE EVENT SAMPLE

3.1 INTRODUCTION

In order to seriously study the structure functions introduced in Chapter 1, it is first necessary to isolate, from the raw event sample resulting from the production chain of section 2.4, a selection of charged current (CC) events free from experimental biases. It was seen in section 1.2 that the kinematics of an inclusive charged current event may be completely specified in terms of three independent variables, for example the neutrino energy E, Bjorken's scaling variable x, and the negative square of the current 4-momentum, Q^2. The purpose of this chapter will be the determination of the distribution of charged current events in terms of these variables. The discussion is organised in the following manner. In section 3.2, the necessary selections on events contained on the Data Summary Tapes (DST's) in order to obtain a sample of CC events will be discussed. Sections 3.3 and 3.4 will deal with some corrections to the numbers of events in this sample due to EMI inefficiencies, contamination of "neutral current" events, and scanning losses. Selection of an elastic sample, which requires special treatment when estimating neutrino energy, is considered in section 3.5. The problem of estimation of the values of E, x and Q^2 for an event from the observed particles will be the subject of section 3.6. It will be found that due to certain experimental limitations the estimated distribution in E, x and Q^2 will not

be the correct one. The important question of unsmearing, or the estimation of the "true" distribution from the "measured" one, will be the subject of section 3.7.

In the remainder of this chapter, the neutrino and antineutrino event samples will generally be referred to by the generic term "neutrino". This should be understood to refer to both samples unless specifically stated otherwise.

3.2 SELECTING A SAMPLE OF CC EVENTS

To ensure that the sample of events chosen for analysis constitutes a reliable sample of CC events, as free as possible from uncalculable experimental biases, a number of selection criteria, or "cuts", were applied to the data. These are described below.

3.2.1 RIGHT SIGN MUON

Each event was required to possess an EMI identified muon of the correct sign, that is, negative for the neutrino beam and positive for the antineutrino beam. For a small percentage of the events more than one muon candidate was present. While this topology is possible, for instance from the semileptonic decay of a heavy quark, the majority of such events result from random association in the EMI. Such events were treated by selecting as the true muon the candidate of largest transverse momentum to the beam direction, checking this track for the correct sign, and assigning the other "muons" the pion mass. The effect of incorrect choice of muon on this analysis is negligible.

3.2.2 MUON MOMENTUM CUT

The EMI provides practically 100% geometric acceptance for high momentum muons originating within the chamber fiducial volume. As the muon momentum is reduced below 5 GeV/c, however, the acceptance begins to decrease significantly, as low momentum muons are absorbed in the shielding or curve sufficiently in the magnetic field to miss the EMI planes. A cut of 5 GeV/c on muon momentum was therefore employed to ensure good

muon identification. The small effect of geometric inefficiency for muons of momentum greater than 5 GeV/c is considered in section 3.3.

3.2.3 GOOD FLUX

Extraction of structure functions requires a knowledge of both the energy/radial distribution and normalization of the neutrinos passing through the chamber. It is important therefore to include in the analysis only those measured events for which the neutrino flux was known and stable. The DST's were flagged with information on the flux conditions pertaining to a given frame, and only events from frames corresponding to "good" flux conditions were used. Typical reasons for rejection of frames were the total absence of flux information, due to inoperation of the Neutrino Flux Monitoring (NFM) system, non-standard values for the current in the horn and reflector providing focussing of the parents, and asymmetries in the beam caused by misalignment of the protons from the SPS.

3.2.4 NEUTRINO ENERGY CUT

At low neutrino energy, especially below 10 GeV, the estimation of the neutrino flux from the measured muon fluxes in the iron shielding (see section 2.2.2) becomes somewhat unreliable. In order to reduce systematic error resulting from the lack of knowledge of the flux in this region, a neutrino energy cut of 10 GeV was employed. As will be shown in section 3.6, the actual estimation of the neutrino energy of an event is itself subject to uncertainty, as is therefore the boundary of the cut. This must be correctly allowed for in the unsmearing calculation, described in section 3.7.

3.2.5 COMPLETE MEASUREMENTS

In high energy neutrino interactions, especially in a heavy liquid, a very small percentage of events prove to be unmeasurable, due for instance to an electromagnetic shower associated with the event obscuring tracks, or to overlapping tracks causing "confusion" in

the region of the primary vertex. These events are flagged as "incomplete" on the DST's and were not included in the chosen event sample. Such events are so few in number as to introduce no bias through their omission.

3.2.6 FIDUCIAL VOLUME

The primary vertex of all events was required to lie within the sector scan fiducial volume described in section 2.4.4, within which scan efficiencies were well determined. The ratio of observed events (within the cuts described here) within the sector scan volume to observed events within the main scan volume was .743 for neutrino events and .741 for antineutrino events.

3.2.7 "STUBS"

The interaction of a high energy neutrino with a nucleon in a complex nucleus such as neon can result in the breakup of that nucleus. This can be observed in the bubble chamber by the appearance of short proton tracks, or "stubs", associated with the interaction vertex. A cut to exclude these stubs, which do not result from the interaction of interest, was employed. All backward going stubs (with respect to the neutrino direction) were excluded, along with those forward going stubs of momentum less than 300 MeV/c.

3.2.8 LABORATORY DEPENDENT CUTS

The question of scanning inefficiencies will be discussed in section 3.4. It was found from the scanning information that for the antineutrino sample, a systematic but unaccountable bias existed in the data samples from the Demokritos, Ecole Polytechnique and Imperial College London laboratories (data from these laboratories contributed approximately 16% of the total antineutrino data set). In order not to introduce a scanning bias which could not readily be corrected for, data from these laboratories was not included in the antineutrino sample for this analysis. No such problem was evident in the neutrino sample, for which all data was accepted.

3.3 CORRECTIONS DUE TO MUON IDENTIFICATION

Three systematics relating to muon identification will be discussed in this section, the geometric acceptance of the EMI, the electronic inefficiency of the EMI, and the contamination of neutral current events.

3.3.1 GEOMETRIC ACCEPTANCE OF THE EMI

The correction to the data sample necessary to account for the geometric inefficiency of the EMI was estimated in the following manner. In principle, the probability that a muon from a CC event will penetrate both planes of the EMI can depend on the position of the event in the chamber and the muon momentum vector. It is desired to know the acceptance in terms of three independent variables specifying the event. The variables chosen were the neutrino energy E, the muon momentum p_μ and the sine of the angle between the muon and neutrino directions, $\sin\theta_\mu = p_\mu^T/p_\mu$. Events were generated within the experimental fiducial volume by Monte Carlo simulation in a given neutrino energy range, with a spatial distribution given by the predicted neutrino flux. The muon momentum vector was then generated flat in p_μ and p_μ^T, and symmetric in angle ϕ about the neutrino direction. The muon was then tracked through the chamber and surrounds to the EMI. The efficiency, averaged over x, y, z and ϕ, was defined as the fraction of muons of given E, p_μ and $\sin\theta_\mu$ passing through both planes. It was found that the efficiency was to good approximation independent of neutrino energy. The efficiency calculation was performed for both neutrino and antineutrino beams, with the results being found to be consistent within statistical errors. The geometric efficiency in bins of p_μ and $\sin\theta_\mu$, averaged over neutrino and antineutrino beams in the energy range 10 to 300 GeV, is given in Table 3.1. The high p_μ and $\sin\theta_\mu$ region is disallowed kinematically. Events in the selected data sample were corrected for acceptance by weighting with a factor given by the inverse of the efficiency interpolated to the measured p_μ and $\sin\theta_\mu$ from Table 3.1. The average correction factor obtained by this procedure was 1.018 for neutrino events and 1.007 for antineutrino events.

Table 3.1 : Geometric Acceptance of the EMI

	p_T^μ/p^μ					
	0.–.1	.1–.2	.2–.3	.3–.4	.4–.5	.5–.6
3–4	.978	.946	.838	.665	.468	.320
4–5	1.000	.984	.892	.669	.498	.363
5–6	1.000	.980	.904	.739	.545	.416
6–8	1.000	.981	.910	.731	.548	–
8–10	1.000	.982	.898	.762	.615	–
p^μ (GeV/c) 10–15	1.000	.984	.909	.788	–	–
15–20	1.000	.988	.923	.790	–	–
20–25	1.000	.989	.925	–	–	–
25–30	1.000	.988	.955	–	–	–
30–40	1.000	.991	.978	–	–	–
40–50	1.000	.995	–	–	–	–
> 50	1.000	.993	–	–	–	–

3.3.2 ELECTRONIC INEFFICIENCY OF THE EMI

A significant cause of loss of muon candidates through electronic inefficiency is the malfunctioning of specific anode wires in the multiwire proportional chambers comprising the two planes of the EMI. Information on the status of all wires is contained on the EMI tapes written during the experimental run, obtained by counting cosmic ray background between spills from the SPS. Using this information a study of muon loss was performed for the present experiment [32] and correction samples of kinematically reconstructed muons obtained which were combined with the total neutrino and antineutrino DSTs. The number of CC events recovered by this method was 125 for the neutrino sample and 248 for the antineutrino sample after weighting.

A further global correction of 3% was applied to both neutrino and antineutrino samples to account for electronic inefficiency not attributable to "dead wires" as described above.

3.3.3 CONTAMINATION DUE TO NEUTRAL CURRENT EVENTS

In addition to the charged current events of the form given by (1.1), neutral current (NC) events of type

$$\nu N \rightarrow \nu X$$
$$\bar{\nu} N \rightarrow \bar{\nu} X \tag{3.1}$$

containing no muons, also occur in the chamber in addition to neutral hadron induced events and isolated V^0s and gamma conversions. It is possible for these events to satisfy the scan criteria for a CC event, and contaminate the CC sample due to misidentification of a hadron as a muon. This can occur due to hadron punch through to the EMI planes, decays of charged hadrons to produce a muon giving a hit in the EMI, or due to random association of a leaving hadron track in the EMI.

The contamination can be estimated by passing the event sample on the GST through the EMI and EMIANA programs using for every frame EMI information from a frame displaced with respect to the frame under consideration. Such an analysis was performed for the neutrino and antineutrino samples by the Birmingham group, producing a sample of fake CC events which were combined with the CC sample with an appropriate negative weight. With a muon momentum cut of 5 GeV/c the NC background sample is negligible in comparison to the total event sample, comprising 17 neutrino and 23 antineutrino events after weighting.

3.4 CORRECTIONS DUE TO SCANNING INEFFICIENCIES

The necessity in bubble chamber experiments to locate events visually produces the problem that not all classes of events satisfying a given set of scan criteria are equally easy to locate. Events with, for example, low charged multiplicity or little electromagnetic shower development are on average located with lower efficiency. If no correction for topology dependent scanning losses is made, a biased sample of CC events is obtained.

For the present experiment, a total of three independent double scans of all or part of the film were performed in order to understand the scanning losses. These "main",

"special" and "sector" scans have been discussed briefly in section 2.4.3. The problem of estimating the scanning efficiency corrections to be applied to the present data is now discussed.

On the basis of two independent scans it is possible to define an estimate of the combined scanning efficiency ϵ by the relation

$$\epsilon = \frac{N_{12}(N_{12}+N_1+N_2)}{(N_{12}+N_1)(N_{12}+N_2)} \tag{3.2}$$

where N_1 is the number of events found on scan 1 only, N_2 the number found on scan 2 only and N_{12} the number found on both scan 1 and scan 2. An assumption underlying this definition is that all events are equally likely to be found, a situation not expected to be true in the present experiment even on a topology by topology basis. As a result of the one and two prong "special" scan it was possible to investigate the validity of (3.2) using the two prong sample common to both the "main" and "special" scans. For the following discussion of scan efficiencies, the full experimental fiducial volume was used.

Using the "main" scan sample and equation (3.2), the two prong scan efficiency was calculated to be .95, based on an observed 1743 two prongs. The total number of distinct two prongs found as a result of combining the "main" and "special" scans was 2166. The upper limit on the two scan efficiency was therefore 1743/2166 = .80. The conclusion to draw is that the use of equation (3.2) can seriously overestimate scanning efficiencies calculated for bubble chamber experiments.

An alternative method of estimating scanning ineffiencies, due to Derenzo and Hildebrand [33] was applied to the above two prong sample. This method assumes that each event has some probability v of being observed on a given scan, as opposed to the above method which assumes that every event has the same probability ϵ of being observed. A parametrization of the distribution of events $F(v)$ in v is chosen and fitted to the data (for details the reader is referred to the original paper in reference [33]). The form for $F(v)$ used was

$$F(v) = \frac{K}{B(\alpha+1,\beta+1)} v^{\alpha}(1-v)^{\beta} \tag{3.3}$$

where $B(x,y)$ is the Euler beta function. To reasonably apply the method, information from more scans than there are parameters in $F(v)$ is required, limiting the method to the two prong sample in the present data for which four scans were performed.

In performing the fit it was necessary to exclude the Oxford laboratory data, for which no scan information was available for the "main" scan, and three further sections of 750 frames which were not scanned in both the "main" and "special" scans. The details of the fit obtained are summarised in Table 3.2. The quantities $\overline{M}_i$ are in effect the number of events found on scan i but not on the (i-1) previous scans, averaged over all possible orderings of the four scans. The χ^2 obtained for the fit appears unacceptably large for what is essentially a one constraint fit. A possible explanation for this lies in the observation that due to the different nature of the "main" and "special" scans, different and to some extent disjoint samples of two prongs were located in each case. The implicit assumption of the Derenzo Hildebrand method that all four scans were performed in a similar manner is therefore not strictly valid in this application. It is also possible that the form chosen for $F(v)$ may be inadequate to describe the true distribution in visibility.

Applying the two scan efficiency deduced from the fit to the data excluded from the fit, it was estimated that the total number of two prongs on the Oxford film was 207 and on the three further sections 88. These events were added to the 2073 two prongs obtained from the fit itself to arrive at a total of 2368 two prongs for the whole film. This corresponds to a two scan efficiency of .74, consistent with the upper limit of .80 obtained above, and a four scan efficiency of .91.

Analysis of the "sector" scan information yielded the estimates of the scanning efficiencies as a function of event topology given in Table 3.3. These estimates were obtained by treating the "main" and "special" scan events as scan 1 and the "sector" scan events as scan 2, applying equation (3.2). In this case, owing to the very high sector scan efficiencies (evidenced by few events found in scan 1 being missed by scan 2), the scanning efficiency is believed not to be seriously overestimated by using equation (3.2). Comparison of the estimate of the scanning efficiency for two prong events obtained from the Derenzo Hildebrand fit (.91) with that obtained from the sector scan information (.95) suggests that the

Table 3.2 : Fit to 2 Prong Scanning Efficiency

	Observed Number of 2 Prongs	Fitted Number of 2 Prongs
$\overline{M}_1$	1234.5	1232.4
$\overline{M}_2$	378.5	382.2
$\overline{M}_3$	174.5	168.7
$\overline{M}_4$	82.5	89.6
K	2073	
α	.93	
β	.32	
χ^2	5.16	
Total Number of Observed 2 Prongs	1870	
Total Number of 2 Prongs from Fit	2073	

Table 3.3 : Scanning Efficiency as a Function of Topology

Number of Prongs	Scanning Efficiency	
	ν	$\overline{\nu}$
1 (elastic)	.222	.810
1 (inelastic)	.800	.939
2	.868	.952
3	.931	.970
4	.960	.977
> 4	.983	.986
All	.952	.963

Derenzo Hildebrand method as applied to the present data produces an underestimate of the scanning efficiency.

The neutrino and antineutrino data samples were corrected for scanning inefficiency on an event by event basis using topology dependent weights corresponding to the efficiencies given in Table 3.3.

3.5 ELASTIC EVENTS

Elastic events are defined by the channels

$$\begin{aligned} \nu n &\rightarrow \mu^- p \\ \bar{\nu} p &\rightarrow \mu^+ n \end{aligned} \tag{3.4}$$

In the absence of effects due to the presence of other nucleons in the neon nucleus, neutrino elastic events appear as two prong events in the bubble chamber and antineutrino elastic events as a single positively charged muon track. Reinteraction effects within the nucleus can cause elastic events to assume different topologies and mimic inelastic events, while the failure to detect neutral particles from an inelastic event can cause these events to appear as elastic candidates. Separation of a pure elastic sample can therefore not be made, and attempts to estimate the numbers and properties of elastic events from the data rely to some extent on modelling the reinteraction processes within the nucleus.

The neutrino energy of an elastic event can be calculated entirely from the muon 4-vector (ignoring small Fermi motion effects), while for inelastic events an estimate must be made given the observed hadron final state. This problem is considered in the following section.

For the present analysis, the following prescription for defining elastic samples was used. In the neutrino case, the candidate elastic sample was taken to be all two prong events with a final state consisting of a μ^- and a single positive hadron (210 events out of a total of 5961 events for all multiplicities). If the hadron was not identified as a

proton, its momentum was used to predict the stopping distance of the track on the assumption that the particle was a proton. Those events in which the hadron travelled further than this distance were excluded from the candidate elastic sample. The hadron in the remaining events was assumed to be a proton, and the value of ν calculated for the event was compared with that required by the "pion threshold" condition (see section 3.6.1). Events with a ν value consistent with an inelastic event were removed from the candidate elastic sample. The remaining events (98 in number), in addition to the few events (23) with a bare μ^-, were considered to be elastic.

Antineutrino elastic events were taken to be all events with a single μ^+, a sample of 498 events out of a total sample of 9561 events.

For reasons discussed above, the definitions just described cannot guarantee pure elastic samples. However, based on simple assumptions, they were believed to give samples containing predominantly elastic events, in numbers comparable to those which might be expected based on measured elastic cross sections for equation (3.4). Identical definitions to those given here were used in treating Monte Carlo generated events, the subject of section 3.7.

3.6 ENERGY CORRECTION

The motivation for the present chapter was the estimation of event distributions in the kinematic variables E, x and Q^2. In a wide band neutrino beam, the energy of the interacting neutrino is unknown, and must be inferred from the 4-momenta of the muon and final state hadrons. Even in a bubble chamber filled with a heavy liquid, however, not all final state hadrons are detected, as neutral hadrons and gammas may fail to interact, decay or convert within the chamber. The problem therefore remains to estimate the neutrino energy E, and x and Q^2, from the observed final state.

3.6.1 ENERGY CORRECTION FOR INELASTIC EVENTS

Figure 3.1 defines the 4-momenta for a neutrino interacting with a stationary nucleon, the x axis being taken as the neutrino direction and the x-y plane being defined by the neutrino and muon 3-momenta. The label "s" refers to the "seen" or observed hadronic system and "m" to the "missing" or undetected hadronic system. Energy-momentum conservation results in the following equations.

$$E + m_N = E^\mu + E^s + E^m \tag{3.5}$$

$$E = p_x^\mu + p_x^s + p_x^m \tag{3.6}$$

$$0 = p_y^\mu + p_y^s + p_y^m \tag{3.7}$$

$$0 = p_z^s + p_z^m \tag{3.8}$$

which represent a system of four equations in the five unknowns E, E^m, p_x^m, p_y^m and p_z^m. A constraint is required in order to solve the equations.

Several methods of energy correction have been employed in neutrino bubble chamber experiments, based to varying degrees on physical principles. As an illustrative example of an event by event method consider the Myatt method [34], which employs momentum balance transverse to the beam direction. On the premise that the seen and missing hadronic systems possess similar properties, it is assumed that these systems have the same direction in space, which implies

$$\frac{p_x^s}{p_y^s} = \frac{p_x^m}{p_y^m} \tag{3.9}$$

Combining (3.6), (3.7) and (3.9) leads to

$$E = p_x^\mu - \frac{p_y^\mu}{p_y^s} p_x^s \tag{3.10}$$

giving an estimate of the neutrino energy in terms of measured quantities.

The physical principle on which the Myatt method is based, the common direction of the seen and missing hadron vectors, clearly breaks down if the seen hadron system lies on the same side as the muon with respect to the neutrino direction, or is backward with

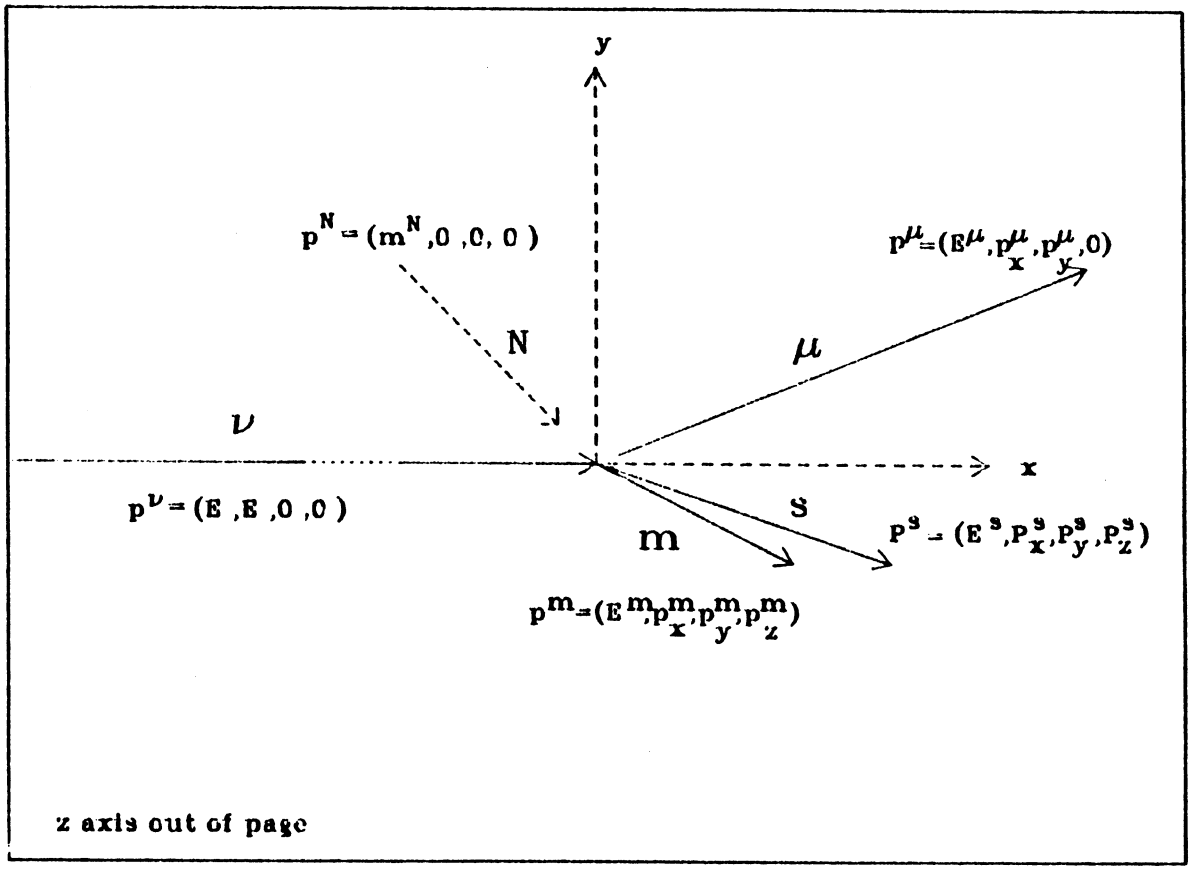

FIG 3.1 DEFINITION OF 4-MOMENTA

respect to this direction. In either case use of the Myatt method must lead to unphysical estimates of for the kinematic variables characterising the event, and an alternative method must be employed. For the present analysis, these events were corrected using the constant correction method to be described below.

A comment on the Myatt method, and energy correction in general should now be made. When the target nucleon is contained in a complex nucleus such as neon, Fermi motion of the struck nucleon within the nucleus makes equations (3.5) to (3.8) no longer strictly valid, as the 4-momentum of the nucleon (assumed to be $(m_N, 0, 0, 0)$ in the above equations) is unknown. Therefore even if all final state particles are observed and well measured, transverse momentum balance may not be observed. It is also true that the assumption embodied in (3.9) will not be true on an event by event basis, though it may well be true on average. The point to note is that whichever energy correction is used to estimate the neutrino energy, the problem remains to estimate the bias introduced into the resulting distributions due to the method chosen. This is in general done by use of a Monte Carlo program, as described in the following section. The necessary corrections required to account for these biases are known as "unsmearing factors". As any choice of correction method requires unsmearing, the particular choice of correction method to employ is not crucial provided the unsmearing calculation is carefully performed.

For the present analysis, the Myatt method was applied to estimate the neutrino energy as described above. In order to study the systematic effects involved in this choice, the analysis was repeated using two further methods of energy correction, which are now described.

The first of these methods amounted in effect to "no energy correction", with the visible hadron energy used to estimate the neutrino energy. With $E^m = 0$, equation (3.5) can be rewritten in the form

$$E = E^\mu + \nu \tag{3.11a}$$

$$\nu = E^s - m_N \tag{3.11b}$$

where E^s is the sum of the energies of the final state hadrons. In an ideal neutrino-nucleon interaction, excluding baryon pair production, the final state hadrons will contain only one baryon. However, in a neon nucleus containing other nucleons besides the one initially struck, more than one baryon may appear in the final state. The condition that only one baryon mass entered into E^s was ensured by including only the kinetic energy $T = E - m$ of each baryon in the final state in the sum to obtain E^s, adding in a single nucleon mass after summing over all particles.

The second method employed will be referred to as the "constant" correction method. In this case the visible hadron energy E^s was estimated as in the above "no correction" method, and ν calculated using equation (3.11b). ν was then scaled by a constant correction factor C, given by the relation [35]

$$C = -\frac{< p_y^\mu >}{< p_y^s >} \tag{3.12}$$

where $< p_y^\mu >$ ($< p_y^s >$) denotes the mean value of p_y^μ (p_y^s) taken over all events. For the data under consideration C has the value 1.19 for the neutrino sample and 1.24 for the antineutrino sample. C may be thought of as an "average" Myatt correction factor, if the similarity with the correction factor in equation (3.10) is noted. It is here being used to correct ν in the energy equation (3.5) rather than p_x^s in the longitudinal momentum equation (3.6), in which case the connection with the Myatt method would be obvious. The choice of equation (3.5) rather than (3.6) was made in the belief that a better treatment was given to the low W^2, low multiplicity events. For the majority of events use of a constant correction factor with either equation (3.5) or equation (3.6) give very similar results.

An additional constraint of use in estimating the neutrino energy which was employed in conjunction with all three methods used, is the so called "pion threshold" condition. This is the requirement that the final state hadronic system in an inelastic event must consist of at least one nucleon and one pion, in which case

$$W^2 \geq (m_N + m_\pi)^2 \tag{3.13}$$

where m_N is the nucleon mass and m_π the pion mass. This can be equivalently expressed in terms of the energy transfer ν,

$$\nu \geq \nu_{min} = \frac{2E^\mu(E^\mu - p_x^\mu) + 2m_N m_\pi + {m_\pi}^2 - {m_\mu}^2}{2(m_N - (E^\mu - p_x^\mu))} \tag{3.14}$$

Having estimated the neutrino energy by any of the above methods, ν was then calculated from equation (3.11a) and compared with ν_{min}. When the inequality in equation (3.14) was not satisfied, ν was set to ν_{min} and E adjusted appropriately.

Application of the pion threshold condition ensured that all events lay within the physically allowed kinematic region. Having obtained an estimate of E, the other kinematic quantities x and Q^2 were then completely specified in terms of E and the muon variables.

3.6.2 NEUTRINO ENERGY FOR ELASTIC EVENTS

The problem of isolation of elastic events was considered in section 3.5. The neutrino energy for these events can be calculated entirely from the lepton vertex, through the formula

$$E = \frac{E^\mu - ({m_\mu}^2/2m_N)}{1 - [(E^\mu - p_x^\mu)/m_N]} \tag{3.15}$$

where m_μ is the muon mass and m_N the target nucleon mass.

The other independent kinematic variables for an elastic event are then given by the formulae

$$x = 1 \tag{3.16}$$

$$Q^2 = 2m_N(E - E^\mu) \tag{3.17}$$

3.7 UNSMEARING

It has been seen in the preceding discussion that it is possible to make an estimate of the kinematic quantities E, x and Q^2 of an event using the observed particles emerging from the interaction. The resulting event distribution in these quantities, which shall be referred to as the "measured" distribution, suffers from the biases inherent in the method of estimation and in other experimental limitations such as the measurement errors in determining the momenta of tracks. In this section the method of "unsmearing", which involves calculation of the desired "true" distributions in E, x and Q^2 from the measured distributions will be discussed.

3.7.1 THE PHILOSOPHY OF UNSMEARING

Unsmearing calculations inevitably rely on the use of Monte Carlo programs to model the known features of the experimental setup. The general problem involves determining the probability that an event which is estimated to have measured values E_m, x_m, ${Q^2}_m$ for E, x and Q^2 possesses true values E_t, x_t, ${Q^2}_t$. This can in principle be achieved by using a Monte Carlo program to generate events with some input distribution in the true quantities, and allowing these events to be "smeared" by simulating the measurement uncertainties such as loss of neutral particles, particle misidentification and momentum measurement errors. The resulting event distribution in E_m, x_m and ${Q^2}_m$ is then compared with the input distribution. Such an approach in effect determines the experimental resolution function R defined by

$$\frac{d^3N(E_m,x_m,Q^2_m)}{dE_m dx_m dQ^2_m} = \int\int\int \frac{d^3N(E_t,x_t,Q^2_t)}{dE_t dx_t dQ^2_t} R(E_m,x_m,Q^2_m;E_t,x_t,Q^2_t) \; dE_t dx_t dQ^2_t \tag{3.18}$$

where $d^3N(E_m,x_m,Q^2_m)/dE_m dx_m dQ^2_m$ is the differential event distribution in E_m, x_m and Q^2_m and $R(E_m,x_m,Q^2_m;E_t,x_t,Q^2_t)$ gives the probability that an event is smeared from true values E_t, x_t, Q^2_t to measured values E_m, x_m, Q^2_m.

Due to finite statistics it is usual to bin the data in E, x and Q^2. Integrated over these bins, (3.18) may be recast in matrix form

$$N^m_{ijk} = \sum_{lmn} S_{ijklmn} N^t_{lmn} \tag{3.19}$$

where N^m_{ijk} is the number of events whose measured value lies in bin i of E, j of x and k of Q^2, and S_{ijklmn} is an element of the "smearing matrix" which contains the same information as the resolution function R introduced above.

Unsmearing of the data event distributions can then be achieved by calculating, using the Monte Carlo, the inverse of matrix S and applying this to the binned data to calculate the true distributions.

The above procedure has the disadvantage that for any practical choice of bins in each variable, the calculation of elements of the unsmearing matrix quickly becomes unmanageable in terms of computer time and space. The problem is traditionally overcome by calculating "unsmearing factors" bin by bin using the simpler equation

$$N^m_{ijk} = S_{ijk} N^t_{ijk} \tag{3.20}$$

In this approach, the value of the S_{ijk} depend to some extent on the choice of input distributions in E_t, x_t and Q^2_t to the Monte Carlo. It is particularly important, therefore, to demonstrate the ability of the Monte Carlo to reproduce the features of the data, and to investigate the sensitivity of the unsmearing factors to the choice of input distributions.

For the extraction of structure functions in bins of x and Q^2, the neutrino energy of the event is integrated over in the calculation of "flux integrals" (see Chapter 5). We are therefore left with an expression for the unsmearing factor in bin j of x and k of Q^2 of

$$U_{jk} = 1/S_{jk} = N^t_{jk}/N^m_{jk} \tag{3.21}$$

with the $N^{T(m)}_{jk}$ defined in analogy with equation (3.20). The factors U_{jk} are then applied to the number of events in bin j, k of the data to obtain the true or unsmeared number of events in that bin.

3.7.2 THE MONTE CARLO

A Monte Carlo developed at the Rutherford Appleton Laboratory [36] specifically with the present experiment in mind was used to simulate CC events under the relevant

experimental conditions. The following is a brief outline of the details of the Monte Carlo, henceforth referred to as CARLO.

The energy E of an event and the position of the interaction within the experimental fiducial volume is chosen according to the neutrino flux distribution in energy and radius given in section 4.2, assuming a linear rise of cross section with energy. At this stage it is decided whether the event is to be elastic or inelastic on the basis of the relative cross sections.

The remaining two independent kinematic variables, x and Q^2, are then generated. In the standard CARLO, the quark and antiquark x distributions are parametrized in the following Q^2 independent manner

$$\begin{aligned} xd_v(x) &= A_d x^{\eta_{1d}}(1-x)^{\eta_{2d}} \\ xu_v(x) &= A_u x^{\eta_{1u}}(1-x)^{\eta_{2u}} \\ xd_s(x) &= A_s(1-x)^{\eta_s} \end{aligned} \tag{3.22}$$

where

$$d_s(x) = \bar{d}_s(x) = u_s(x) = \bar{u}_s(x)$$

$$s(x) = \bar{s}(x) = a d_s(x)$$

$$c(x) = \bar{c}(x)$$

The free parameters in this formulation are η_{1d}, η_{2d}, η_{1u}, η_{2u}, η_s, a and $B = \int_0^1 xF_3 dx / \int_0^1 F_2 dx$ The normalization constants A_d and A_u are fixed by the quark sum rules $\int_0^1 d_v(x)dx = 1$ and $\int_0^1 u_v(x) = 2$, and A_s is function of A_d, A_u, a and B. To ascertain the effect on the unsmearing factors of the inclusion of some scaling violation in the input quark distributions, the above parametrization was replaced by that of Buras and Gaemers [19] and the unsmearing calculation repeated. For low Q^2 ($Q^2 < 1.8$ GeV^2/c^2) an extrapolation based on the parametrization of Perkins, Schreiner and Scott [37] was used. The effect of changing the input x and Q^2 distributions is discussed in the following section. For an elastic event, Q^2 was generated according to the known elastic form factors.

Specification of E, x and Q^2 completely determines the lepton vertex and hence the muon 4-vector. The standard CARLO was modified at this point to allow the option of

including radiative corrections to the muon 4-vector, using the calculation of de Rujula et al. [38] implemented in the manner suggested by Scott [39]. If on the basis of the cross sections of reference [38] a hard photon was radiated by the muon, this photon was reassigned to the hadron shower and tracked through the chamber liquid to check for possible conversion, in an identical manner to photons originating from the hadron vertex. The muon energy was reduced by the energy of the emitted photon, but the direction preserved, as the radiation is essentially collinear. In a typical sample of CARLO events of approximately 180000, the number of muons radiating such a photon was found to be approximately 19000. The mean energy of the radiated photons was 1.50 GeV.

In the standard CARLO the muon is tracked through the chamber and surrounds to determine whether a hit in both planes of the EMI would be registered. This was disabled for the present application, as a correction is applied to the data in the manner of section 3.3.1.

The next stage in event generation is the treatment of the hadronization at the lower vertex. CARLO has the capacity to assign Fermi momentum to the target nucleon following Bodek and Ritchie [40]. Motivated by the discussion of section 1.6 the effect of including and omitting this feature will be investigated in the following section.

Charged and neutral hadrons are generated using a longitudinal phase space model. Reinteraction of hadrons within the neon nucleus is crudely modelled and can affect the multiplicity distributions of emerging hadrons. Charged particles are tracked a short distance (0.4 cm) to determine whether a secondary interaction occurs sufficiently close to the primary vertex to cause tracks from this interaction to be confused with those from the primary. Neutral particles are tracked to determine whether they decay, interact, or (in the case of photons from π^0 decay) convert within the chamber. Finally, all particles are smeared to take into account track measurement errors, misidentification and scanning losses for neutrals.

The events generated with the above prescription were then treated in the same manner as the data to estimate the measured kinematic variables from the observed final state

particles.

The degree to which CARLO is capable of representing the observed distributions in various kinematic quantities is illustrated in Figures 3.2a - u for the neutrino sample and in Figures 3.3a - u for the antineutrino sample. In each case, the distribution given by CARLO is represented by the continuous curve and the observed data distribution by the points with error bars. Agreement between the two distributions is considered satisfactory for all inclusive quantities. Less satisfactory agreement is obtained for the multiplicity distributions, and indicates the difficulty involved in successfully modelling the complex reinteraction processes within a nucleus such as neon. To a good approximation, the unsmearing calculation is not sensitive to such variations in these non-inclusive quantities, except where individual exclusive channels are involved, as is the case for elastic events. This will be discussed further below.

3.7.3 THE UNSMEARING FACTORS

Using the prescription described earlier in this section, unsmearing factors for the neutrino and antineutrino samples were calculated and are presented in Tables 3.4a and b. The choice of binning in x and Q^2 was governed by the observed distribution of events in these quantities to be given in section 5.2. Approximately 200000 CARLO events were generated for both the neutrino and antineutrino samples. Errors quoted are statistical only and result from the finite CARLO event samples used.

The sensitivity of the unsmearing factors to several previously mentioned effects is also indicated in Tables 3.4a and b. These are the effect of i) replacement of the input quark distributions by a set based on the parametrization of Buras and Gaemers [19], with a value of $\Lambda = 300$ MeV/c. ii) including the generation of Fermi motion for the target nucleon within CARLO, and iii) including radiative corrections in CARLO. In each case the entry represents the change in the unsmearing factor induced by actions i) to iii).

The replacement of any given set of input quark distributions by another is a measure of the systematic uncertainty of the method of structure function extraction adopted in

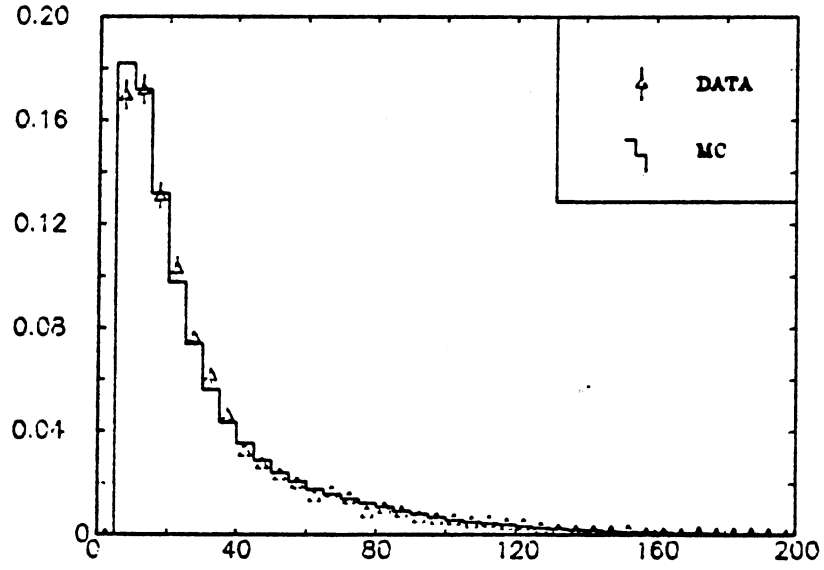

(a) MUON MOMENTUM (GeV/c)

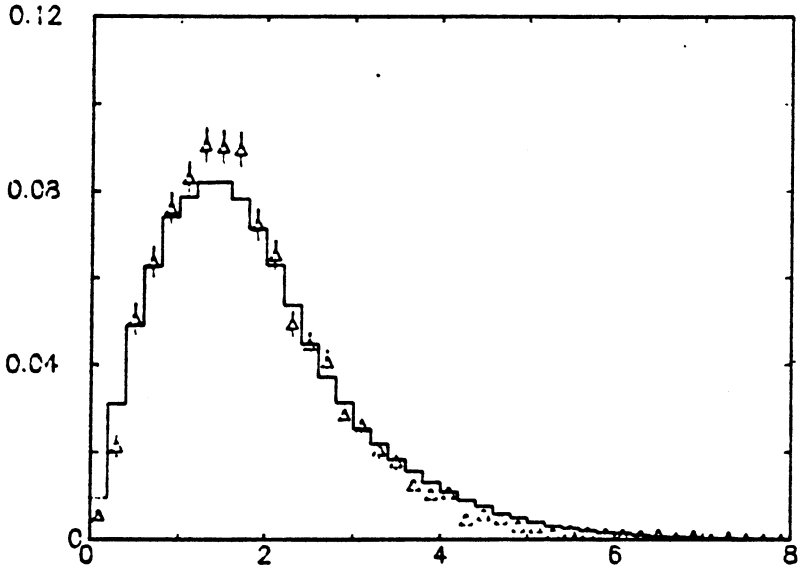

(b) PT OF MUON (GeV/c)

FIG 3.2 NEUTRINO MONTE CARLO DATA COMPARISON

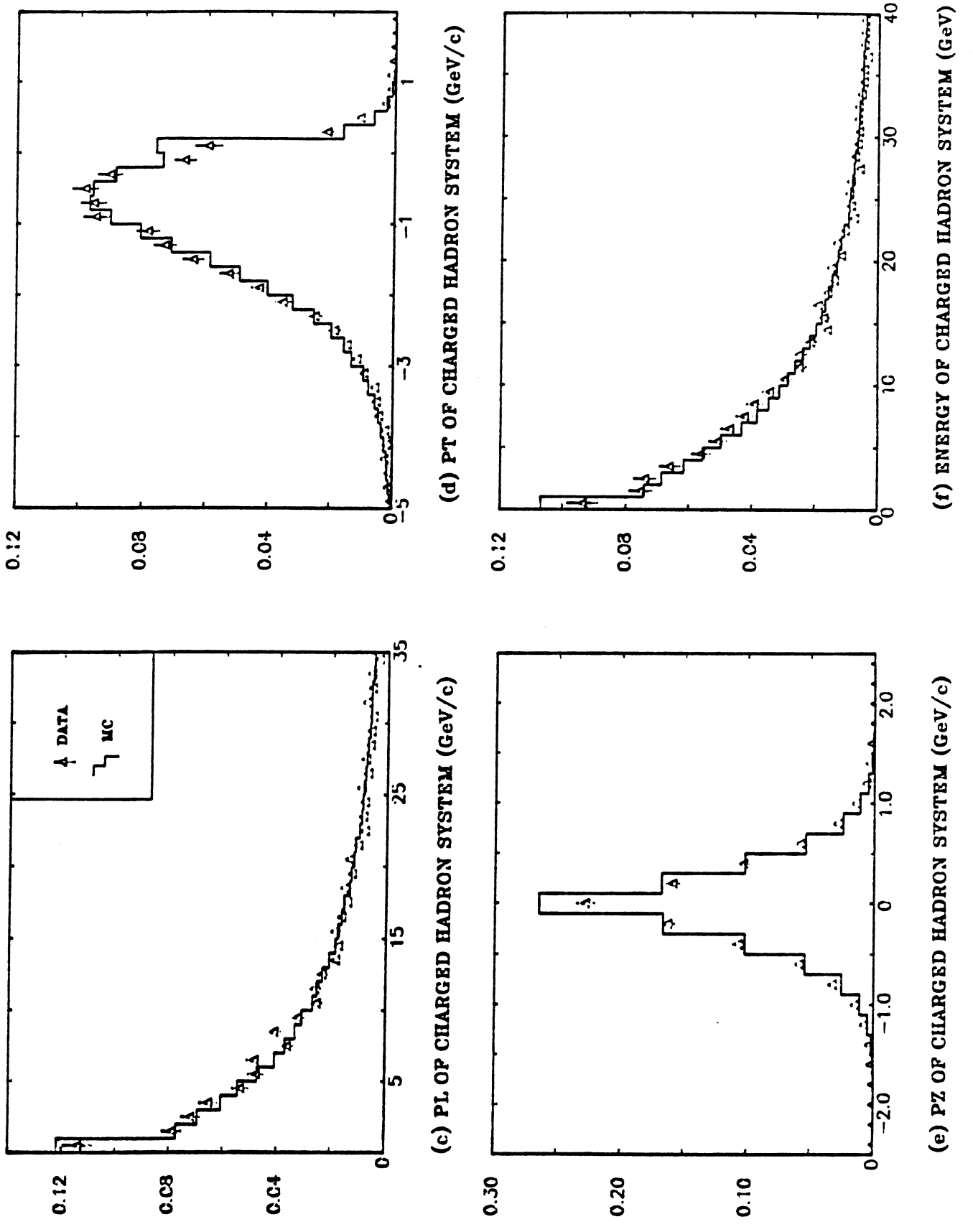

FIG 3.2 NEUTRINO MONTE CARLO DATA COMPARISON (CONT.)

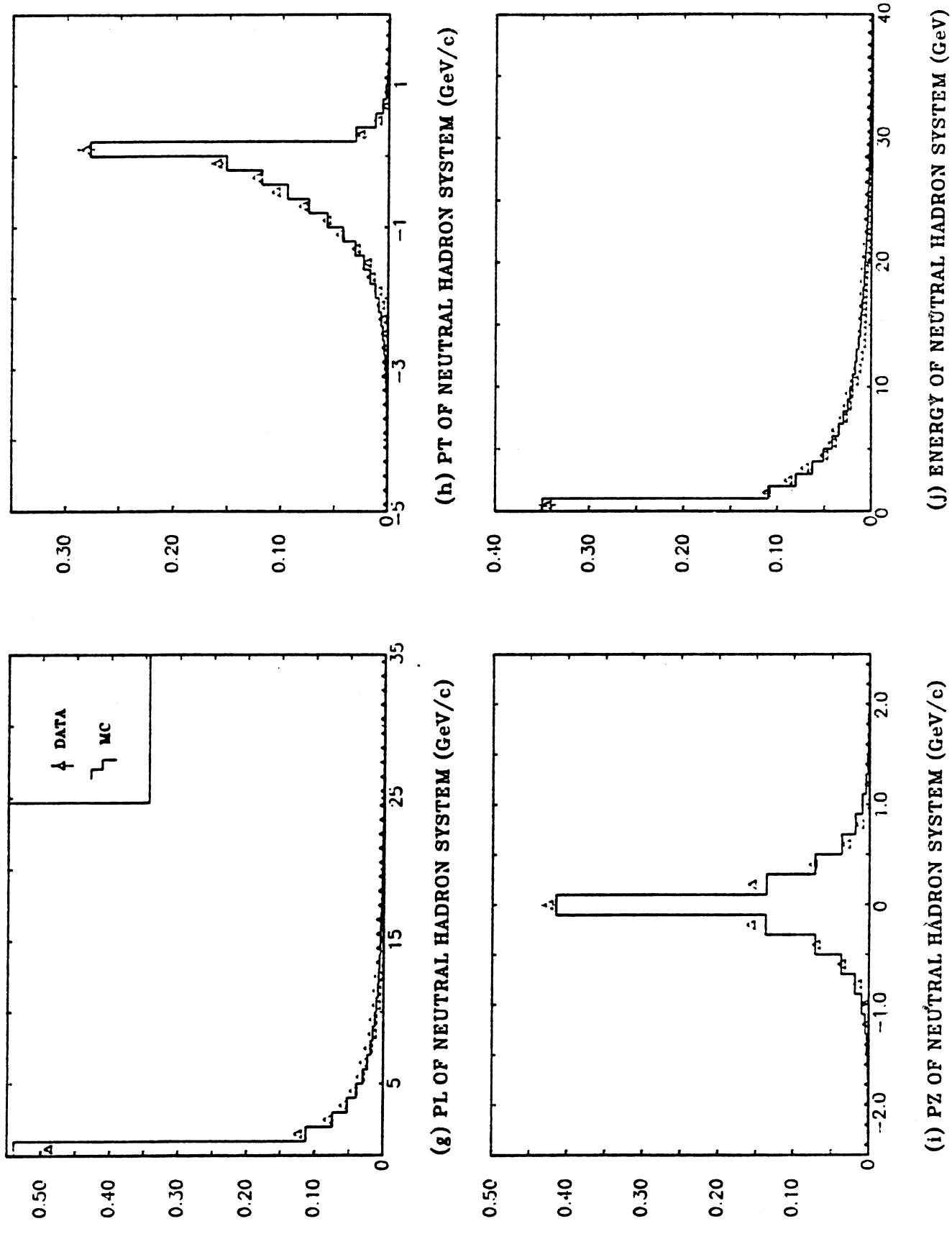

FIG 3.2 NEUTRINO MONTE CARLO DATA COMPARISON (CONT.)

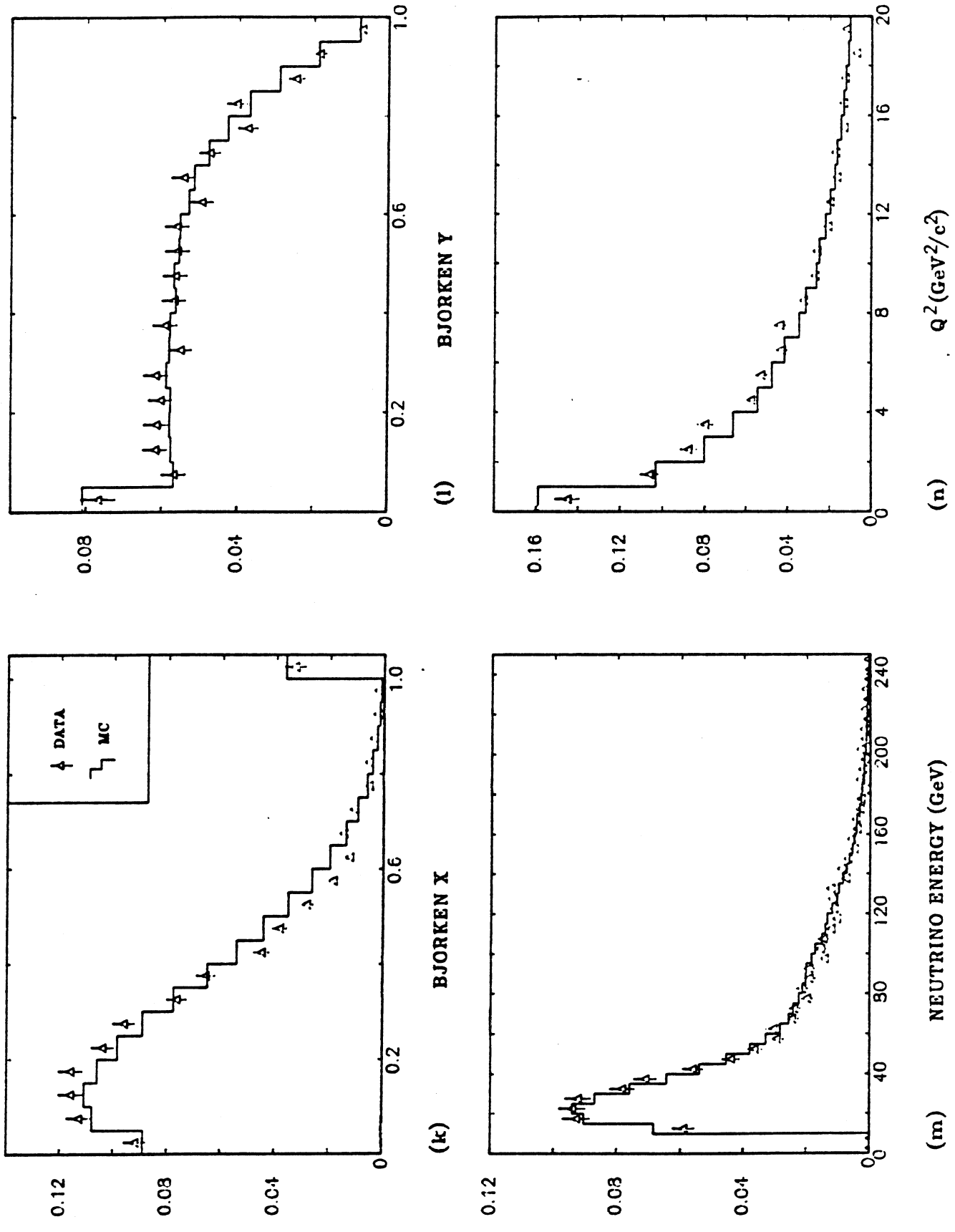

FIG 3.2 NEUTRINO MONTE CARLO DATA COMPARISON (CONT.)

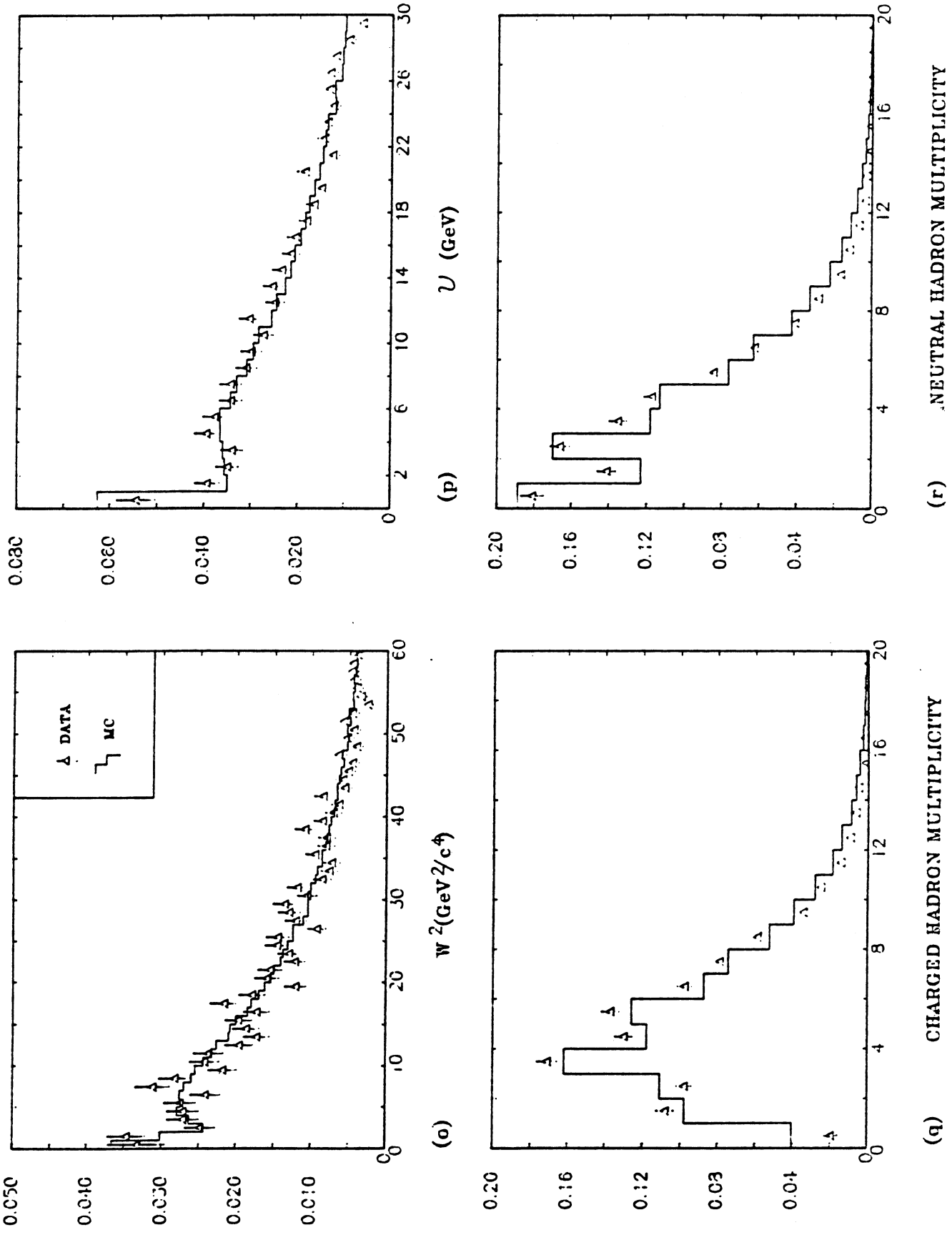

FIG 3.2 NEUTRINO MONTE CARLO DATA COMPARISON (CONT.)

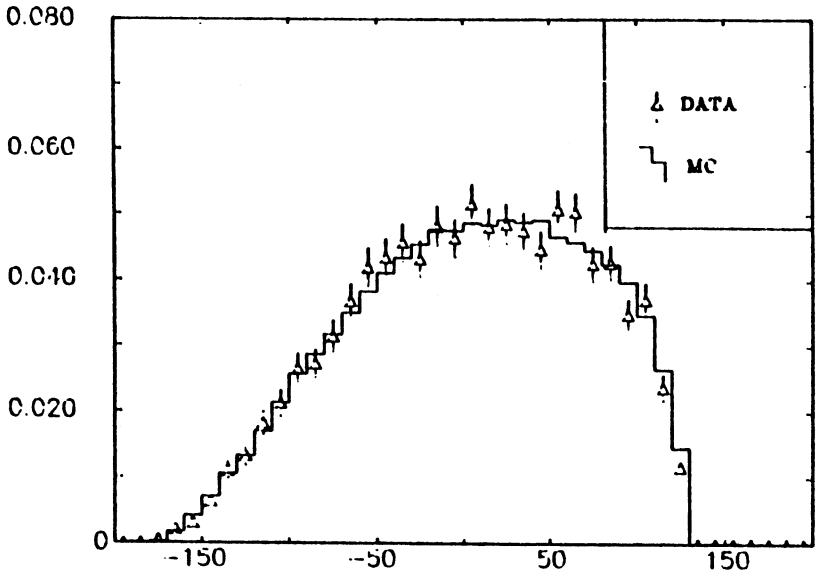

(s) X COCRDINATE OF VERTEX (cm)

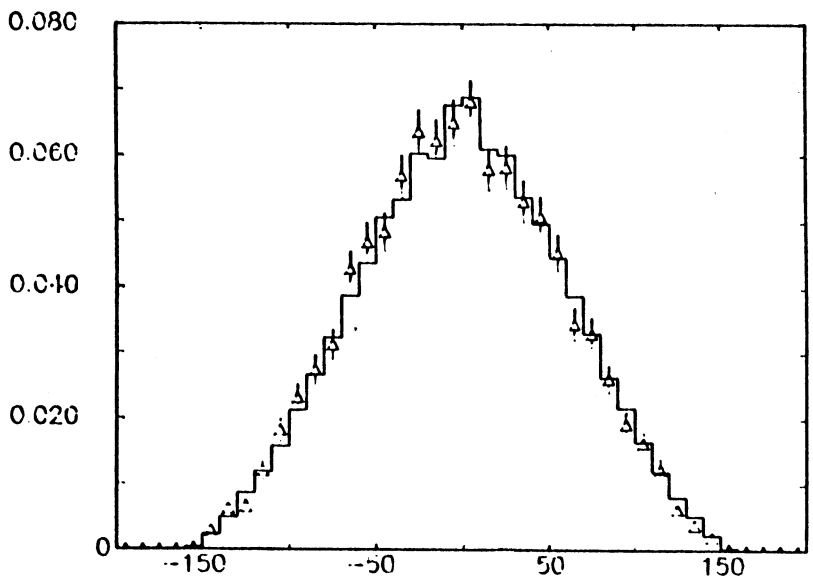

(t) Y COORDINATE OF VERTEX (cm)

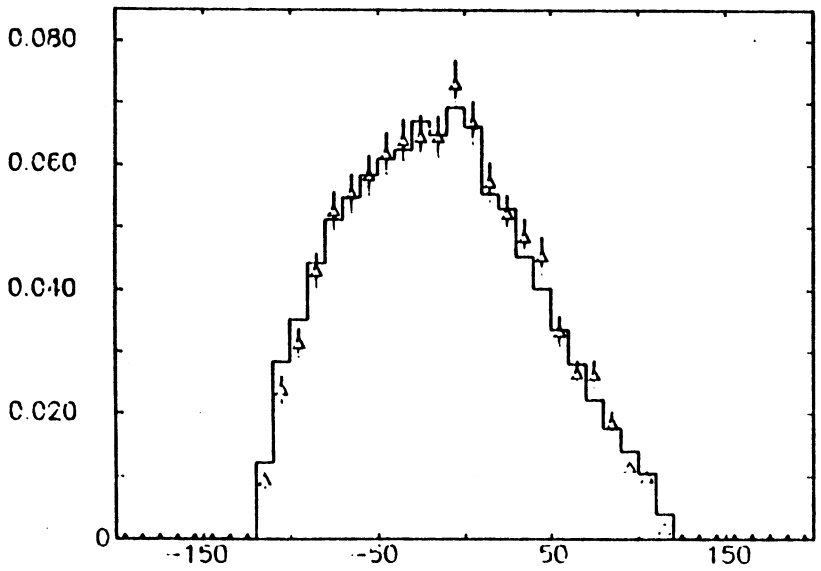

(u) Z COORDINATE OF VERTEX (cm)

FIG 3.2 NEUTRINO MONTE CARLO DATA COMPARISON (CONT.)

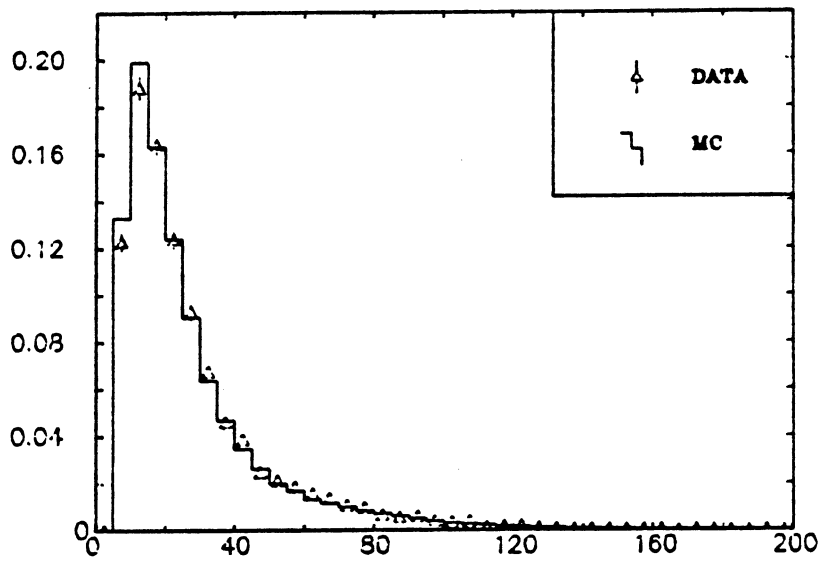

(a) MUON MOMENTUM (GeV/c)

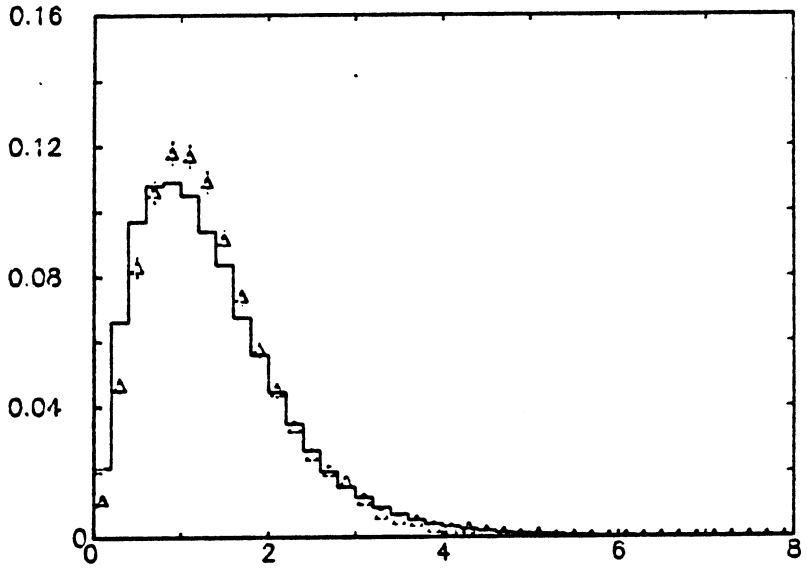

(b) PT OF MUON (GeV/c)

FIG 3.3 ANTINEUTRINO MONTE CARLO DATA COMPARISON

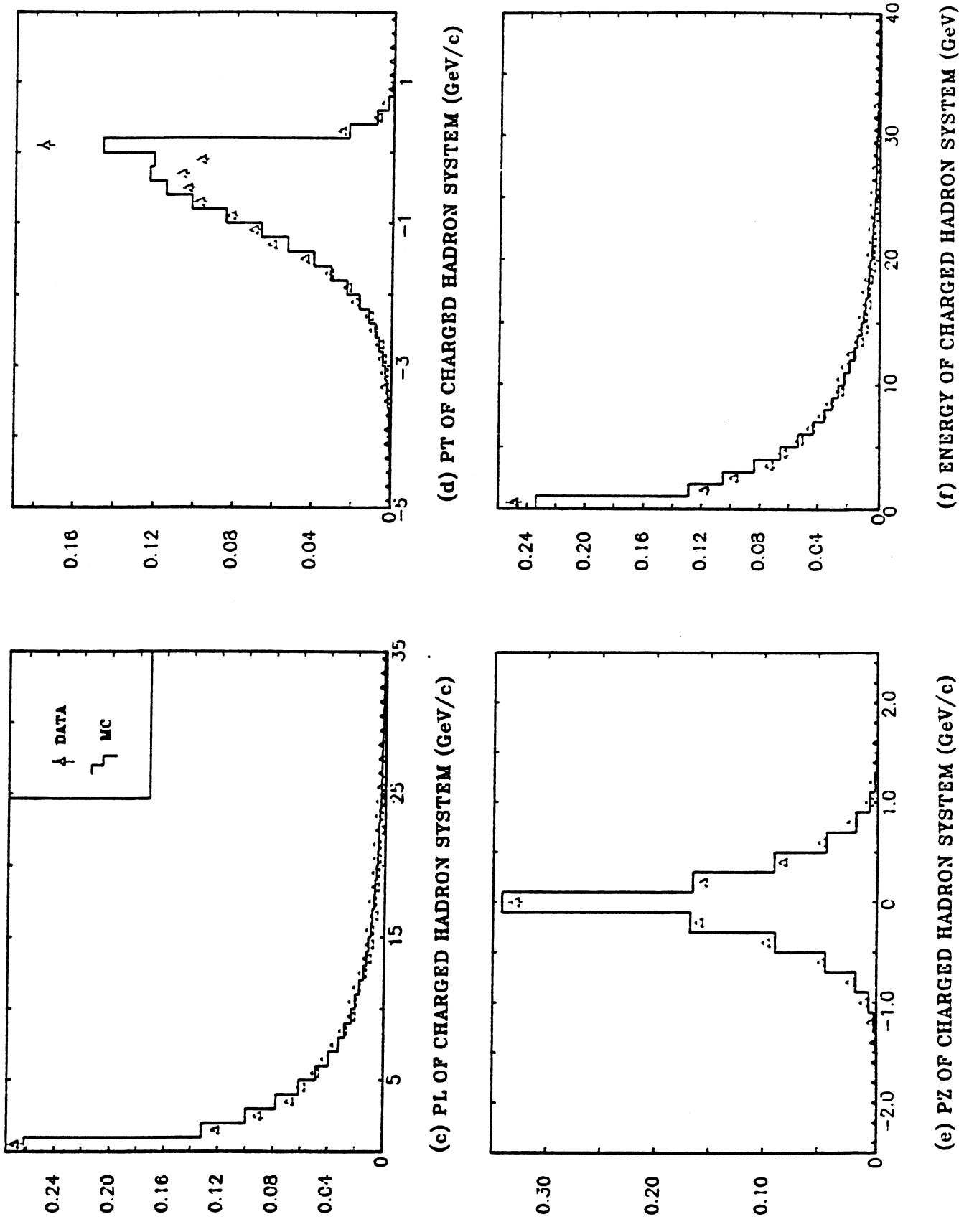

FIG 3.3 ANTINEUTRINO MONTE CARLO DATA COMPARISON (CONT.)

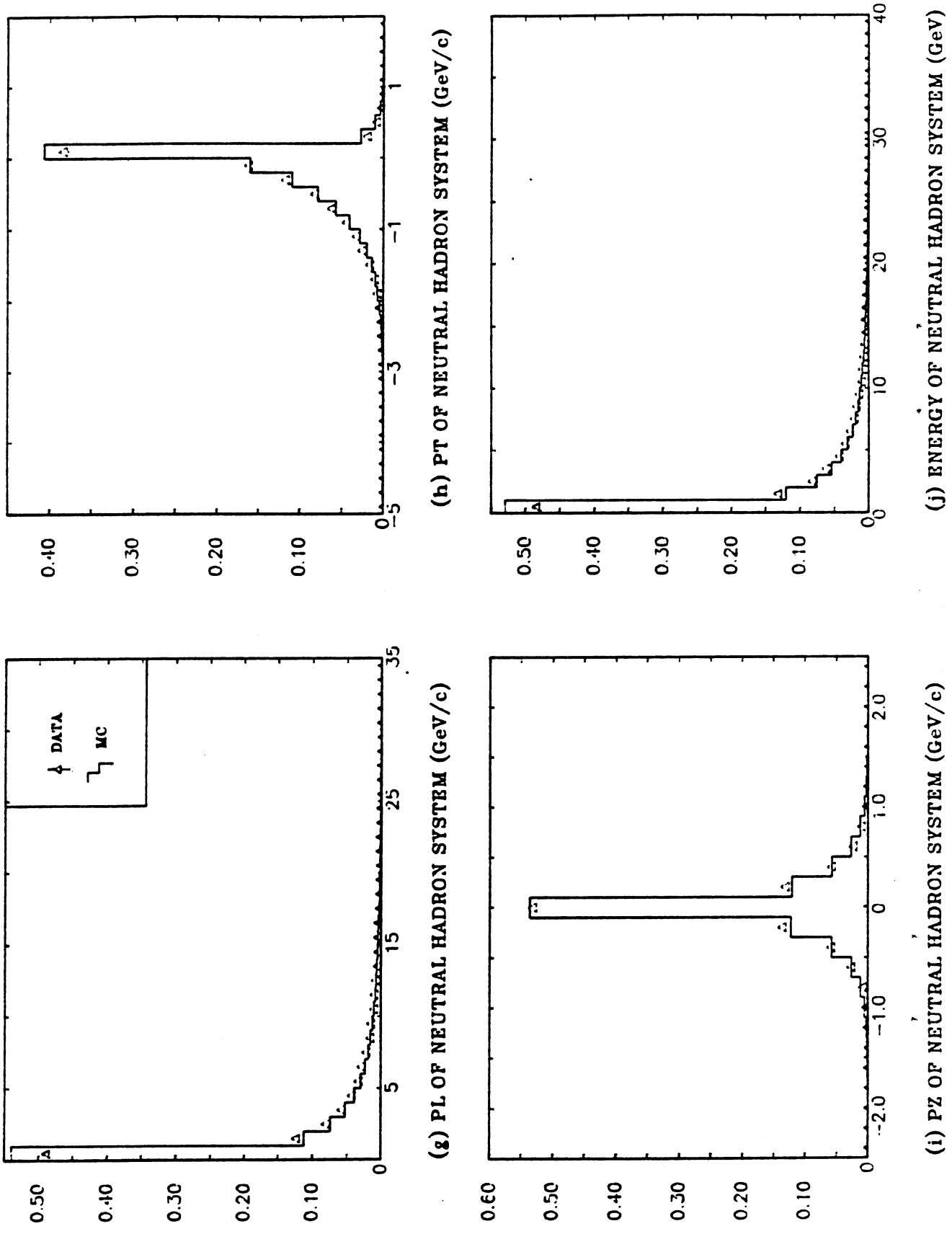

FIG 3.3 ANTINEUTRINO MONTE CARLO DATA COMPARISON (CONT.)

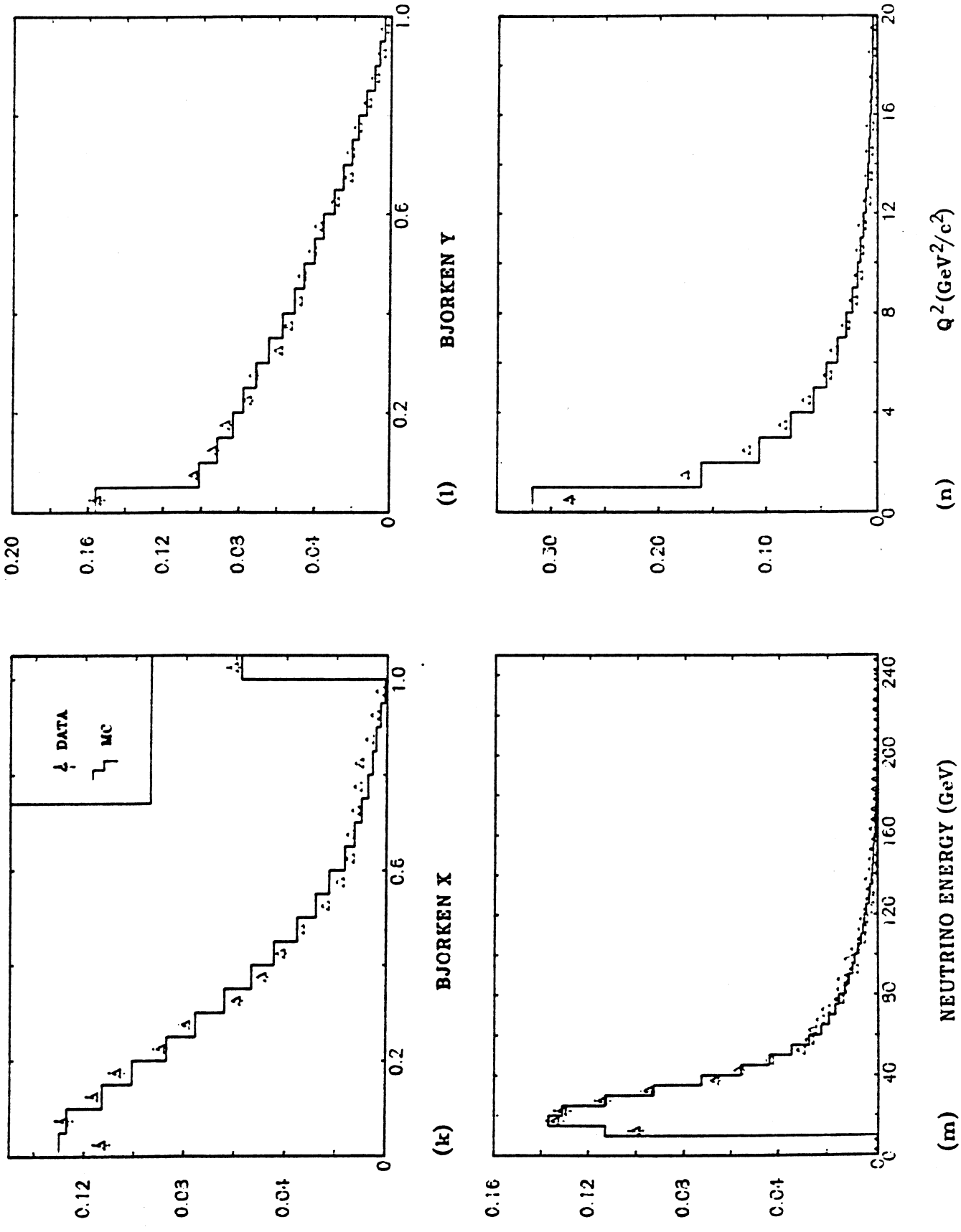

FIG 3.3 ANTINEUTRINO MONTE CARLO DATA COMPARISON (CONT.)

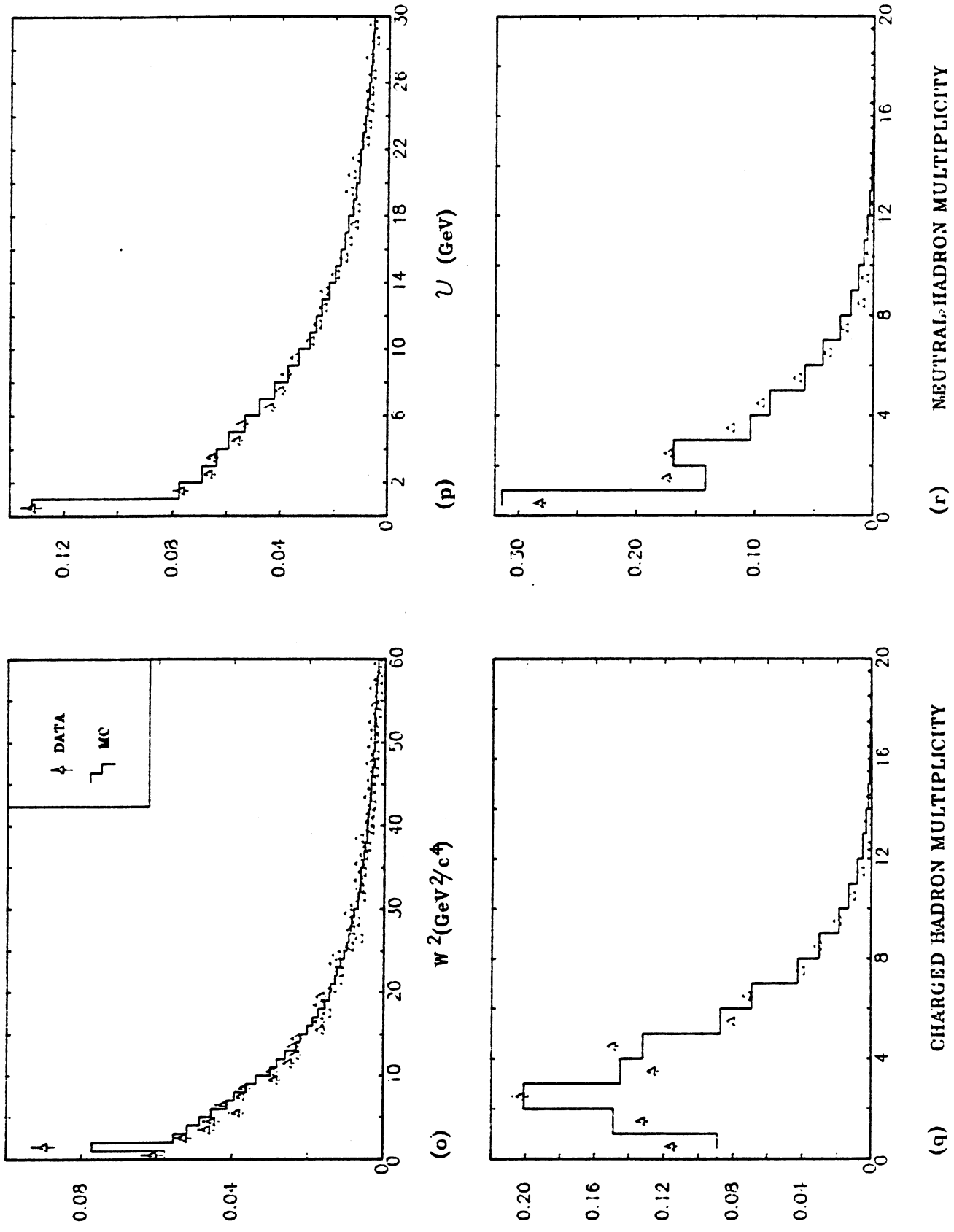

FIG 3.3 ANTINEUTRINO MONTE CARLO DATA COMPARISON (CONT.)

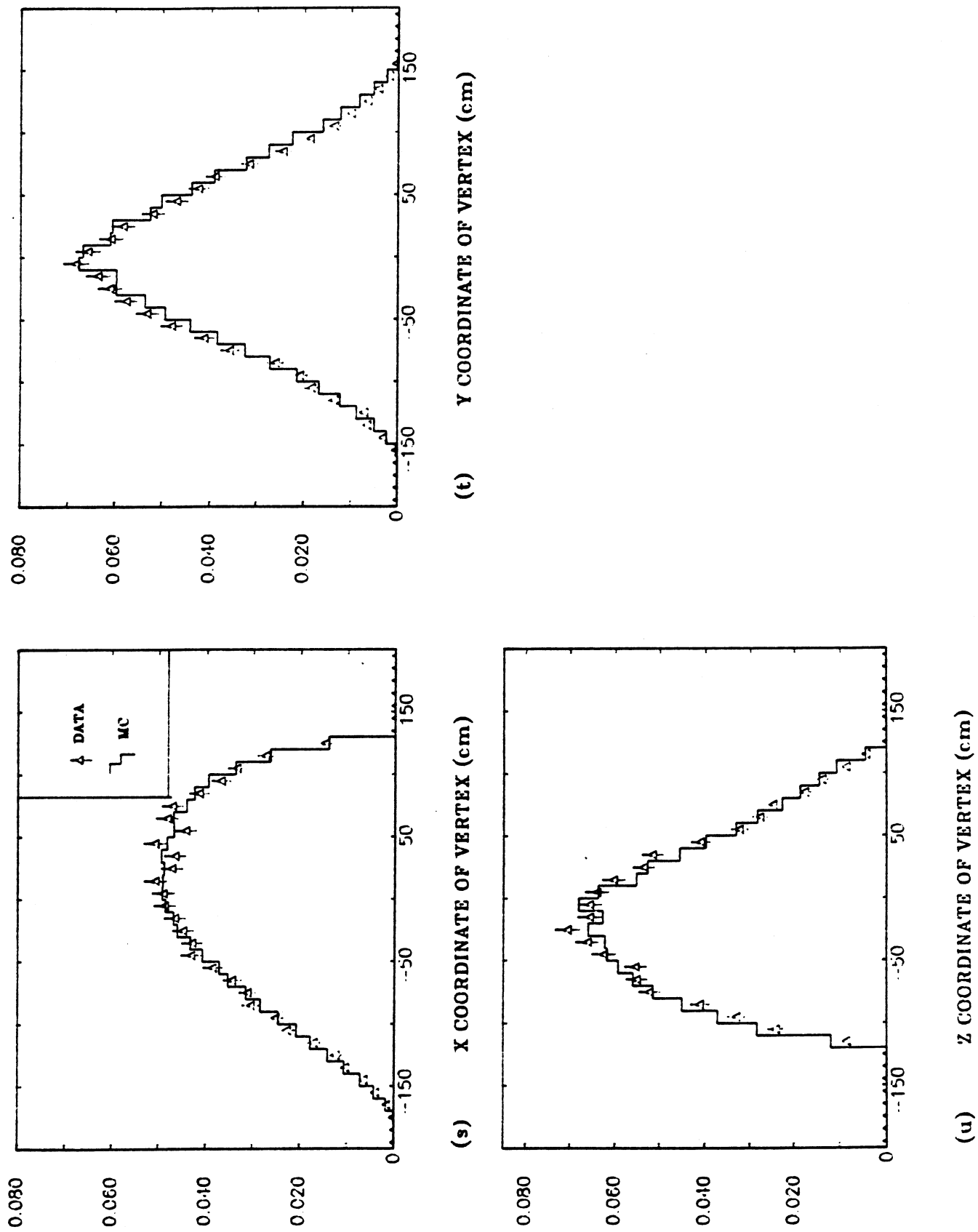

FIG 3.3 ANTINEUTRINO MONTE CARLO DATA COMPARISON (CONT.)

Table 3.4a : Neutrino unsmearing factors

$Q^2(GeV^2/c^2)$	x	Unsmearing Factor	(i)	(ii)	(iii)
0.–.4	0.–.1	1.221 ± 0.019	−0.060	+0.010	−0.017
	.1–.2	1.420 ± 0.047	+0.005	+0.055	+0.220
	.2–.3	1.440 ± 0.073	+0.308	−0.169	+0.217
	.3–.4	1.158 ± 0.081	+0.397	−0.454	+0.011
	.4–.6	0.343 ± 0.031	+0.244	−0.098	+0.032
	.6–1.	-	-	-	-
	Elastic	0.421 ± 0.013	+0.107	+0.054	−0.002
.4–1.	0.–.1	1.079 ± 0.018	−0.021	−0.069	−0.040
	.1–.2	1.178 ± 0.029	−0.043	+0.201	+0.111
	.2–.3	1.392 ± 0.049	+0.006	−0.157	+0.213
	.3–.4	1.456 ± 0.072	+0.075	+0.011	+0.172
	.4–.6	1.158 ± 0.061	+0.666	−0.164	+0.150
	.6–1.	0.175 ± 0.018	+0.130	−0.064	−0.026
	Elastic	0.438 ± 0.019	+0.001	−0.001	+0.019
1.–2.	0.–.1	1.005 ± 0.017	+0.013	+0.070	−0.045
	.1–.2	1.094 ± 0.021	−0.037	−0.027	+0.048
	.2–.3	1.181 ± 0.031	−0.040	+0.047	+0.118
	.3–.4	1.256 ± 0.046	+0.044	+0.224	+0.028
	.4–.6	1.194 ± 0.049	+0.145	+0.044	+0.161
	.6–1.	0.422 ± 0.031	+0.195	−0.119	−0.083
	Elastic	0.361 ± 0.024	−0.010	−0.007	+0.047
2.–4.	0.–.1	0.978 ± 0.017	+0.043	−0.038	−0.106
	.1–.2	1.054 ± 0.016	−0.018	+0.012	+0.014
	.2–.3	1.048 ± 0.020	+0.019	+0.021	+0.102
	.3–.4	1.133 ± 0.028	−0.024	+0.029	+0.064
	.4–.6	1.073 ± 0.030	+0.009	+0.027	+0.088
	.6–1.	0.587 ± 0.033	+0.127	−0.046	+0.007
	Elastic	0.284 ± 0.031	+0.016	−0.014	+0.095

(i) Change due to using Buras and Gaemers Input Distributions
(ii) Change due to including Fermi Motion
(iii) Change due to including radiative corrections
No entry indicates a lack of data in this bin

Table 3.4a (cont.)

$Q^2(GeV^2/c^2)$	x	Unsmearing Factor	(i)	(ii)	(iii)
4.–8.	0.–.1	0.884 ± 0.019	+0.062	+0.014	−0.089
	.1–.2	1.031 ± 0.015	+0.004	+0.002	+0.005
	.2–.3	1.065 ± 0.017	−0.028	+0.017	+0.033
	.3–.4	1.052 ± 0.021	−0.010	−0.009	+0.077
	.4–.6	1.054 ± 0.022	−0.008	+0.054	+0.057
	.6–1.	0.782 ± 0.032	+0.052	−0.137	+0.018
	Elastic	0.202 ± 0.046	+0.066	+0.038	+0.116
8.–16.	0.–.1	0.855 ± 0.025	+0.013	−0.029	−0.168
	.1–.2	0.980 ± 0.017	+0.022	+0.005	−0.037
	.2–.3	1.028 ± 0.017	+0.010	+0.074	+0.015
	.3–.4	1.045 ± 0.019	−0.018	+0.003	+0.012
	.4–.6	1.034 ± 0.018	+0.017	−0.063	+0.081
	.6–1.	0.842 ± 0.028	+0.010	−0.079	+0.080
	Elastic	0.206 ± 0.085	+0.118	−0.116	+0.203
16.–64.	0.–.1	0.386 ± 0.022	+0.009	+0.017	−0.117
	.1–.2	0.941 ± 0.019	+0.005	+0.085	−0.097
	.2–.3	1.026 ± 0.016	−0.007	+0.018	−0.024
	.3–.4	1.020 ± 0.016	+0.008	+0.020	+0.019
	.4–.6	1.033 ± 0.014	−0.005	+0.021	+0.038
	.6–1.	0.920 ± 0.021	+0.021	−0.136	+0.074
	Elastic	0.100 ± 0.105	−0.100	+0.136	−0.100
64.–200	0.–.1	–	–	–	–
	.1–.2	0.076 ± 0.018	+0.003	−0.005	−0.023
	.2–.3	0.568 ± 0.039	−0.084	+0.094	−0.105
	.3–.4	0.876 ± 0.039	+0.029	+0.021	−0.027
	.4–.6	1.028 ± 0.029	+0.007	−0.026	+0.037
	.6–1.	1.030 ± 0.041	−0.041	−0.078	+0.024
	Elastic	–	–	–	–

Table 3.4b : Antineutrino unsmearing factors

$Q^2(GeV^2/c^2)$	x	Unsmearing Factor	(i)	(ii)	(iii)
0.–.4	0.–.1	1.221 ± 0.013	−0.054	+0.021	+0.003
	.1–.2	1.347 ± 0.029	+0.030	+0.014	+0.148
	.2–.3	1.329 ± 0.042	+0.263	−0.138	+0.197
	.3–.4	1.072 ± 0.048	+0.434	−0.236	+0.037
	.4–.6	0.337 ± 0.018	+0.265	−0.131	+0.011
	.6–1.	-	-	-	-
	Elastic	0.486 ± 0.010	+0.091	+0.010	−0.046
.4–1.	0.–.1	1.059 ± 0.014	−0.011	+0.031	−0.025
	.1–.2	1.175 ± 0.020	−0.033	+0.043	+0.106
	.2–.3	1.306 ± 0.031	+0.001	+0.190	+0.126
	.3–.4	1.298 ± 0.041	+0.077	+0.020	+0.207
	.4–.6	1.129 ± 0.038	+0.355	−0.130	−0.032
	.6–1.	0.143 ± 0.010	+0.076	−0.065	−0.009
	Elastic	0.698 ± 0.021	−0.043	−0.030	−0.061
1.–2.	0.–.1	0.963 ± 0.014	+0.026	−0.017	−0.073
	.1–.2	1.099 ± 0.017	−0.048	−0.056	+0.050
	.2–.3	1.166 ± 0.023	−0.038	+0.172	+0.133
	.3–.4	1.236 ± 0.032	+0.020	−0.049	+0.146
	.4–.6	1.173 ± 0.032	+0.037	−0.161	+0.038
	.6–1.	0.306 ± 0.014	+0.132	−0.048	−0.019
	Elastic	0.993 ± 0.054	+0.040	−0.105	+0.010
2.–4.	0.–.1	0.840 ± 0.015	+0.102	+0.022	−0.086
	.1–.2	1.047 ± 0.015	−0.038	−0.007	+0.010
	.2–.3	1.098 ± 0.018	−0.029	−0.013	+0.072
	.3–.4	1.109 ± 0.022	+0.059	+0.128	+0.142
	.4–.6	1.110 ± 0.023	+0.045	−0.059	+0.097
	.6–1.	0.534 ± 0.021	+0.104	−0.061	−0.014
	Elastic	1.634 ± 0.174	+0.039	−0.147	+0.126

(i) Change due to using Buras and Gaemers Input Distributions
(ii) Change due to including Fermi Motion
(iii) Change due to including radiative corrections
No entry indicates a lack of data in this bin

Table 3.4b (cont.)

$Q^2(GeV^2/c^2)$	x	Unsmearing Factor	(i)	(ii)	(iii)
4.–8.	0.–.1	0.701 ± 0.018	+0.093	+0.043	−0.100
	.1–.2	0.978 ± 0.015	−0.006	+0.035	−0.037
	.2–.3	1.046 ± 0.017	−0.026	+0.041	+0.048
	.3–.4	1.097 ± 0.021	−0.020	−0.077	+0.056
	.4–.6	1.083 ± 0.020	+0.015	+0.604	+0.091
	.6–1.	0.773 ± 0.026	+0.033	−0.495	+0.001
	Elastic	2.304 ± 0.575	−0.573	−0.974	−1.304
8.–16.	0.–.1	0.518 ± 0.025	+0.086	+0.029	−0.164
	.1–.2	0.905 ± 0.022	+0.023	+0.121	−0.106
	.2–.3	1.013 ± 0.022	−0.023	+0.101	+0.002
	.3–.4	1.039 ± 0.023	−0.024	+0.010	+0.048
	.4–.6	1.059 ± 0.021	+0.024	+0.048	+0.072
	.6–1.	0.933 ± 0.032	−0.030	−0.232	+0.027
	Elastic	1.125 ± 0.547	+1.475	+0.069	+0.097
16.–64.	0.–.1	0.104 ± 0.015	+0.025	+0.006	−0.030
	.1–.2	0.719 ± 0.030	−0.017	+0.115	−0.143
	.2–.3	0.939 ± 0.029	−0.058	−0.187	−0.072
	.3–.4	0.976 ± 0.029	−0.008	+0.062	+0.047
	.4–.6	1.025 ± 0.024	+0.018	+0.020	+0.044
	.6–1.	0.962 ± 0.034	+0.011	−0.148	+0.077
	Elastic	2.000 ± 2.450	−2.000	−1.308	−2.000
64.–200	0.–.1	–	–	–	–
	.1–.2	0.014 ± 0.014	−0.014	+0.006	−0.014
	.2–.3	0.220 ± 0.068	−0.115	−0.003	−0.134
	.3–.4	0.564 ± 0.106	−0.064	+0.054	−0.070
	.4–.6	0.895 ± 0.102	−0.013	+0.119	+0.039
	.6–1.	0.945 ± 0.129	−0.016	−0.162	+0.047
	Elastic	–	–	–	–

this thesis, as it has been noted in section 3.7.1 that the use of unsmearing factors as opposed to the full resolution function can in principle introduce a dependence of the unsmearing factors on the input distributions. On the basis of Table 3.4, the use of a Buras and Gaemers parametrization induces changes in the unsmearing factors in general at less than the 10% level. When considering the entries in column (i) of this Table, due attention should be paid to the statistical errors on the unsmearing factors, which is in some cases comparable in size to the induced change. A more significant variation, of from 15% to 100%, can be observed in the region $Q^2 <\sim 2$ GeV^2/c^2, $x > .2$. The Buras and Gaemers parametrization does not claim to apply for low Q^2, and as pointed out above, an extrapolation based on reference [37] was used for $Q^2 < 1.8$ GeV^2/c^2. This region of the kinematic plane, at low W^2, consists mainly of low multiplicity events and is dominated by resonance channels, which neither a simple input $x - Q^2$ distribution nor longitudinal phase space model of hadron production can effectively model. The unsmearing factors in this region are therefore subject to very large systematic uncertainties, which must be taken into account when quoting values for the structure functions. It is not believed that a reliable estimate of F_2 and xF_3 can be made in this region.

Changes induced in the unsmearing factors by the inclusion of radiative corrections are in general at less than the 5 - 10% level. For the lowest x bin, however, the unsmearing factor is affected significantly as Q^2 increases, particularly in the bin $16 < Q^2 < 64$ GeV^2/c^2, where the increase is 30% for the neutrino case and 29% for the antineutrino case.

The inclusion of Fermi motion has a significant effect on the unsmearing factors only at high x, where an increase of the order of 25% can be observed. It should be noted that Fermi motion as implemented in CARLO for the present calculation of unsmearing factors includes the virtual mass assignment to the target nucleon of Bodek and Ritchie.

The effect on the measured structure functions F_2 and xF_3 of these systematic changes to the unsmearing factors will be illustrated in Chapter 5.

The following remark on the unsmearing factors quoted above concerns their actual numerical magnitude. Within the kinematic region $0 < Q^2 < 16$ GeV^2/c^2 and $x < .6$ the

unsmearing factors in general vary nowhere from unity by greater than $\sim 25\%$. For $x >$ .6, however, the unsmearing factors are markedly less than unity for $Q^2 < 4$ GeV^2/c^2, becoming in the extreme case < 0.1 for the bin $.6 < x < 1.$, $.4 < Q^2 < 1.$ GeV^2/c^2. Similar behaviour is observed at low x in the highest Q^2 bin. Large unsmearing factors are treated with extreme caution in structure function analyses. The analysis of the CDHS collaboration [5], for example, excludes all bins for which the unsmearing correction differs from unity by more than 40%. What is strictly relevant here is the systematic error that is assigned to the unsmearing factor rather than the magnitude of the factor itself. As it is believed that the high x bin can contribute information to the body of structure function knowledge, it is retained in the subsequent analysis despite the large unsmearing corrections, with the caveat that the systematic uncertainties in the correction in this region are potentially large. This is particularly true for low Q^2, which is dominated by resonance and elastic channels which are not adequately reproduced by the Monte Carlo. This point will also be taken up in Chapter 5 when the structure functions are calculated.

In the discussion above, systematic uncertainty in the values of the unsmearing factors obtained using the CARLO program have been investigated in some detail. Nevertheless, further systematic uncertainty must also exist in the unsmearing factors of a form which is "built in" or inherent to the CARLO program by the nature of the event generation and smearing employed. This can only be investigated by use of an independent Monte Carlo program or method. Such a method exists for the present experiment [41], and a set of unsmearing factors predicted by this method is reproduced with permission in Tables 3.5a,b.

The essence of the method upon which the unsmearing factors in Tables 3.5a,b are based is the construction of a likelihood function for an event with a given set of observed physical variables E^μ, p_y^μ, p_x^s, p_y^s, p_z^s, which expresses the probability that such an event has true kinematic variables with values E, x and y. An analytic form for the input quark distributions (in this particular case simple quark-parton model formulae) in terms of x and y, in addition to an analytic function parametrizing the relationship between an estimate of the neutrino energy E (in this case obtained using the Myatt method) and

the true neutrino energy, is used in constructing the likelihood function. A simultaneous log likelihood fit to the parameters specifying the input quark distributions and those specifying the smearing is performed by summing over all events in the data sample, weighted appropriately for scan losses and EMI acceptances. The values obtained for the parameters specifying the smearing from the likelihood fit can then be used to calculate unsmearing factors by generating "events" using this parametrization. In this sense the method may be viewed as employing a Monte Carlo which models the total hadron final state, the few well specified parameters of the model being obtained from a fit to the observed data. This is in contrast to the CARLO program, which models the hadron final state in detail, and chooses values for the "parameters" of the model by tuning generated distributions to reproduce those obtained from the data.

A comparison of the unsmearing factors of Tables 3.4 and 3.5 indicates a good general agreement over most of the kinematic plane. Where differences occur they must be taken as a measure of the systematic uncertainty in the unsmearing factors. The most notable differences occur in the region of high x and low Q^2, which has been discussed above in connection with the CARLO program alone. This adds weight to the statement made there that the structure function evaluation in this region of the kinematic plane is subject to large systematic uncertainties.

Table 3.5a : Neutrino Unsmearing Factors from Likelihood Fit [41]

		Q^2 (GeV^2/c^2)							
		0.–.4	.4–1.	1.–2.	2.–4.	4.–8.	8.–16.	16.–64.	64.–200.
	0.–.1	1.077±.097	1.095±.088	1.059±.077	0.960±.075	0.859±.075	0.762±.089	0.524±.095	–
	.1–.2	1.032±.194	1.152±.130	1.176±.110	1.073±.071	1.023±.068	0.945±.071	0.822±.073	0.305±.115
x	.2–.3	1.001±.069	1.133±.199	1.169±.146	1.186±.102	1.088±.079	1.029±.075	0.942±.067	0.657±.175
	.3–.4	0.949±.386	0.991±.204	1.085±.200	1.219±.138	1.090±.098	1.056±.092	0.998±.072	0.886±.202
	.4–.6	0.673±.222	0.843±.185	0.855±.163	0.993±.124	1.095±.117	1.086±.102	1.046±.080	0.998±.153
	.6–1.	–	0.229±.060	0.208±.049	0.347±.071	0.543±.083	0.833±.135	0.889±.122	1.067±.290
	Elastic	0.979±.180	0.951±.188	0.842±.223	0.649±.299	0.354±.500	0.116±.125	0.030±.022	–

Table 3.5b : Antineutrino Unsmearing Factors from Likelihood Fit [41]

		Q^2 (GeV^2/c^2)							
		0.–.4	.4–1.	1.–2.	2.–4.	4.–8.	8.–16.	16.–64.	64.–200.
	0.–.1	1.074±.054	1.083±.054	1.013±.054	0.848±.050	0.718±.060	0.626±.079	0.261±.058	–
	.1–.2	1.074±.100	1.164±.079	1.128±.064	1.064±.055	0.954±.055	0.846±.070	0.625±.085	0.010±.036
x	.2–.3	1.092±.144	1.328±.121	1.256±.090	1.154±.069	1.063±.066	0.993±.078	0.866±.100	0.337±.156
	.3–.4	0.982±.177	1.189±.153	1.186±.120	1.189±.094	1.141±.083	1.035±.092	0.962±.114	0.873±.518
	.4–.6	0.566±.067	0.901±.116	1.054±.102	1.123±.085	1.135±.084	1.072±.092	1.026±.106	0.890±.404
	.6–1.	–	0.201±.019	0.204±.023	0.439±.050	0.609±.074	0.903±.106	1.003±.168	0.658±.930
	Elastic	0.980±.069	0.965±.092	0.942±.154	0.855±.261	0.686±.397	0.520±.425	0.030±.022	–

Chapter 4

THE TOTAL CROSS SECTIONS

4.1 INTRODUCTION

In section 1.3 it was noted that the total cross sections for neutrino and antineutrino scattering on isoscalar targets rise linearly with the incident neutrino energy, with world averaged values for the slope σ/E of the cross sections given by equation (1.23). In this chapter these slopes will be calculated for the present experiment, firstly averaged over the energy range accessible to the experiment, and secondly as a function of neutrino energy, to test the validity of the assumption that the cross section rises linearly with energy. The cross sections obtained will be compared with previous measurements.

4.2 σ/E AVERAGED OVER ENERGY

The extraction of the slope of the total cross sections for neutrinos and antineutrinos is in principle a simple matter. Given the information on the muon flux in the shielding obtained in the manner described in section 2.2.2, it is possible to predict both the total number of neutrinos passing through the chamber fiducial volume during the experiment and the shape of the distribution in energy and radius measured from the beam axis. From this information, the number of events that would be observed given a value $\sigma/E =$

$1 \times 10^{-38}\text{cm}^2\text{GeV}^{-1}$ for the slope can be predicted. The actual value of σ/E may then be calculated by simply dividing the total number of events observed by this prediction. This calculation will now be considered in more detail.

The variation of the neutrino and antineutrino event spectra with energy is related to the fluxes and cross sections through the equation

$$\frac{dN_{ev}^{\nu,\bar{\nu}}(E)}{dE} = N^T N^{\nu,\bar{\nu}} \phi^{\nu,\bar{\nu}}(E) \sigma^{\nu,\bar{\nu}}(E) \tag{4.1}$$

where

N^T is the number of target nucleons in the experimental fiducial volume.

$N^{\nu,\bar{\nu}}$ is the total number of neutrinos (antineutrinos) passing through the fiducial volume during the course of the experiment.

$\phi^{\nu,\bar{\nu}}(E)$ is the shape of the neutrino (antineutrino) flux with respect to energy, normalized such that $\int \phi^{\nu,\bar{\nu}}(E)dE = 1\text{m}^{-2}$.

Assuming a linear cross section of slope α and integrating (4.1) over an energy range E_{min}, E_{max} we obtain

$$N_{ev}^{\nu,\bar{\nu}} = N^T N^{\nu,\bar{\nu}} < E >^{\nu,\bar{\nu}} \alpha^{\nu,\bar{\nu}} \tag{4.2}$$

where $< E >^{\nu,\bar{\nu}} = \int_{E_{min}}^{E_{max}} E\phi^{\nu,\bar{\nu}}(E)dE$ is the mean neutrino (antineutrino) energy in that energy range. $N^T N^{\nu,\bar{\nu}} < E >^{\nu,\bar{\nu}}$ is simply the number of events that would be observed for a cross section of slope $\sigma/E = 10^{-38}\text{cm}^2/\text{GeV}$.

The neutrino (antineutrino) flux as a function of neutrino energy and radial distance from the beam axis, as measured by the CERN group [42] is given in Tables 4.1a,b for the WA59 experiment, normalized such that each entry gives the number of neutrinos (antineutrinos) in a given bin per unit energy and area, for 10^4 protons incident on the beryllium target. It is necessary to know the variation of the flux with energy averaged over the experimental fiducial volume. The fluxes in Table 4.1 are independent of the fiducial volume, and refer to numbers of neutrinos incident on a plane located at the position of BEBC perpendicular to the beam axis. If Φ_{ij} is the flux per unit energy in the

Table 4.1a : Neutrino Flux ($GeV^{-1}m^{-2}$) per 10^4 protons

		Radius(m)										
		0.0–0.2	0.2–0.4	0.4–0.6	0.6–0.8	0.8–1.0	1.0–1.2	1.2–1.4	1.4–1.6	1.6–1.8	1.8–2.0	2.0–2.2
	5–10	$.966\times10^{-2}$	$.110\times10^{+0}$	$.132\times10^{+0}$	$.259\times10^{+0}$	$.317\times10^{+0}$	$.417\times10^{+0}$	$.450\times10^{+0}$	$.607\times10^{+0}$	$.708\times10^{+0}$	$.840\times10^{+0}$	$.667\times10^{+0}$
	10–15	$.697\times10^{-1}$	$.260\times10^{+0}$	$.333\times10^{+0}$	$.601\times10^{+0}$	$.669\times10^{+0}$	$.680\times10^{+0}$	$.805\times10^{+0}$	$.869\times10^{+0}$	$.879\times10^{+0}$	$.830\times10^{+0}$	$.676\times10^{+0}$
	15–20	$.641\times10^{-1}$	$.171\times10^{+0}$	$.304\times10^{+0}$	$.474\times10^{+0}$	$.502\times10^{+0}$	$.511\times10^{+0}$	$.517\times10^{+0}$	$.442\times10^{+0}$	$.437\times10^{+0}$	$.357\times10^{+0}$	$.321\times10^{+0}$
	20–25	$.632\times10^{-1}$	$.160\times10^{+0}$	$.270\times10^{+0}$	$.387\times10^{+0}$	$.396\times10^{+0}$	$.359\times10^{+0}$	$.291\times10^{+0}$	$.233\times10^{+0}$	$.205\times10^{+0}$	$.190\times10^{+0}$	$.109\times10^{+0}$
	25–30	$.366\times10^{-1}$	$.129\times10^{+0}$	$.228\times10^{+0}$	$.266\times10^{+0}$	$.256\times10^{+0}$	$.202\times10^{+0}$	$.199\times10^{+0}$	$.157\times10^{+0}$	$.119\times10^{+0}$	$.961\times10^{-1}$	$.691\times10^{-1}$
	30–40	$.450\times10^{-1}$	$.130\times10^{+0}$	$.172\times10^{+0}$	$.151\times10^{+0}$	$.113\times10^{+0}$	$.689\times10^{-1}$	$.551\times10^{-1}$	$.420\times10^{-1}$	$.467\times10^{-1}$	$.469\times10^{-1}$	$.374\times10^{-1}$
	40–50	$.352\times10^{-1}$	$.840\times10^{-1}$	$.801\times10^{-1}$	$.546\times10^{-1}$	$.399\times10^{-1}$	$.344\times10^{-1}$	$.358\times10^{-1}$	$.342\times10^{-1}$	$.407\times10^{-1}$	$.500\times10^{-1}$	$.474\times10^{-1}$
	50–60	$.187\times10^{-1}$	$.416\times10^{-1}$	$.372\times10^{-1}$	$.294\times10^{-1}$	$.254\times10^{-1}$	$.273\times10^{-1}$	$.296\times10^{-1}$	$.340\times10^{-1}$	$.433\times10^{-1}$	$.396\times10^{-1}$	$.432\times10^{-1}$
	60–70	$.701\times10^{-2}$	$.146\times10^{-1}$	$.178\times10^{-1}$	$.195\times10^{-1}$	$.200\times10^{-1}$	$.252\times10^{-1}$	$.310\times10^{-1}$	$.320\times10^{-1}$	$.342\times10^{-1}$	$.404\times10^{-1}$	$.411\times10^{-1}$
	70–80	$.301\times10^{-2}$	$.985\times10^{-2}$	$.145\times10^{-1}$	$.180\times10^{-1}$	$.190\times10^{-1}$	$.220\times10^{-1}$	$.276\times10^{-1}$	$.284\times10^{-1}$	$.291\times10^{-1}$	$.286\times10^{-1}$	$.207\times10^{-1}$
E (GeV)	80–90	$.178\times10^{-2}$	$.631\times10^{-2}$	$.989\times10^{-2}$	$.148\times10^{-1}$	$.166\times10^{-1}$	$.197\times10^{-1}$	$.225\times10^{-1}$	$.223\times10^{-1}$	$.168\times10^{-1}$	$.128\times10^{-1}$	$.904\times10^{-2}$
	90–100	$.166\times10^{-2}$	$.501\times10^{-2}$	$.904\times10^{-2}$	$.139\times10^{-1}$	$.149\times10^{-1}$	$.162\times10^{-1}$	$.156\times10^{-1}$	$.124\times10^{-1}$	$.903\times10^{-2}$	$.546\times10^{-2}$	$.392\times10^{-2}$
	100–120	$.137\times10^{-2}$	$.406\times10^{-2}$	$.812\times10^{-2}$	$.896\times10^{-2}$	$.106\times10^{-1}$	$.934\times10^{-2}$	$.712\times10^{-2}$	$.538\times10^{-2}$	$.343\times10^{-2}$	$.254\times10^{-2}$	$.200\times10^{-2}$
	120–140	$.110\times10^{-2}$	$.341\times10^{-2}$	$.530\times10^{-2}$	$.512\times10^{-2}$	$.456\times10^{-2}$	$.342\times10^{-2}$	$.261\times10^{-2}$	$.193\times10^{-2}$	$.151\times10^{-2}$	$.105\times10^{-2}$	$.739\times10^{-3}$
	140–160	$.915\times10^{-3}$	$.201\times10^{-2}$	$.245\times10^{-2}$	$.234\times10^{-2}$	$.217\times10^{-2}$	$.166\times10^{-2}$	$.125\times10^{-2}$	$.953\times10^{-3}$	$.611\times10^{-3}$	$.469\times10^{-3}$	$.360\times10^{-3}$
	160–180	$.409\times10^{-3}$	$.962\times10^{-3}$	$.118\times10^{-2}$	$.117\times10^{-2}$	$.987\times10^{-3}$	$.811\times10^{-3}$	$.606\times10^{-3}$	$.362\times10^{-3}$	$.288\times10^{-3}$	$.188\times10^{-3}$	$.170\times10^{-3}$
	180–200	$.152\times10^{-3}$	$.449\times10^{-3}$	$.611\times10^{-3}$	$.608\times10^{-3}$	$.570\times10^{-3}$	$.407\times10^{-3}$	$.268\times10^{-3}$	$.169\times10^{-3}$	$.116\times10^{-3}$	$.796\times10^{-4}$	$.555\times10^{-4}$
	200–220	$.599\times10^{-4}$	$.199\times10^{-3}$	$.297\times10^{-3}$	$.350\times10^{-3}$	$.289\times10^{-3}$	$.192\times10^{-3}$	$.115\times10^{-3}$	$.734\times10^{-4}$	$.514\times10^{-4}$	$.375\times10^{-4}$	$.228\times10^{-4}$
	220–240	$.225\times10^{-4}$	$.799\times10^{-4}$	$.159\times10^{-3}$	$.166\times10^{-3}$	$.141\times10^{-3}$	$.839\times10^{-4}$	$.480\times10^{-4}$	$.291\times10^{-4}$	$.196\times10^{-4}$	$.111\times10^{-4}$	$.680\times10^{-5}$
	240–260	$.911\times10^{-5}$	$.340\times10^{-4}$	$.733\times10^{-4}$	$.904\times10^{-4}$	$.685\times10^{-4}$	$.420\times10^{-4}$	$.199\times10^{-4}$	$.113\times10^{-4}$	$.700\times10^{-5}$	$.480\times10^{-5}$	$.232\times10^{-5}$
	260–280	$.302\times10^{-5}$	$.128\times10^{-4}$	$.293\times10^{-4}$	$.354\times10^{-4}$	$.264\times10^{-4}$	$.146\times10^{-4}$	$.625\times10^{-5}$	$.271\times10^{-5}$	$.222\times10^{-5}$	$.105\times10^{-5}$	$.657\times10^{-6}$
	280–300	$.498\times10^{-6}$	$.336\times10^{-5}$	$.702\times10^{-5}$	$.936\times10^{-5}$	$.481\times10^{-5}$	$.251\times10^{-5}$	$.118\times10^{-5}$	$.564\times10^{-6}$	$.277\times10^{-6}$	$.152\times10^{-6}$	$.817\times10^{-7}$

Table 4.1b : Antineutrino Flux ($GeV^{-1}m^{-2}$) per 10^4 protons

		Radius(m)										
		0.0–0.2	0.2–0.4	0.4–0.6	0.6–0.8	0.8–1.0	1.0–1.2	1.2–1.4	1.4–1.6	1.6–1.8	1.8–2.0	2.0–2.2
	5–10	$.728\times10^{-2}$	$.822\times10^{-1}$	$.971\times10^{-1}$	$.191\times10^{+0}$	$.232\times10^{+0}$	$.303\times10^{+0}$	$.325\times10^{+0}$	$.442\times10^{+0}$	$.512\times10^{+0}$	$.613\times10^{+0}$	$.491\times10^{+0}$
	10–15	$.516\times10^{-1}$	$.193\times10^{+0}$	$.247\times10^{+0}$	$.443\times10^{+0}$	$.486\times10^{+0}$	$.493\times10^{+0}$	$.584\times10^{+0}$	$.632\times10^{+0}$	$.642\times10^{+0}$	$.609\times10^{+0}$	$.498\times10^{+0}$
	15–20	$.482\times10^{-1}$	$.126\times10^{+0}$	$.222\times10^{+0}$	$.343\times10^{+0}$	$.354\times10^{+0}$	$.360\times10^{+0}$	$.371\times10^{+0}$	$.318\times10^{+0}$	$.319\times10^{+0}$	$.259\times10^{+0}$	$.235\times10^{+0}$
	20–25	$.452\times10^{-1}$	$.112\times10^{+0}$	$.185\times10^{+0}$	$.264\times10^{+0}$	$.269\times10^{+0}$	$.247\times10^{+0}$	$.203\times10^{+0}$	$.165\times10^{+0}$	$.148\times10^{+0}$	$.137\times10^{+0}$	$.787\times10^{-1}$
	25–30	$.234\times10^{-1}$	$.814\times10^{-1}$	$.144\times10^{+0}$	$.166\times10^{+0}$	$.163\times10^{+0}$	$.132\times10^{+0}$	$.133\times10^{+0}$	$.107\times10^{+0}$	$.812\times10^{-1}$	$.628\times10^{-1}$	$.435\times10^{-1}$
	30–40	$.259\times10^{-1}$	$.753\times10^{-1}$	$.988\times10^{-1}$	$.870\times10^{-1}$	$.666\times10^{-1}$	$.414\times10^{-1}$	$.332\times10^{-1}$	$.242\times10^{-1}$	$.260\times10^{-1}$	$.258\times10^{-1}$	$.204\times10^{-1}$
	40–50	$.176\times10^{-1}$	$.425\times10^{-1}$	$.406\times10^{-1}$	$.279\times10^{-1}$	$.206\times10^{-1}$	$.175\times10^{-1}$	$.182\times10^{-1}$	$.171\times10^{-1}$	$.200\times10^{-1}$	$.237\times10^{-1}$	$.217\times10^{-1}$
	50–60	$.872\times10^{-2}$	$.192\times10^{-1}$	$.169\times10^{-1}$	$.133\times10^{-1}$	$.116\times10^{-1}$	$.127\times10^{-1}$	$.135\times10^{-1}$	$.150\times10^{-1}$	$.186\times10^{-1}$	$.157\times10^{-1}$	$.170\times10^{-1}$
	60–70	$.307\times10^{-2}$	$.614\times10^{-2}$	$.728\times10^{-2}$	$.790\times10^{-2}$	$.811\times10^{-2}$	$.100\times10^{-1}$	$.119\times10^{-1}$	$.119\times10^{-1}$	$.120\times10^{-1}$	$.142\times10^{-1}$	$.142\times10^{-1}$
	70–80	$.113\times10^{-2}$	$.371\times10^{-2}$	$.538\times10^{-2}$	$.663\times10^{-2}$	$.677\times10^{-2}$	$.760\times10^{-2}$	$.905\times10^{-2}$	$.874\times10^{-2}$	$.881\times10^{-2}$	$.850\times10^{-2}$	$.592\times10^{-2}$
E (GeV)	80–90	$.592\times10^{-3}$	$.210\times10^{-2}$	$.333\times10^{-2}$	$.476\times10^{-2}$	$.500\times10^{-2}$	$.569\times10^{-2}$	$.607\times10^{-2}$	$.583\times10^{-2}$	$.417\times10^{-2}$	$.311\times10^{-2}$	$.214\times10^{-2}$
	90–100	$.480\times10^{-3}$	$.146\times10^{-2}$	$.257\times10^{-2}$	$.386\times10^{-2}$	$.388\times10^{-2}$	$.394\times10^{-2}$	$.357\times10^{-2}$	$.271\times10^{-2}$	$.190\times10^{-2}$	$.109\times10^{-2}$	$.788\times10^{-3}$
	100–120	$.335\times10^{-3}$	$.989\times10^{-3}$	$.192\times10^{-2}$	$.195\times10^{-2}$	$.221\times10^{-2}$	$.183\times10^{-2}$	$.132\times10^{-2}$	$.963\times10^{-3}$	$.597\times10^{-3}$	$.453\times10^{-3}$	$.370\times10^{-3}$
	120–140	$.208\times10^{-3}$	$.631\times10^{-3}$	$.928\times10^{-3}$	$.851\times10^{-3}$	$.712\times10^{-3}$	$.503\times10^{-3}$	$.370\times10^{-3}$	$.275\times10^{-3}$	$.223\times10^{-3}$	$.170\times10^{-3}$	$.117\times10^{-3}$
	140–160	$.129\times10^{-3}$	$.273\times10^{-3}$	$.320\times10^{-3}$	$.293\times10^{-3}$	$.265\times10^{-3}$	$.196\times10^{-3}$	$.145\times10^{-3}$	$.112\times10^{-3}$	$.757\times10^{-4}$	$.618\times10^{-4}$	$.509\times10^{-4}$
	160–180	$.409\times10^{-4}$	$.100\times10^{-3}$	$.120\times10^{-3}$	$.117\times10^{-3}$	$.909\times10^{-4}$	$.722\times10^{-4}$	$.551\times10^{-4}$	$.344\times10^{-4}$	$.324\times10^{-4}$	$.213\times10^{-4}$	$.216\times10^{-4}$
	180–200	$.946\times10^{-5}$	$.316\times10^{-4}$	$.453\times10^{-4}$	$.435\times10^{-4}$	$.388\times10^{-4}$	$.255\times10^{-4}$	$.175\times10^{-4}$	$.131\times10^{-4}$	$.103\times10^{-4}$	$.753\times10^{-5}$	$.561\times10^{-5}$
	200–220	$.213\times10^{-5}$	$.839\times10^{-5}$	$.137\times10^{-4}$	$.167\times10^{-4}$	$.129\times10^{-4}$	$.807\times10^{-5}$	$.520\times10^{-5}$	$.392\times10^{-5}$	$.324\times10^{-5}$	$.235\times10^{-5}$	$.166\times10^{-5}$
	220–240	$.375\times10^{-6}$	$.166\times10^{-5}$	$.432\times10^{-5}$	$.463\times10^{-5}$	$.381\times10^{-5}$	$.207\times10^{-5}$	$.135\times10^{-5}$	$.965\times10^{-6}$	$.700\times10^{-6}$	$.480\times10^{-6}$	$.230\times10^{-6}$
	240–260	$.759\times10^{-7}$	$.321\times10^{-6}$	$.905\times10^{-6}$	$.125\times10^{-5}$	$.971\times10^{-6}$	$.630\times10^{-6}$	$.324\times10^{-6}$	$.185\times10^{-6}$	$.136\times10^{-6}$	$.102\times10^{-6}$	$.535\times10^{-7}$
	260–280	$.882\times10^{-8}$	$.473\times10^{-7}$	$.139\times10^{-6}$	$.206\times10^{-6}$	$.183\times10^{-6}$	$.117\times10^{-6}$	$.480\times10^{-7}$	$.265\times10^{-7}$	$.247\times10^{-7}$	$.133\times10^{-7}$	$.850\times10^{-8}$
	280–300	$.410\times10^{-9}$	$.359\times10^{-8}$	$.924\times10^{-8}$	$.173\times10^{-7}$	$.117\times10^{-7}$	$.856\times10^{-8}$	$.421\times10^{-8}$	$.271\times10^{-8}$	$.136\times10^{-8}$	$.840\times10^{-9}$	$.540\times10^{-9}$

ith bin of radius and jth bin of energy, then the flux per unit energy for the jth energy bin averaged over the fiducial volume is given by

$$\Phi_j = \sum_i \Phi_{ij} \Delta V_i \tag{4.3}$$

where ΔV_i is the volume of intersection of the fiducial volume and an annular cylinder whose axis is the beam axis, extending over the ith radius bin. The average flux per unit energy calculated using (4.3) is given in Table 4.2, normalized such that $\sum_j \Phi_j \Delta E_j = 1m^{-2}$, where the first energy bin begins at 10 GeV and ΔE_j is the width of the jth energy bin. Thus defined, these flux shapes Φ_j correspond to the $\phi^{\nu,\bar{\nu}}(E)$ of equation (4.1).

The total number of neutrinos (antineutrinos) is obtained by summing the numbers of muons observed in the shielding by the NFM during the course of the experiment. The relationship of the number of muons observed to the number of neutrinos passing through the chamber is obtained from the fit to the shape of the muon fluxes outlined in Section 2.2.2. Following the selection of the event sample detailed below it was found that $N^{\nu} = 5.12 \times 10^9$, $N^{\bar{\nu}} = 1.92 \times 10^{10}$. The total number of target nucleons within the fiducial volume is $N^T = 4.756 \times 10^{30}$.

Calculation of the slope of the cross section from equation (4.2) requires the total number of events $N_{ev}^{\nu,\bar{\nu}}$ induced by the $N^{\nu,\bar{\nu}}$ neutrinos (antineutrinos). The CC event sample considered was that obtained with the selection criteria of section 3.2. The raw numbers of observed events were corrected for the effects of 1) Geometric and electronic EMI inefficiency, 2) neutral current background, 3) scanning losses, 4) the muon momentum cut, 5) migration of events across the boundary $E = 10$ GeV, and 6) non-isoscalarity of the target. The first three corrections were dealt with in Chapter 3. The fraction of events with $p_\mu < 5$ GeV/c was estimated by assuming the form (1.15) for the differential cross section and a parametrization for the quark momentum distributions of the form discussed in Section (3.7.2). The correction factor for migration of events across the boundary $E = 10$ GeV was estimated using the Monte Carlo. In determining the neutrino energy the Myatt method was used as described in Section 3.6.1. The effect of the non-isoscalarity of the

Table 4.2 : Average Flux per unit Energy

Energy Range (GeV)	Flux $(m^{-2}GeV^{-1})$	
	ν	$\overline{\nu}$
10 – 15	$.502 \times 10^{-1}$	$.583 \times 10^{-1}$
15 – 20	$.377 \times 10^{-1}$	$.430 \times 10^{-1}$
20 – 25	$.296 \times 10^{-1}$	$.323 \times 10^{-1}$
25 – 30	$.204 \times 10^{-1}$	$.207 \times 10^{-1}$
30 – 40	$.123 \times 10^{-1}$	$.113 \times 10^{-1}$
40 – 50	$.607 \times 10^{-2}$	$.489 \times 10^{-2}$
50 – 60	$.338 \times 10^{-2}$	$.246 \times 10^{-2}$
60 – 70	$.202 \times 10^{-2}$	$.130 \times 10^{-2}$
70 – 80	$.168 \times 10^{-2}$	$.948 \times 10^{-3}$
80 – 90	$.133 \times 10^{-2}$	$.643 \times 10^{-3}$
90 – 100	$.112 \times 10^{-2}$	$.470 \times 10^{-3}$
100 – 120	$.763 \times 10^{-3}$	$.262 \times 10^{-3}$
120 – 140	$.412 \times 10^{-3}$	$.109 \times 10^{-3}$
140 – 160	$.208 \times 10^{-3}$	$.422 \times 10^{-4}$
160 – 180	$.993 \times 10^{-4}$	$.155 \times 10^{-4}$
180 – 200	$.498 \times 10^{-4}$	$.550 \times 10^{-5}$
200 – 220	$.246 \times 10^{-4}$	$.174 \times 10^{-5}$
220 – 240	$.115 \times 10^{-4}$	$.473 \times 10^{-6}$
240 – 260	$.555 \times 10^{-5}$	$.115 \times 10^{-6}$
260 – 280	$.212 \times 10^{-5}$	$.192 \times 10^{-7}$
280 – 300	$.484 \times 10^{-6}$	$.140 \times 10^{-8}$

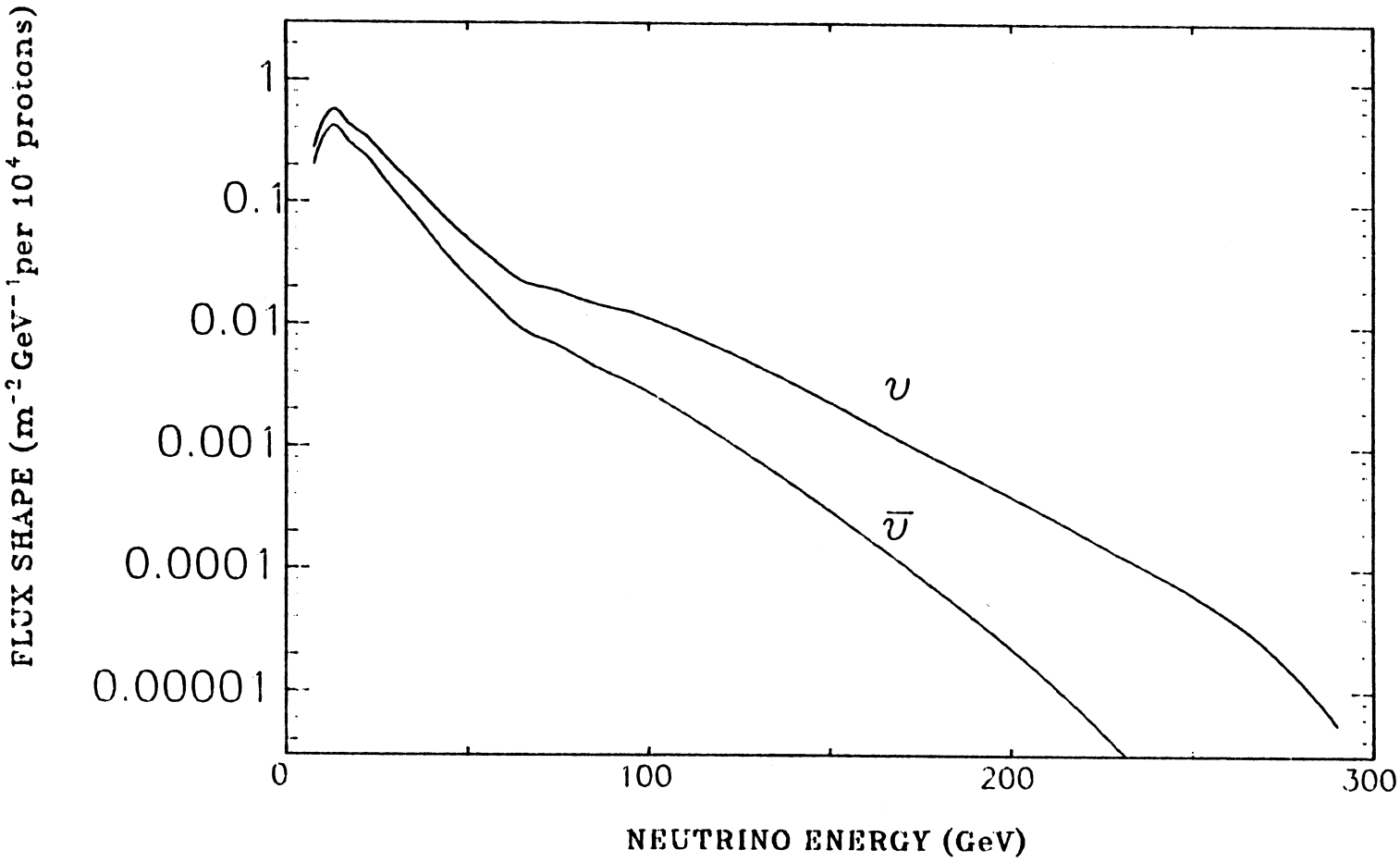

FIG 4.1 NEUTRINO AND ANTINEUTRINO FLUX SHAPES

Table 4.3 : Total Cross Section Calculation

Correction	ν	$\bar{\nu}$
Dead Wires in EMI	1.021	1.026
Neutral Current Background	0.997	0.998
Average Scanning Efficiency	1.054	1.038
Average EMI Geometric Acceptance	1.018	1.007
EMI Electronic Inefficiency	1.030	1.030
Muon Momentum Cut	1.183	1.098
Migration across E = 10 GeV Cut	1.010	1.008
Non-isoscalarity of Target	1.0078	0.9924
Raw Number of Events	5915	9529
Corrected Number of Events	8020.5 ± 105.1	11535.2 ± 116.4
Number of Events for $\sigma/E = 1 \times 10^{-38}\text{cm}^2/\text{GeV}$	13177.9	37603.0
σ/E ($\times 10^{-38}\text{cm}^2/\text{GeV}$)	.609 ± .008	.307 ± .003

target was calculated assuming the values of $\sigma^{\nu p}/\sigma^{\nu n} = 0.5$ and $\sigma^{\bar{\nu}p}/\sigma^{\bar{\nu}n} = 2.0$, and the known fractions of protons and neutrons in the target.

The magnitudes of the above corrections for both the neutrino and antineutrino samples are summarised in Table 4.3 along with the uncorrected and corrected event numbers. Using the corrected numbers in equation 4.2 gives the following values for the slopes of the cross sections with energy

$$\sigma^{\nu N}/E = (.609 \pm .008) \times 10^{-38} cm^2/GeV$$

$$\sigma^{\bar{\nu}N}/E = (.307 \pm .003) \times 10^{-38} cm^2/GeV$$

The errors quoted are statistical only.

The major source of systematic error in the cross section measurements is due to uncertainty in the normalization of the neutrino and antineutrino fluxes. Contributions to this error come from the calibration of the muon detectors in the gaps in the shielding and from assumptions in the Monte Carlo program used to fit the observed muon fluxes. The normalization error has been estimated for this experiment to be 7% [42].

In correcting for the muon momentum cut of 5 GeV/c, a value for the ratio of structure function integrals $B = \int_0^1 xF_3 dx / \int_0^1 F_2 dx$ must be assumed. The form of distributions used corresponded to a value of $B = .66$. Choosing a value of $B = .77$ induced an increase of .25% in σ^{ν}/E and a decrease of 2.1% in $\sigma^{\bar{\nu}}/E$.

The correction factor due to migration of events across the $E = 10$ GeV boundary is dependent on the details of the Monte Carlo used in its calculation and on the method of energy estimation used. The cross sections were recalculated using both no correction and a constant correction (see section 3.6.1) and found to be (statistical errors only)

$$\sigma^{\nu}/E = (.612 \pm .008) \times 10^{-38} cm^2/GeV$$

$$\sigma^{\bar{\nu}}/E = (.307 \pm .003) \times 10^{-38} cm^2/GeV$$

for no correction and

$$\sigma^{\nu}/E = (.611 \pm .008) \times 10^{-38} cm^2/GeV$$

$$\sigma^{\bar{\nu}}/E = (.307 \pm .003) \times 10^{-38} cm^2/GeV$$

for a constant correction. It can be seen that the cross section measurement is not sensitive to the method of energy correction chosen.

The sensitivity of the cross section measurements to the low neutrino energy region, for which the determination of the muon flux is less reliable, was investigated by repeating the above calculation with the neutrino energy cut raised to 20 GeV. In this case the cross sections were found to be

$$\sigma^{\nu}/E = (.621 \pm .009) \times 10^{-38} cm^2/GeV$$

$$\sigma^{\bar{\nu}}/E = (.319 \pm .004) \times 10^{-38} cm^2/GeV$$

an increase of 2.0% for σ^{ν}/E and 3.9% for $\sigma^{\bar{\nu}}/E$.

A final check on the systematic uncertainty in the above measurements is the sensitivity to the assumptions made in the fitting of the muon fluxes, used to obtain the neutrino fluxes of Table 4.1. The fluxes quoted in this table were obtained assuming a focussing efficiency of 80% and density of iron shielding of 7.2 g cm^{-3}. By focussing efficiency is meant the fraction of the nominal horn and reflector currents used in the Monte Carlo fit to the muon fluxes. Neutrino fluxes were also available [42] for a focussing efficiency of

95% and shielding density of 7.3 g cm^{-3}. The cross section calculation was repeated using these fluxes, the results being

$$\sigma^{\nu}/E = (.592 \pm .008) \times 10^{-38} cm^2/GeV$$

$$\sigma^{\overline{\nu}}/E = (.299 \pm .003) \times 10^{-38} cm^2/GeV$$

for focussing efficiency 80%, shielding density 7.3 g cm^{-3},

$$\sigma^{\nu}/E = (.619 \pm .008) \times 10^{-38} cm^2/GeV$$

$$\sigma^{\overline{\nu}}/E = (.323 \pm .003) \times 10^{-38} cm^2/GeV$$

for focussing efficiency 95%, shielding density 7.2 g cm^{-3}, and

$$\sigma^{\nu}/E = (.606 \pm .008) \times 10^{-38} cm^2/GeV$$

$$\sigma^{\overline{\nu}}/E = (.315 \pm .003) \times 10^{-38} cm^2/GeV$$

for focussing efficiency 95%, shielding density 7.3 g cm^{-3}. Considering the spread in these values, systematic errors of 2.2% (ν) and 3.9% ($\overline{\nu}$) were assigned to the measured cross section values as being representative of the errors due to these assumptions.

The above discussion is designed to give a feel for the systematic uncertainty in the total cross section measurement. There are further uncertainties due to other assumptions made in the Monte Carlo used to fit the muon fluxes, for example the assumed value for the ratio of parent pions to kaons produced in the Be target. These have not been taken into account here, but nevertheless contribute to the total systematic error. The dominant contributions are believed however to be the normalization error of 7% quoted above, and the errors due to focussing efficiency and density assumptions. With these two errors alone, added in quadrature, the calculated values of the total neutrino and antineutrino cross sections above $E =$ 10 GeV become

$$\sigma^{\nu}/E = (.609 \pm .008(stat.) \pm .044(syst.)) \times 10^{-38} cm^2/GeV$$

$$\sigma^{\overline{\nu}}/E = (.307 \pm .003(stat.) \pm .025(syst.)) \times 10^{-38} cm^2/GeV$$

It can be seen that the systematic uncertainty in the values obtained dominates over the statistical error derived from event numbers alone.

Using the above measured values of the cross sections, a value for the cross section ratio $R^{\overline{\nu}/\nu} = \sigma^{\overline{\nu}}/\sigma^{\nu}$ was calculated. This ratio is a quantity which is better determined

than the individual cross sections, as much of the contribution to the the normalization error cancels in the ratio. The normalization error in the ratio was estimated to be 1.4% [42]. Taking this as representing the dominant systematic error, the cross section ratio obtained was

$$R^{\bar{\nu}/\nu} = .504 \pm .008(stat.) \pm .007(syst.)$$

In this case, in contrast to the individual total cross sections, the statistical and systematic errors are of similar magnitude.

Finally, on the assumption of scaling, it is possible using the values obtained for the cross sections to deduce a value for the ratio B of structure function integrals introduced above. Clearly this is not a "measurement" of the quantity B as a value for it has been assumed in calculating $\sigma^{\nu,\bar{\nu}}/E$. Nevertheless, it is important to demonstrate consistency between the value assumed in correcting for the muon momentum cut and the value implied by the cross sections thus obtained. If F_2 and xF_3 are taken to be functions of x only, and the W propagator term ignored, equation (1.15) may be integrated over x and y to yield

$$\sigma^{\nu,\bar{\nu}} = \frac{G^2 mE}{\pi}\left\{\frac{4}{3}\int_0^1 F_2(x)dx \pm \frac{2}{3}\int_0^1 xF_3(x)dx\right\} \tag{4.4}$$

which may be solved to give

$$\begin{aligned}\int_0^1 F_2(x)dx &= \frac{3}{4}\frac{\pi}{G^2 m}\left(\frac{\sigma^{\nu}}{E} + \frac{\sigma^{\bar{\nu}}}{E}\right)\\ \int_0^1 xF_3(x)dx &= \frac{3}{2}\frac{\pi}{G^2 m}\left(\frac{\sigma^{\nu}}{E} - \frac{\sigma^{\bar{\nu}}}{E}\right)\end{aligned} \tag{4.5}$$

Using the values of σ^{ν}/E and $\sigma^{\bar{\nu}}/E$ obtained above, and $G^2 m/\pi = 1.582 \times 10^{-38}$ cm^2 GeV^{-1}, it follows that

$$\int_0^1 F_2(x)dx = .434 \pm .004(stat.)$$
$$\int_0^1 xF_3(x)dx = .286 \pm .008(stat.)$$

and

$$B = \int_0^1 xF_3(x)dx \Big/ \int_0^1 F_2(x)dx = .660 \pm .019(stat.)$$

consistent with the value assumed in the correction for the muon momentum cut. It should be noted that using the extraction of the structure functions F_2 and xF_3 in the following chapter, a value of B will be deduced in Chapter 6 and compared with this value.

4.3 σ/E AS A FUNCTION OF ENERGY

Calculation of the slopes of the cross sections $\sigma^{\nu,\bar{\nu}}/E$ as a function of energy is in principle identical, in each chosen bin of energy, to the calculation of $\sigma^{\nu,\bar{\nu}}/E$ above $E = 10$ GeV performed in the preceding section. The correction for migration of events across the cut boundary now appears as an unsmearing factor for a given bin, but is calculated in the same manner as previously using the Monte Carlo.

The bins of energy chosen were the following

10-15 GeV, 15-20 GeV, 20-30 GeV, 30-50 GeV, 50-80 GeV, 80-120 GeV, 120-180 GeV, 180-300 GeV

The final bin was limited by statistics as will be seen below. There is practically no data from the present experiment above a neutrino energy of 300 GeV.

Tables 4.4a,b summarise the calculation of the total cross section slopes for the neutrino and antineutrino samples respectively. In each table, the first column (a) gives the raw event numbers in each bin. The Myatt energy correction was applied, as described in section 3.6.1. The following columns give the correction factors for EMI dead wires, NC background, geometric EMI acceptance, scan losses, muon momentum cut and energy resolution. These corrections were applied to the raw event numbers in addition to the global 3% electronic inefficiency and non-isoscalarity corrections, giving the event numbers in column (b). The corrections for scan losses and geometric acceptance are in fact event by event weights, and the tables quote the average values of these weights. Similarly the dead wire and neutral current background corrections quoted are the effective weights resulting from the numbers of events found on the correction tapes (see section 3.3). The numbers of events expected for a slope of $\sigma/E = 1 \times 10^{-38}$ cm^2/GeV is given in column (c), and the value of the total cross section slope in the final column. The quoted errors are statistical only.

The above values of the total cross section as a function of energy are displayed graphically in Figure 4.2. Also shown in this figure are the values obtained using both

Table 4.4a : Total Neutrino Cross Section as a Function of Energy

	(a)							(b)	(c)	
Energy Bin (GeV)	Raw Event Numbers	Dead Wires	NC Background	Geometric Acceptance	Scanning Inefficiency	p_μ Cut	Energy Resolution	Corr. Event Numbers	Number Events $\sigma/E = 10^{-38} cm^2/GeV$	σ/E $\times 10^{-38} cm^2/GeV$
10–15	333	1.027	0.993	1.036	1.093	1.597	0.993	632.7 ± 35.8	1364.3	.464 ± .026
15–20	530	1.026	0.995	1.030	1.084	1.365	1.038	888.3 ± 39.5	1434.4	.619 ± .028
20–30	1084	1.027	0.998	1.026	1.064	1.236	1.051	1635.3 ± 50.0	2667.6	.613 ± .019
30–50	1489	1.015	0.997	1.018	1.059	1.141	1.028	1977.1 ± 52.0	3052.8	.648 ± .017
50–80	1001	1.019	0.997	1.013	1.037	1.082	0.968	1161.4 ± 36.5	1924.4	.604 ± .019
80–120	773	1.022	0.997	1.009	1.040	1.051	1.042	939.3 ± 33.9	1682.8	.558 ± .020
120–180	526	1.019	0.999	1.008	1.034	1.035	0.983	589.5 ± 25.7	883.3	.667 ± .029
180–300	179	1.025	0.998	1.003	1.029	1.024	0.675	135.6 ± 9.9	168.4	.805 ± .059
> 10	5915	1.021	0.997	1.018	1.055	1.183	1.010	8020.5 ± 105.1	13177.9	.609 ± .008
> 20	5052	1.020	0.998	1.016	1.049	1.124	1.009	6449.3 ± 91.2	10379.2	.621 ± .009

Table 4.4b : Total Antineutrino Cross Section as a Function of Energy

	(a)						(b)	(c)	
Energy Bin (GeV)	Raw Event Numbers	Dead Wires	NC Background	Geometric Acceptance	Scanning Inefficiency	p_μ Cut	Energy Resolution	Corr. Event Numbers	Number Events $\sigma/E = 10^{-38} cm^2/GeV$	σ/E $\times 10^{-38} cm^2/GeV$
10-15	937	1.028	0.997	1.017	1.052	1.246	1.018	1332.1 ± 42.9	5483.3	.243 ± .008
15-20	1265	1.025	0.998	1.012	1.050	1.147	1.055	1701.5 ± 47.1	5658.0	.301 ± .008
20-30	2315	1.030	0.997	1.009	1.042	1.096	1.055	2957.2 ± 60.4	9732.6	.304 ± .006
30-50	2530	1.022	0.998	1.005	1.033	1.059	1.012	3042.1 ± 59.6	9256.9	.329 ± .006
50-80	1371	1.028	0.997	1.003	1.029	1.035	0.951	1459.0 ± 38.8	4368.5	.334 ± .009
80-120	765	1.025	0.999	1.001	1.025	1.022	0.961	807.6 ± 28.7	2360.4	.342 ± .012
120-180	269	1.015	0.994	1.003	1.021	1.015	0.833	240.5 ± 14.6	696.4	.345 ± .021
180-300	77	1.013	0.981	1.005	1.023	1.011	0.282	22.9 ± 2.7	46.8	.489 ± .058
> 10	9529	1.026	0.998	1.007	1.038	1.098	1.008	11535.2 ± 116.4	37603.0	.307 ± .003
> 20	7327	1.026	0.997	1.005	1.034	1.063	0.998	8450.9 ± 97.3	26461.6	.319 ± .004

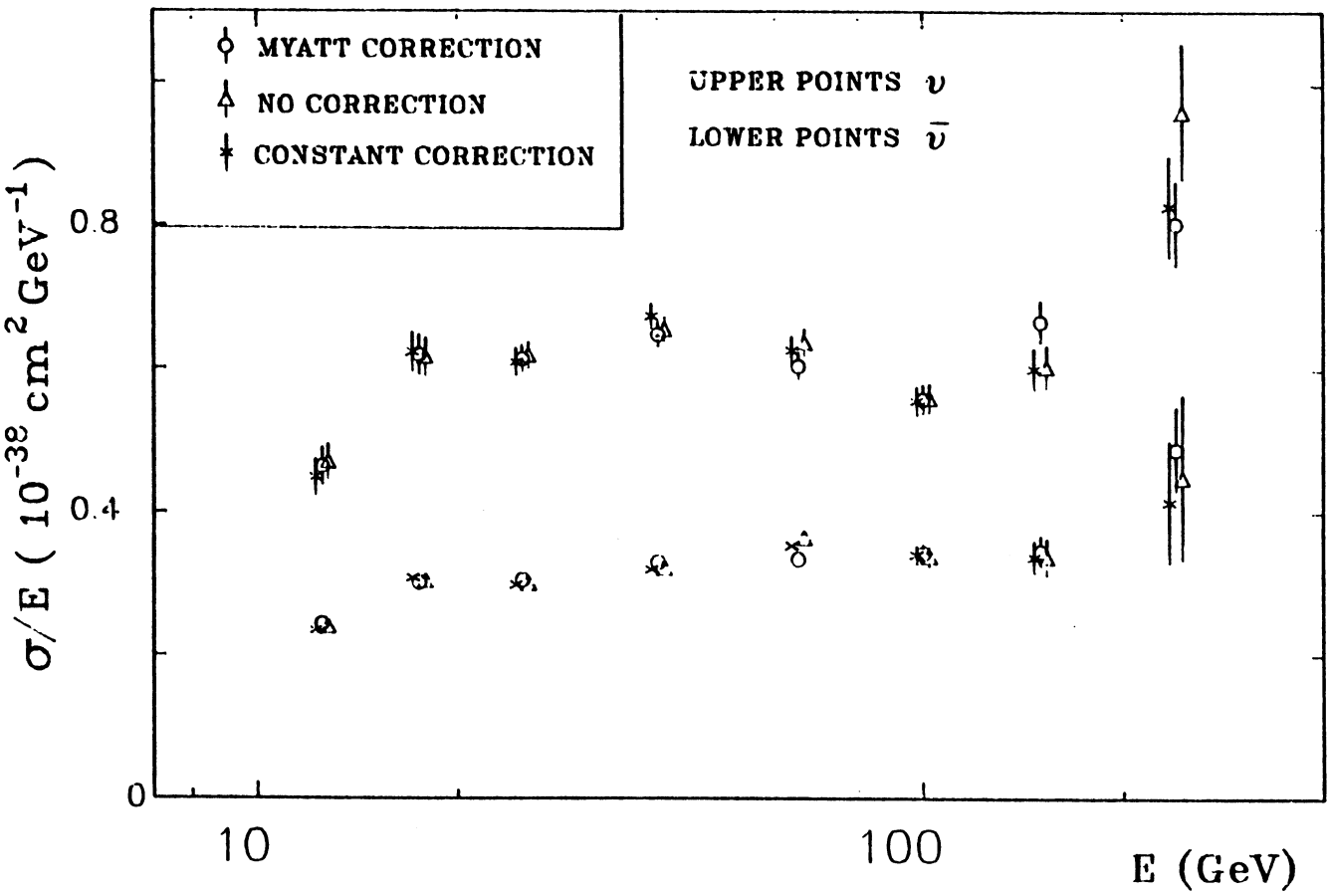

FIG 4.2 TOTAL CROSS SECTIONS AS A FUNCTION OF NEUTRINO ENERGY FOR 3 ENERGY CORRECTION METHODS

Table 4.5a : Total ν Cross Section as a Function of Energy For 3 Energy Correction Methods

Neutrino Energy (GeV)	σ^{ν}/E ($\times 10^{-38}$cm^{2}GeV^{-1})		
	Myatt Correction	No Correction	Constant Correction
10–15	.464 ± .026	.470 ± .024	.449 ± .025
15–20	.619 ± .028	.616 ± .026	.623 ± .027
20–30	.613 ± .019	.618 ± .018	.609 ± .019
30–50	.648 ± .017	.655 ± .017	.674 ± .017
50–80	.604 ± .019	.637 ± .019	.626 ± .019
80–120	.558 ± .020	.559 ± .020	.556 ± .020
120–180	.667 ± .029	.603 ± .030	.601 ± .028
180–300	.805 ± .059	.962 ± .094	.829 ± .070
> 10	.609 ± .008	.612 ± .008	.611 ± .008
> 20	.621 ± .009	.626 ± .009	.625 ± .009

Errors are statistical only

Table 4.5b : Total $\overline{\nu}$ Cross Section as a Function of Energy For 3 Energy Correction Methods

Neutrino Energy (GeV)	$\sigma^{\overline{\nu}}/E$ ($\times 10^{-38}$cm^{2}GeV^{-1})		
	Myatt Correction	No Correction	Constant Correction
10–15	.243 ± .008	.239 ± .007	.234 ± .008
15–20	.301 ± .008	.303 ± .008	.307 ± .008
20–30	.304 ± .006	.299 ± .006	.297 ± .006
30–50	.329 ± .006	.321 ± .006	.319 ± .006
50–80	.334 ± .009	.364 ± .010	.353 ± .007
80–120	.342 ± .012	.338 ± .013	.340 ± .012
120–180	.345 ± .021	.337 ± .025	.337 ± .022
180–300	.489 ± .058	.449 ± .115	.415 ± .085
> 10	.307 ± .003	.307 ± .003	.307 ± .003
> 20	.319 ± .004	.322 ± .004	.320 ± .004

Errors are statistical only

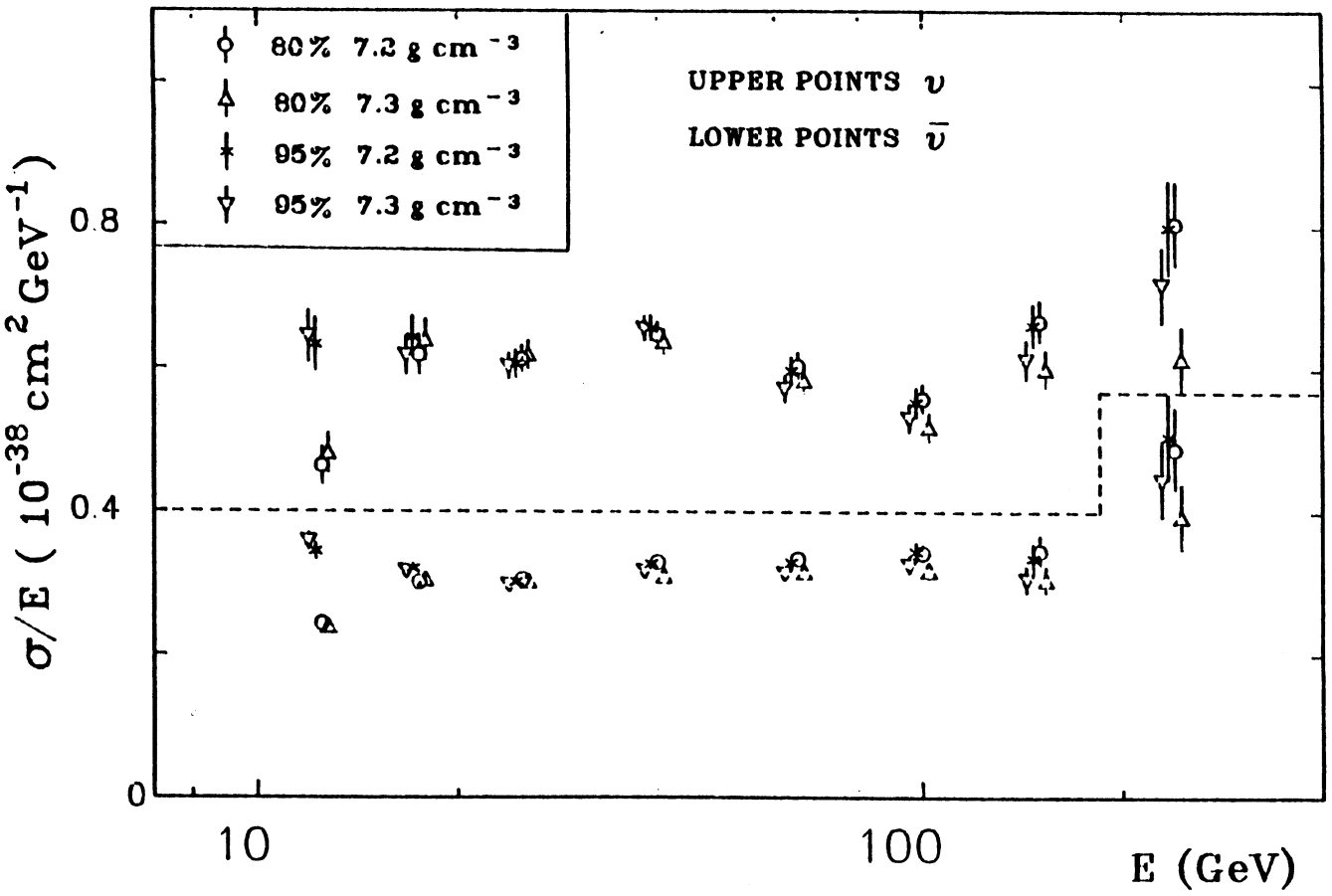

FIG 4.3 TOTAL CROSS SECTIONS AS A FUNCTION OF NEUTRINO ENERGY FOR DIFFERENT FOCUSSING AND DENSITY ASSUMPTIONS

Table 4.6a : Total ν Cross Section as a Function of Energy For Different Focussing and Density Assumptions

Neutrino Energy (GeV)	σ^{ν}/E ($\times 10^{-38}$cm^{2}GeV^{-1})			
	80% 7.2 g cm^{-3}	80% 7.3 g cm^{-3}	95% 7.2 g cm^{-3}	95% 7.3 g cm^{-3}
10–15	.464 ± .026	.482 ± .027	.633 ± .036	.644 ± .036
15–20	.619 ± .028	.640 ± .028	.643 ± .029	.618 ± .027
20–30	.613 ± .019	.619 ± .019	.606 ± .019	.603 ± .018
30–50	.648 ± .017	.638 ± .017	.657 ± .017	.656 ± .017
50–80	.604 ± .019	.584 ± .018	.597 ± .019	.572 ± .018
80–120	.558 ± .020	.519 ± .019	.553 ± .020	.531 ± .019
120–180	.667 ± .029	.601 ± .026	.662 ± .029	.613 ± .027
180–300	.805 ± .059	.615 ± .045	.899 ± .066	.719 ± .053
> 10	.609 ± .008	.592 ± .008	.619 ± .008	.606 ± .008
> 20	.621 ± .009	.598 ± .008	.621 ± .010	.602 ± .009

Errors are statistical only

Table 4.6b : Total $\bar{\nu}$ Cross Section as a Function of Energy For Different Focussing and Density Assumptions

Neutrino Energy (GeV)	$\sigma^{\bar{\nu}}/E$ ($\times 10^{-38}$cm^{2}GeV^{-1})			
	80% 7.2 g cm^{-3}	80% 7.3 g cm^{-3}	95% 7.2 g cm^{-3}	95% 7.3 g cm^{-3}
10–15	.243 ± .008	.239 ± .008	.344 ± .011	.358 ± .012
15–20	.301 ± .008	.305 ± .008	.320 ± .009	.316 ± .009
20–30	.304 ± .006	.302 ± .006	.301 ± .006	.297 ± .006
30–50	.329 ± .006	.310 ± .006	.327 ± .006	.316 ± .006
50–80	.334 ± .009	.316 ± .008	.329 ± .009	.313 ± .008
80–120	.342 ± .012	.318 ± .011	.344 ± .012	.325 ± .012
120–180	.345 ± .021	.305 ± .018	.335 ± .020	.305 ± .018
180–300	.489 ± .058	.394 ± .045	.506 ± .059	.445 ± .052
> 10	.307 ± .003	.299 ± .003	.323 ± .003	.315 ± .003
> 20	.319 ± .004	.309 ± .004	.323 ± .004	.310 ± .004

Errors are statistical only

no energy correction and a constant correction, in order to give an indication of the uncertainty due to the neutrino energy estimation. The values obtained using these three correction methods are given in Tables 4.5a,b.

The uncertainty in the total cross section as a function of energy due to the assumed values for the focussing efficiency and the iron shielding density was investigated in an identical manner to that employed for the total cross section averaged over energy, by repeating the calculation with the other combinations of focussing efficiency of 80% and 95% and shielding density of 7.2 g cm^{-3} and 7.3 g cm^{-3}. Tables 4.6a,b present the values obtained. These values are also displayed in Fig. 4.3. All values shown were obtained using the Myatt method of energy correction.

The total cross sections as a function of neutrino energy calculated under various assumptions and methods of energy correction have been presented above in some detail. The object of the exercise, as stated in the introduction to this chapter, was to check the validity of the assumption that the cross section rises linearly with neutrino energy. On the basis of Figs. 4.2 and 4.3 this assumption would appear to be consistent with the present data. No strong dependence on the method of energy correction employed is observed. From Fig. 4.3 it would appear that the assumptions made for the value of the focussing efficiency and shielding density are a significant source of systematic uncertainty. In particular the values obtained for the total cross sections for the lowest energy bin (10 - 15 GeV) appear very sensitive to the focussing efficiency chosen, and a systematic error appropriate to this variation would have to be assigned. The highest energy bin (180 - 300 GeV), for which statistics are small, also appears sensitive to these assumptions. Therefore, although the cross sections of Table 4.4b for example are suggestive of a slow rise in the value of the cross section slope with energy, when all uncertainties are taken into account, the data shows no evidence for a variation of the cross section slopes with neutrino energy. The total cross sections for neutrino and antineutrino scattering are therefore consistent with a linear rise with neutrino energy.

Table 4.7 gives the values of the cross section ratio $R^{\bar{\nu}/\nu} = \sigma^{\bar{\nu}}/\sigma^{\nu}$ as a function of neutrino energy, for three methods of energy correction. This ratio is also displayed in

Table 4.7 : Cross Section Ratio $R^{\bar{\nu}/\nu}$ as a function of Neutrino Energy For 3 Energy Correction Methods

Neutrino Energy (GeV)	$R^{\bar{\nu}/\nu} = \sigma^{\bar{\nu}}/\sigma^{\nu}$		
	Myatt Correction	No Correction	Constant Correction
10–15	.524 ± .034	.509 ± .030	.521 ± .034
15–20	.486 ± .025	.492 ± .024	.493 ± .025
20–30	.496 ± .018	.484 ± .017	.488 ± .018
30–50	.508 ± .016	.490 ± .016	.473 ± .015
50–80	.553 ± .023	.571 ± .023	.564 ± .020
80–120	.613 ± .031	.605 ± .032	.612 ± .031
120–180	.517 ± .039	.559 ± .050	.561 ± .045
180–300	.607 ± .085	.467 ± .128	.501 ± .111
> 10	.504 ± .008	.502 ± .008	.502 ± .008
> 20	.514 ± .010	.514 ± .010	.512 ± .010

Errors are statistical only

Table 4.8 : Cross Section Ratio $R^{\bar{\nu}/\nu}$ as a function of Neutrino Energy For Different Focussing and Density Assumptions

Neutrino Energy (GeV)	$R^{\bar{\nu}/\nu} = \sigma^{\bar{\nu}}/\sigma^{\nu}$			
	80% 7.2 g cm^{-3}	80% 7.3 g cm^{-3}	95% 7.2 g cm^{-3}	95% 7.3 g cm^{-3}
10–15	.524 ± .034	.496 ± .032	.543 ± .035	.556 ± .036
15–20	.486 ± .025	.477 ± .024	.498 ± .026	.511 ± .027
20–30	.496 ± .018	.488 ± .018	.497 ± .018	.493 ± .018
30–50	.508 ± .016	.486 ± .016	.498 ± .016	.482 ± .015
50–80	.553 ± .023	.541 ± .022	.551 ± .023	.547 ± .022
80–120	.613 ± .031	.613 ± .031	.622 ± .031	.612 ± .031
120–180	.517 ± .039	.507 ± .037	.506 ± .037	.498 ± .037
180–300	.607 ± .085	.641 ± .087	.563 ± .078	.619 ± .086
> 10	.504 ± .008	.505 ± .008	.522 ± .008	.520 ± .008
> 20	.514 ± .010	.517 ± .010	.520 ± .011	.515 ± .010

Errors are statistical only

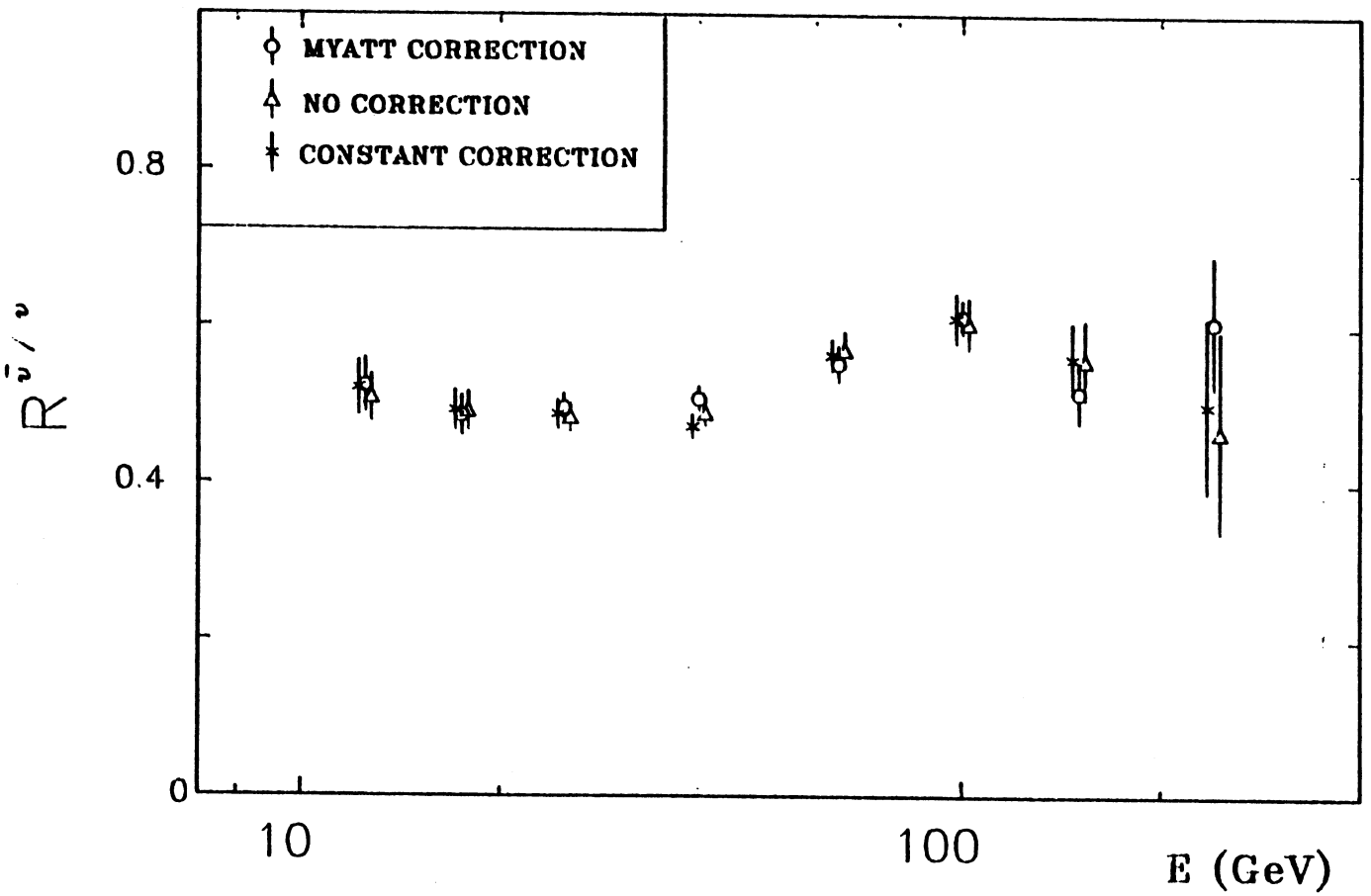

FIG 4.4 RATIO OF TOTAL NEUTRINO AND ANTINEUTRINO CROSS SECTIONS AS A FUNCTION OF NEUTRINO ENERGY FOR 3 ENERGY CORRECTION METHODS

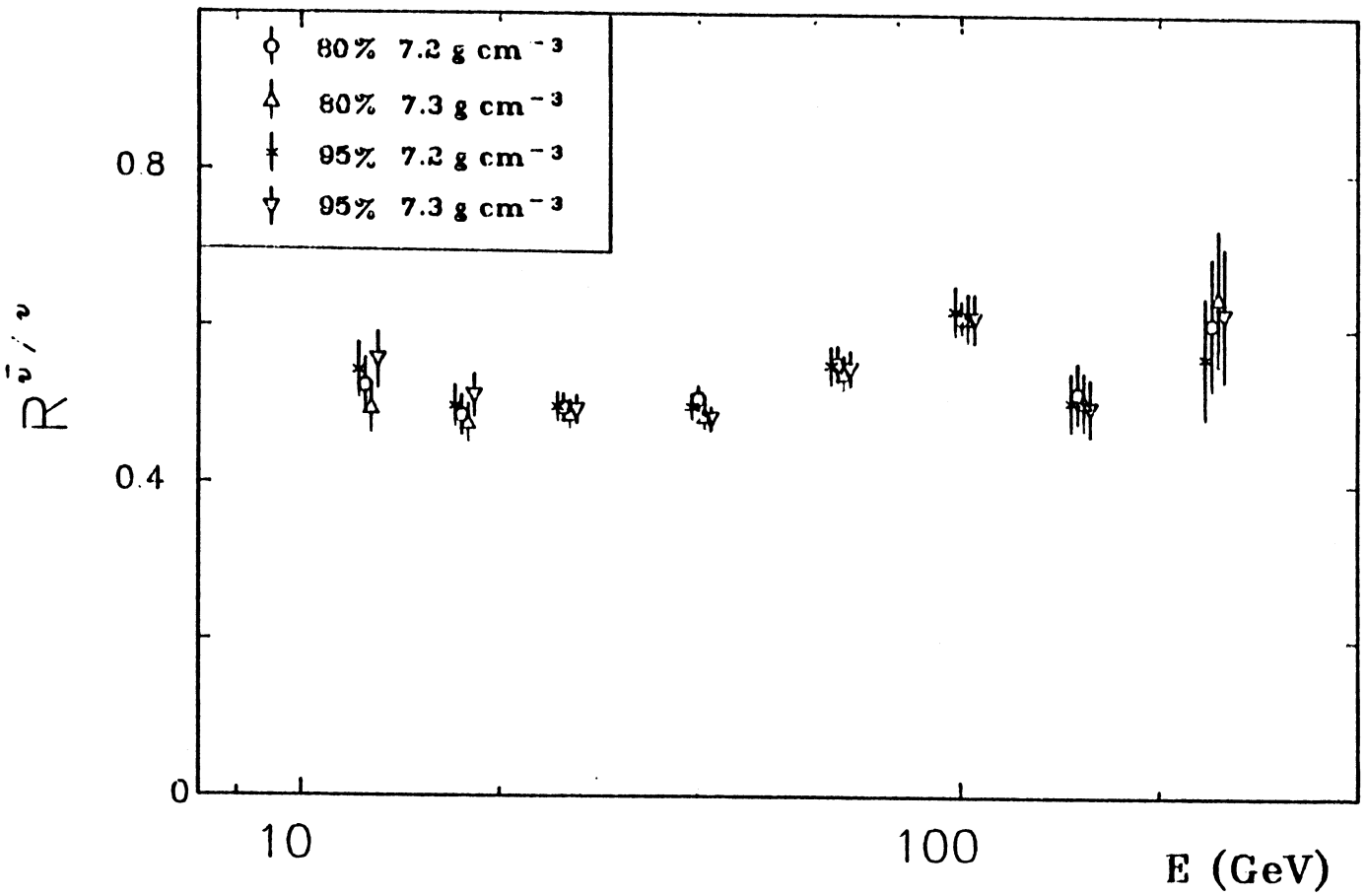

FIG 4.5 RATIO OF TOTAL NEUTRINO AND ANTINEUTRINO CROSS SECTIONS AS A FUNCTION OF NEUTRINO ENERGY FOR DIFFERENT FOCUSSING AND DENSITY ASSUMPTIONS

Fig. 4.4. The data does not suggest any significant dependence of $R^{\bar{\nu}/\nu}$ on neutrino energy. In Table 4.8 and Fig. 4.5 the cross section ratio is given for the four combinations of focussing efficiency and shielding density. In this case also, this ratio is found not to be particularly sensitive to these uncertainties.

4.4 COMPARISON WITH OTHER MEASUREMENTS

The neutrino and antineutrino total cross sections have been measured in a number of experiments besides the one discussed here. A compilation of these measurements is provided by the Particle Data Group [12]. References to the experiments contributing to the compilation may be found there.

Within the energy range accessible to this experiment, the most precise data on the total cross sections has come from the CDHS collaboration at CERN and the CCFRR collaboration at Fermilab. Both measurements were made with the use of Narrow Band neutrino and antineutrino beams. It will be noted from [12] that a systematic disagreement exists between the values obtained by these two collaborations, with the CDHS collaboration obtaining lower cross section values than the CCFRR collaboration. This has been a long standing problem in the measurement of total neutrino cross sections. Recent results from the CDHS collaboration [43], based on a recalculation of the total cross sections, produce higher values which are consistent with those of the CCFRR collaboration, thus resolving the discrepancy. The new values of the total cross sections for the CDHS collaboration are

$$\sigma^{\nu}/E = (.696 \pm .024) \times 10^{-38} cm^2/GeV$$

$$\sigma^{\bar{\nu}}/E = (.334 \pm .011) \times 10^{-38} cm^2/GeV$$

In Fig. 4.6 the present total cross section measurements are compared with measurements of the same cross sections from other experiments. All measurements with the exception of the recent CDHS values were obtained from the compilation given by the Particle Data Group in reference [12]. The reader is referred to the list of references

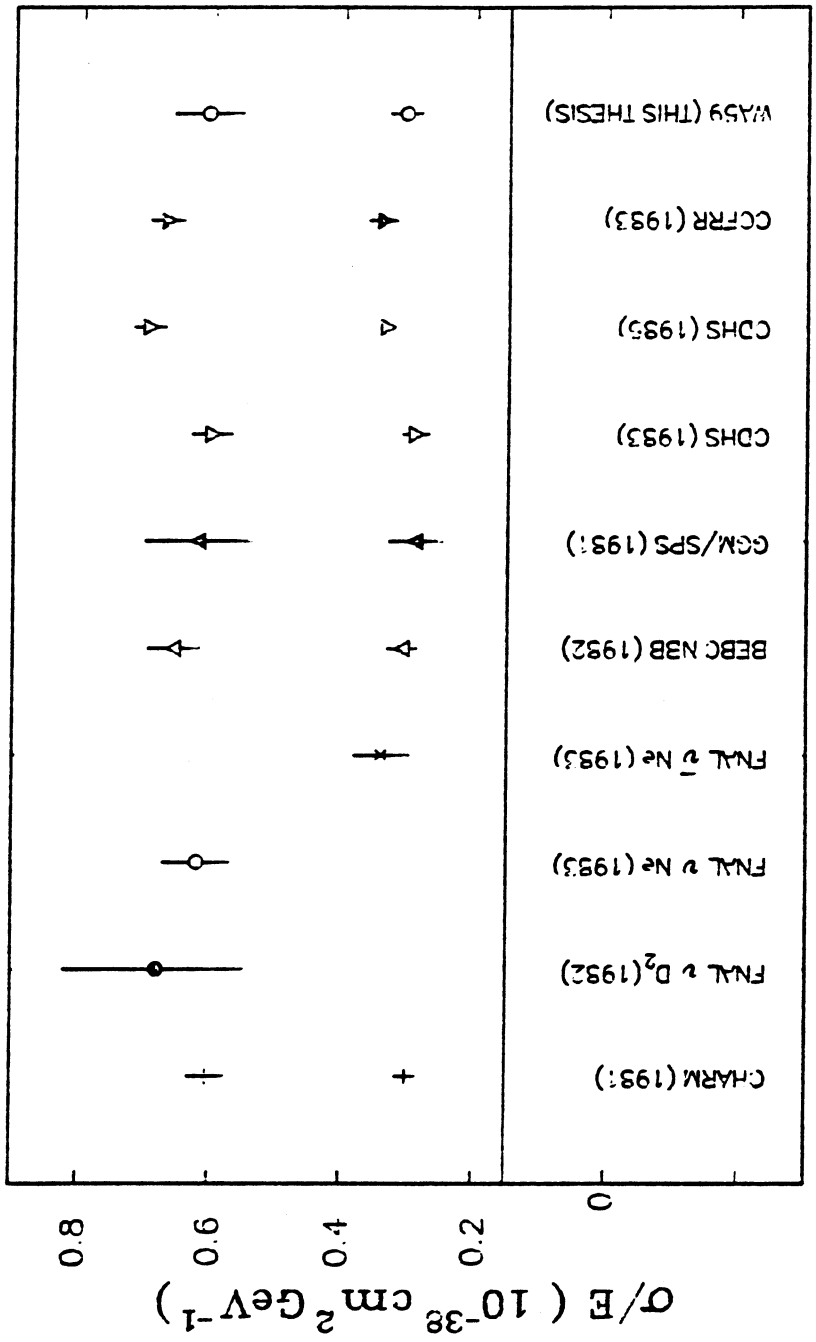

FIG 4.6 COMPARISON OF TOTAL CROSS SECTION MEASUREMENTS

contained therein for references to the individual experiments quoted here. Where experiments quoted both statistical and systematic errors these have been added linearly in the figure. The error bars on the cross sections for the present experiment also consist of the statistical error and systematic error added linearly. The present values appear consistent with all other measurements. Although both the neutrino and antineutrino cross sections are systematically lower in magnitude than the precise measurements of the CDHS and CCFRR counter experiments (in comparison to CDHS (1985), the neutrino cross section is lower by approximately 13% and the antineutrino cross section by 10%), they remain consistent within errors. The total cross section ratios of the CDHS experiment and the present one are also consistent within errors. The total cross section measurements are important in the calculation of structure functions to be considered in the following Chapter, as they affect the overall normalization of F_2 and xF_3, and it is therefore important to compare values of these quantities between experiments before comparing the structure functions themselves.

Chapter 5

THE STRUCTURE FUNCTIONS

5.1 INTRODUCTION

In Chapter 3 the method of extraction of the event distributions in the kinematic variables E, x and Q^2 was discussed. Using these distributions, the structure functions F_2 and xF_3 will be calculated in section 5.2 by what may be termed the "classical method" of combination of the neutrino and antineutrino data samples. A discussion of systematic uncertainties in the structure functions thus obtained will be given in section 5.3. In section 5.4, a comparison will be made with other published data, with due caution paid to the problem of trying to compare measurements from different experiments.

5.2 THE STRUCTURE FUNCTIONS F_2 and xF_3

Consider again the form of the differential cross section for scattering of neutrinos and antineutrinos from an isoscalar target, equation (1.15)

$$\frac{d^2\sigma^{\nu,\bar{\nu}}}{dxdy} = \frac{G^2 mE}{\pi}\left(\frac{{m_W}^2}{{m_W}^2+Q^2}\right)^2 \times \left\{2xF_1(x,Q^2)\frac{y^2}{2} + F_2(x,Q^2)\left(1-y-\frac{mxy}{2E}\right) \pm xF_3(x,Q^2)y\left(1-\frac{y}{2}\right)\right\} \tag{5.1}$$

where we have assumed the equality of the structure functions for neutrinos and antineutrinos, equation (1.19). This cross section is related to the measurable event distributions

through the differential form in x and y of equation (4.1).

$$\frac{d^3N_{ev}^{\nu,\bar{\nu}}(x,y,E)}{dxdydE} = N^T N^{\nu,\bar{\nu}} \phi^{\nu,\bar{\nu}}(E) \frac{d^2\sigma^{\nu,\bar{\nu}}(x,y,E)}{dxdy} \tag{5.2}$$

where $d^3N_{ev}^{\nu,\bar{\nu}}(x,y,E)/dxdydE$ is the number of neutrino (antineutrino) events observed in the interval $x \to x+dx, y \to y+dy, E \to E+dE$ and the remaining quantities were defined in Section 4.2.

Combining equations (5.1) and (5.2), it is possible to relate the observed quantities of numbers of events to the structure functions we wish to measure. It can be seen however that we have a system of two equations in the three unknowns $2xF_1$, F_2 and xF_3. From equations (1.12) and (1.14) it is possible to derive an expression for the ratio of the longitudinal to transverse W boson absorption cross sections

$$R \equiv \frac{\sigma_S}{\sigma_T} \equiv \frac{2\sigma_S}{\sigma_R + \sigma_L} = \frac{F_2\left(1+Q^2/\nu^2\right) - 2xF_1}{2xF_1} \tag{5.3}$$

Using this relation to eliminate $2xF_1$, equation (5.1) may be written

$$\begin{aligned}\frac{d^2\sigma^{\nu,\bar{\nu}}}{dxdy} = \frac{G^2mE}{\pi}&\left(\frac{{m_W}^2}{{m_W}^2+Q^2}\right)^2 \\ &\left\{F_2(x,Q^2)\left(1-y-\frac{mxy}{2E}+\frac{y^2}{2}\frac{\left(1+Q^2/\nu^2\right)}{(1+R)}\right) \pm xF_3(x,Q^2)y\left(1-\frac{y}{2}\right)\right\}\end{aligned} \tag{5.4}$$

F_2 and xF_3 can then be calculated assuming a value for R. The value chosen was $R = 0$, corresponding to the vanishing of the longitudinal cross section σ_S. In the limit Q^2/ν^2 small this is equivalent to assuming the Callan-Gross relation (1.22), demanded by the quark-parton model. The effect of choosing a small positive value of $R = 0.1$ on F_2 and xF_3 (as used for instance in the CDHS analysis [5]) will be investigated below, as will the choice of strict Callan-Gross, $A = 2xF_1/F_2 = 1$.

In order to obtain the number of events in a bin of x and Q^2, equation (5.2) must be integrated over the bin and over all energies. For the ith bin of x and jth bin of Q^2, we may write

$$N_{ij}^{\nu,\bar{\nu}} = I_{2ij}^{\nu,\bar{\nu}}(F_2)_{ij} \pm I_{3ij}^{\nu,\bar{\nu}}(xF_3)_{ij} \tag{5.5}$$

where the "flux integrals" $I^{\nu,\bar{\nu}}_{2ij}$, $I^{\nu,\bar{\nu}}_{3ij}$ are defined by the relations

$$I^{\nu,\bar{\nu}}_{2ij} = N^T N^{\nu,\bar{\nu}} \frac{G^2 m}{\pi} \int\int\int \left(\frac{{m_W}^2}{{m_W}^2 + Q^2}\right)^2 \left[1 - y - \frac{mxy}{2E} + \frac{y^2}{2}\frac{(1 + Q^2/\nu^2)}{(1+R)}\right] \times E\phi^{\nu,\bar{\nu}}(E) dx dy dE \tag{5.6}$$

$$I^{\nu,\bar{\nu}}_{3ij} = N^T N^{\nu,\bar{\nu}} \frac{G^2 m}{\pi} \int\int\int \left(\frac{{m_W}^2}{{m_W}^2 + Q^2}\right)^2 y\,(1 - y/2)\, E\phi^{\nu,\bar{\nu}}(E) dx dy dE \tag{5.7}$$

and $(F_2)_{ij}$, $(xF_3)_{ij}$ are the values of the respective structure functions in the bin ij.

The volume of integration in equations (5.6) and (5.7) extends over all x, y and E such that x and Q^2 lie within the bin ij. The number of observed events in bin ij may be subject to kinematic constraints imposed by the muon momentum and neutrino energy cuts. These are taken into account in the calculation of the flux integrals by appropriate modification of the volume of integration. Another constraint which affects the volume of integration in this region is the pion threshold condition defined in section 3.6.1, namely that a physical boundary exists in the $x - Q^2$ plane due to the necessity of producing, in an inelastic event, at least one baryon and one pion in the final state. This is expressed by the condition

$$W^2 = m^2 + Q^2\left(\frac{1}{x} - 1\right) \geq (m + m_\pi)^2 \tag{5.8}$$

where m is the mass of a nucleon, and m_π the pion mass. With the present choice of binning in x and Q^2, this boundary passes through the bins with $Q^2 > 0.4$ GeV^2/c^2, the bin $0.4 < Q^2 < 0.6$ GeV^2/c^2, $0.4 < x < 0.6$, and the high x bins $0.6 < x < 1$. It is responsible for the total lack of data in the bin $0. < Q^2 < 0.4$ GeV^2/c^2, $0.6 < x < 1.$, which lies entirely beyond the pion threshold. In some sense it is arguable whether the pion threshold condition should be imposed in calculating the flux integrals, for the reason that in doing so one presupposes and inputs some knowledge of the dynamics of the process about which one hopes to learn by measuring the structure functions (the dynamics being that the threshold exists at all). In an ideal experiment with infinite statistics and vanishingly small bins, the same value for the structure function would be obtained everywhere whether or not the threshold condition is imposed, whereas in the present case imposing or leaving out the threshold affects the value of the (bin averaged) structure function obtained in bins through which it passes. This is purely a consequence

of the finite and sometimes large bins of x and Q^2 used. For the present analysis the pion threshold was imposed on the flux integrals, with the understanding that the structure function quoted is an average over the reduced $x-Q^2$ bin lying within the pion threshold, and is in fact zero without.

The physical interpretation of, for example, the flux integral I^{ν}_{2ij} is the number of neutrino induced events that would be observed in bin ij if the corresponding structure function $(F_2)_{ij}=1$ and all other structure functions (in this case $(xF_3)_{ij}$) are zero. As the flux integrals are expressed entirely in terms of known quantities, and can be evaluated numerically, equations (5.5) may be solved in each bin ij for $(F_2)_{ij}$ and $(xF_3)_{ij}$.

The bins in x and Q^2 chosen for the present analysis were the following

x $\quad 0.-.1,\ \ .1-.2,\ \ .2-.3,\ \ .3-.4,\ \ .4-.6,\ \ .6-1.$

Q^2 $\quad 0.-.4,\ \ .4-1.,\ \ 1.-2.,\ \ 2.-4.,\ \ 4.-8.,\ \ 8.-16.,\ \ 16.-64.,\ \ 64.-200.(GeV^2/c^2)$

This particular choice was made in order to obtain both a suitable number of events in each bin considered, and to ensure that the majority of events for which the measured x and Q^2 lie within a given bin also possess a true x and Q^2 in the same bin. The second requirement was tested using the Monte Carlo, for which both the true and measured $x-Q^2$ planes are modelled.

In Table 5.1 the computed values of the flux integrals I^{ν}_2, I^{ν}_3, $I^{\bar{\nu}}_2$ and $I^{\bar{\nu}}_3$ are given, for the chosen value of $R=0$. The values of N^T, $N^{\nu,\bar{\nu}}$ and the flux $\phi^{\nu,\bar{\nu}}(E)$ were given in section 4.2. The value used for the W boson mass was m_W =80.9 GeV/c^2 [44]. The effect of the propagator term in equations (5.6) and (5.7) is small for the Q^2 range accessible to the present experiment, amounting to a .97% correction at the mean Q^2 =89 GeV^2/c^2 of the highest Q^2 bin considered.

The $x-Q^2$ planes for the neutrino and antineutrino samples obtained using the selection criteria and corrections of sections 3.2-3.5 are given in Tables 5.2a,b. The Myatt method was used to estimate the neutrino energy as outlined in section 3.6. A correction for the non-isoscalarity of the target of 1.0078 for the neutrino sample and 0.9924 for the antineutrino sample was applied.

Table 5.1 : Flux integrals

$Q^2(GeV^2/c^2)$	x	I_2^ν	$I_2^{\bar{\nu}}$	I_3^ν	$I_3^{\bar{\nu}}$
0.–.4	0.–.1	376.4	1235.0	83.7	282.0
	.1–.2	88.6	303.6	3.6	13.7
	.2–.3	46.7	157.6	1.2	4.5
	.3–.4	27.3	91.7	0.5	2.0
	.4–.6	18.3	61.9	0.3	1.2
	.6–1.	–	–	–	–
	Elastic	140.0	515.5	0.9	3.3
.4–1.	0.–.1	263.6	818.6	99.1	323.3
	.1–.2	137.0	470.6	18.3	68.8
	.2–.3	84.0	291.1	6.4	24.0
	.3–.4	60.8	210.8	3.2	12.2
	.4–.6	88.8	302.9	3.2	12.3
	.6–1.	35.4	118.8	1.0	3.9
	Elastic	229.3	772.0	4.0	15.0
1.–2.	0.–.1	220.6	626.2	108.9	330.4
	.1–.2	192.3	647.8	51.8	192.1
	.2–.3	130.0	445.4	21.4	80.5
	.3–.4	96.4	331.6	11.1	41.7
	.4–.6	139.7	483.2	11.3	42.7
	.6–1.	116.4	405.9	6.6	25.0
	Elastic	356.6	1222.3	13.7	51.6
2.–4.	0.–.1	185.4	446.2	111.1	288.9
	.1–.2	256.0	806.7	106.7	371.7
	.2–.3	212.6	710.5	64.0	235.9
	.3–.4	172.3	586.6	39.6	148.2
	.4–.6	260.1	891.7	42.8	160.9
	.6–1.	281.8	970.0	30.6	115.0
	Elastic	696.5	2413.1	55.0	207.4

Table 5.1 (cont.)

$Q^2(GeV^2/c^2)$	x	I_2^ν	$I_2^{\overline{\nu}}$	I_3^ν	$I_3^{\overline{\nu}}$
4.–8.	0.–.1	117.3	209.7	81.4	156.2
	.1–.2	253.3	682.5	140.6	420.9
	.2–.3	265.6	816.7	120.3	410.4
	.3–.4	246.7	798.2	92.8	332.4
	.4–.6	425.7	1423.5	127.9	471.4
	.6–1.	566.5	1933.1	120.2	450.5
	Elastic	1292.7	4431.8	206.8	776.9
8.–16.	0.–.1	53.9	64.0	43.4	53.8
	.1–.2	180.5	355.2	119.1	258.2
	.2–.3	241.0	611.2	141.0	398.8
	.3–.4	265.4	754.0	139.6	441.5
	.4–.6	531.7	1635.8	240.1	819.3
	.6–1.	891.5	2918.6	313.8	1133.8
	Elastic	2124.1	7117.4	628.4	2320.3
16.–64.	0.–.1	10.3	6.8	9.3	6.3
	.1–.2	117.2	134.3	95.3	113.3
	.2–.3	234.6	358.0	172.8	279.2
	.3–.4	319.4	591.7	218.5	435.8
	.4–.6	799.5	1777.4	499.8	1212.7
	.6–1.	1880.8	4973.0	1036.6	3007.1
	Elastic	5093.6	14423.8	2602.7	8095.1
64.–200.	0.–.1	0.0	0.0	0.0	0.0
	.1–.2	0.4	0.1	0.4	0.1
	.2–.3	8.3	3.8	7.7	3.6
	.3–.4	31.6	22.8	28.4	21.0
	.4–.6	163.3	163.7	138.0	143.1
	.6–1.	671.5	923.3	511.6	740.6
	Elastic	2169.0	3414.3	1567.4	2636.1

Table 5.2a : Neutrino $x - Q^2$ Event Plane

		Q^2 (GeV^2/c^2)								
		0.–.4	.4–1.	1.–2.	2.–4.	4.–8.	8.–16.	16.–64.	64.–200.	Total
	0.–.1	209.5±15.3	241.6±16.3	293.3±17.8	249.3±16.3	200.8±14.6	120.0±14.6	51.4±7.3	4.2±2.1	1370.1±38.5
	.1–.2	46.3±7.2	119.2±11.4	174.6±13.7	373.3±19.9	365.5±19.7	263.7±16.8	203.9±14.7	10.1±3.2	1556.7±40.8
x	.2–.3	19.9±4.7	53.3±7.6	103.6±10.5	209.0±15.1	317.9±18.5	298.0±17.9	316.6±18.4	23.9±5.0	1342.3±38.0
	.3–.4	13.8±4.0	31.2±5.9	41.1±6.7	126.9±11.7	201.7±14.8	206.7±15.0	300.9±18.0	31.3±5.8	953.6±32.2
	.4–.6	13.8±3.9	24.6±5.2	41.3±6.7	99.5±10.5	155.4±13.2	193.8±14.7	282.7±17.9	62.3±8.3	873.3±31.2
	.6–1.	–	28.2±5.7	34.1±6.2	50.3±7.5	76.4±9.3	71.0±9.0	99.5±10.8	25.2±5.3	384.7±20.9
	Elastic	119.9±20.9	53.8±9.8	25.0±5.4	14.2±5.7	1.2±1.2	9.3±6.6	–	–	223.3±25.3
	Total	423.1±27.9	551.9±25.4	712.9±27.8	1122.6±35.0	1319.0±37.7	1162.6±36.0	1255.0±37.0	157.0±13.1	6704.2±87.6

Table 5.2b : Antineutrino $x - Q^2$ Event Plane

		Q^2 (GeV^2/c^2)								
		0.–.4	.4–1.	1.–2.	2.–4.	4.–8.	8.–16.	16.–64.	64.–200.	Total
	0.–.1	615.3±25.6	621.4±25.6	536.2±23.8	433.3±21.5	212.2±14.9	84.8±9.4	38.0±6.3	1.6±1.6	2542.7±51.9
	.1–.2	155.2±12.8	305.6±17.9	481.1±22.5	595.0±24.9	486.0±22.6	232.3±15.6	90.1±9.7	3.7±2.2	2348.9±49.6
x	.2–.3	72.7±8.8	184.9±14.0	277.1±17.1	437.7±21.5	405.7±20.6	265.2±16.7	123.5±11.4	9.4±3.2	1776.2±43.3
	.3–.4	41.4±6.7	88.7±9.6	160.3±13.0	239.8±15.9	304.3±18.0	200.4±14.5	105.6±10.5	4.6±2.3	1145.1±34.8
	.4–.6	88.8±9.7	83.7±9.4	163.2±13.2	252.5±16.3	298.1±17.8	205.6±14.9	149.6±12.6	6.5±2.7	1248.0±36.5
	.6–1.	–	167.6±13.3	176.0±13.7	163.3±13.2	133.6±12.0	125.8±11.6	57.4±7.8	1.1±1.1	824.8±29.7
	Elastic	352.2±21.1	199.7±15.8	65.6±9.1	19.8±5.0	3.9±2.2	3.8±2.2	–	–	645.1±28.5
	Total	1325.7±38.5	1651.8±42.2	1859.5±44.4	2141.3±47.6	1843.8±44.1	1117.9±34.4	564.0±24.4	26.8±5.5	10531.0±106.1

Unsmearing factors were calculated using the Monte Carlo described in section 3.7, and have been given previously in Tables 3.4a,b. Using these factors to unsmear the above event planes, and the computed values of the flux integrals, equation (5.5) was solved in each bin of x and Q^2 for the structure functions F_2 and xF_3.

Due to the finite size of the bins of x and Q^2 used to extract the structure functions, the actual x and Q^2 point within the bin corresponding to the value of the structure function obtained cannot be specified. A reasonable assumption to make, and one that is adopted here, is that this point is the mean x and Q^2 of the bin. A small problem arises, however, if the structure functions are to be used for further analysis of the type suggested in Section 1.4. The calculation of moments, for example, requires integration of the structure functions over x at fixed Q^2, whereas for a given Q^2 bin, the mean Q^2 may vary over the x region considered. To overcome this, bin centring was performed using the parametrization of Perkins, Schreiner and Scott [37]

$$F_2(x, {Q_1}^2) = F_2(x, {Q_0}^2)\left(\frac{{Q_1}^2}{{Q_0}^2}\right)^{.25-x} \tag{5.9}$$

where x is taken as the mean x of the $x - Q^2$ bin considered, ${Q_0}^2$ as the mean Q^2 of this $x - Q^2$ bin, and ${Q_1}^2$ as the mean Q^2 of the Q^2 bin taken over all x. In this way, for a given Q^2 bin, all structure function points will lie at the same mean Q^2, common to the whole x region. These bin centring corrections are small, and are given in Table 5.3. If an overall fit to the $x - Q^2$ evolution of the structure functions were to be performed, where the mean $x - Q^2$ of each bin was used as input, bin centring corrections would in fact not be necessary.

The values of the structure functions F_2 and xF_3, following bin centring corrections, are given in Tables 5.4a,b. Errors quoted correspond simply to the statistical errors on the event numbers. Figures 5.1a,b give a graphical representation of the measured values of F_2 and xF_3 as functions of Q^2 for each x bin, with the points plotted at the mean Q^2 of each bin. An immediate point to note from the Figure is that scaling is seen to be broken in the present data, in the familiar pattern of structure functions rising with Q^2 at low

Table 5.3 : Bin Centring Corrections

		Q^2 (GeV^2/c^2)							
		0.–.4	.4–1.	1.–2.	2.–4.	4.–8.	8.–16.	16.–64.	64.–200.
	0.–.1	1.019	1.006	1.004	1.003	1.001	1.004	1.005	–
	.1–.2	0.988	0.995	0.999	1.001	1.001	1.001	1.005	0.993
x	.2–.3	0.999	1.000	1.000	1.000	1.000	1.000	1.000	1.001
	.3–.4	1.021	1.004	1.003	1.003	1.001	1.000	1.006	0.991
	.4–.6	1.092	1.002	1.006	1.003	1.002	1.004	1.002	1.002
	.6–1.	–	1.019	0.993	0.988	1.014	1.024	0.998	0.978

Table 5.4a : Structure Function F_2

$Q^2(GeV^2/c^2)$	x	F_2	(i)	(ii)	(iii)	$R = 0.1$	$A = 1$
0.-.4	0.-.1	0.657 ± 0.029	−0.031	+0.008	−0.004	+0.004	+0.000
	.1-.2	0.708 ± 0.065	+0.009	+0.018	+0.095	+0.000	+0.000
	.2-.3	0.613 ± 0.085	+0.126	−0.068	+0.092	+0.000	+0.000
	.3-.4	0.549 ± 0.099	+0.203	−0.176	+0.011	+0.000	+0.000
	.4-.6	0.398 ± 0.050	+0.301	−0.139	+0.022	+0.000	+0.000
	.6-1.	-	-	-	-	-	-
	Elastic	0.346 ± 0.033	+0.077	+0.027	−0.016	+0.000	+0.000
.4-1.	0.-.1	0.905 ± 0.038	−0.014	−0.021	−0.028	+0.010	+0.001
	.1-.2	0.897 ± 0.055	−0.030	+0.105	+0.083	+0.001	+0.001
	.2-.3	0.858 ± 0.073	+0.002	+0.005	+0.109	+0.000	+0.001
	.3-.4	0.654 ± 0.080	+0.036	+0.007	+0.088	+0.000	+0.001
	.4-.6	0.317 ± 0.040	+0.144	−0.041	+0.018	+0.000	+0.000
	.6-1.	0.172 ± 0.017	+0.108	−0.071	−0.017	+0.000	+0.000
	Elastic	0.139 ± 0.012	−0.005	−0.004	−0.005	+0.000	+0.000
1.-2.	0.-.1	1.095 ± 0.046	+0.020	+0.042	−0.062	+0.020	+0.001
	.1-.2	0.909 ± 0.045	−0.035	−0.032	+0.041	+0.005	+0.002
	.2-.3	0.839 ± 0.055	−0.028	+0.070	+0.089	+0.002	+0.002
	.3-.4	0.567 ± 0.051	+0.015	+0.039	+0.040	+0.001	+0.001
	.4-.6	0.376 ± 0.034	+0.029	−0.019	+0.031	+0.000	+0.001
	.6-1.	0.127 ± 0.013	+0.057	−0.028	−0.017	+0.000	+0.000
	Elastic	0.038 ± 0.005	+0.001	−0.003	+0.002	+0.000	+0.000
2.-4.	0.-.1	1.080 ± 0.049	+0.078	−0.017	−0.115	+0.028	+0.001
	.1-.2	1.178 ± 0.046	−0.027	+0.007	+0.014	+0.015	+0.004
	.2-.3	0.864 ± 0.042	+0.002	+0.007	+0.074	+0.006	+0.004
	.3-.4	0.657 ± 0.043	+0.002	+0.036	+0.052	+0.003	+0.004
	.4-.6	0.366 ± 0.025	+0.008	−0.002	+0.031	+0.001	+0.002
	.6-1.	0.097 ± 0.009	+0.020	−0.009	−0.001	+0.000	+0.000
	Elastic	0.009 ± 0.002	+0.000	−0.001	+0.002	+0.000	+0.000

(i) Change due to using Buras and Gaemers Input Distributions
(ii) Change due to including Fermi Motion
(iii) Change due to including radiative corrections
No entry indicates a lack of data in this bin

Table 5.4a (cont.)

$Q^2(GeV^2/c^2)$	x	F_2	(i)	(ii)	(iii)	$R = 0.1$	$A = 1$
4.–8.	0.–.1	1.130 ± 0.062	+0.100	+0.034	−0.128	+0.040	+0.001
	.1–.2	1.118 ± 0.045	+0.001	+0.013	−0.009	+0.026	+0.004
	.2–.3	0.920 ± 0.041	−0.024	+0.020	+0.032	+0.014	+0.005
	.3–.4	0.653 ± 0.035	−0.008	−0.018	+0.043	+0.007	+0.005
	.4–.6	0.311 ± 0.018	+0.000	+0.070	+0.020	+0.002	+0.003
	.6–1.	0.082 ± 0.007	+0.005	−0.026	+0.001	+0.000	+0.001
	Elastic	0.001 ± 0.001	−0.000	−0.000	−0.000	+0.000	+0.000
8.–16.	0.–.1	1.317 ± 0.099	+0.070	−0.015	−0.298	+0.063	+0.001
	.1–.2	1.037 ± 0.052	+0.024	+0.041	−0.061	+0.034	+0.003
	.2–.3	0.882 ± 0.043	+0.002	+0.069	+0.010	+0.023	+0.005
	.3–.4	0.562 ± 0.033	−0.010	+0.002	+0.011	+0.012	+0.005
	.4–.6	0.264 ± 0.016	+0.005	−0.009	+0.020	+0.004	+0.003
	.6–1.	0.056 ± 0.005	−0.000	−0.008	+0.004	+0.001	+0.001
	Elastic	0.001 ± 0.000	+0.001	−0.000	+0.000	+0.000	+0.000
16.–64.	0.–.1	1.277 ± 0.149	+0.091	+0.059	−0.383	+0.082	+0.001
	.1–.2	1.080 ± 0.066	−0.001	+0.114	−0.133	+0.053	+0.002
	.2–.3	0.874 ± 0.044	−0.015	−0.018	−0.029	+0.035	+0.003
	.3–.4	0.589 ± 0.031	+0.004	+0.015	+0.014	+0.021	+0.004
	.4–.6	0.233 ± 0.013	−0.000	+0.005	+0.009	+0.007	+0.002
	.6–1.	0.031 ± 0.003	+0.001	−0.005	+0.002	+0.001	+0.001
	Elastic	–	–	–	–	–	–
64.–200.	0.–.1	–	–	–	–	–	–
	.1–.2	1.231 ± 0.350	−0.322	+0.101	−0.619	+0.098	+0.002
	.2–.3	1.097 ± 0.197	−0.262	+0.134	−0.315	+0.077	+0.003
	.3–.4	0.493 ± 0.086	+0.008	+0.016	−0.020	+0.031	+0.002
	.4–.6	0.219 ± 0.028	+0.001	−0.003	+0.008	+0.012	+0.001
	.6–1.	0.020 ± 0.004	−0.001	−0.002	+0.000	+0.001	+0.000
	Elastic	–	–	–	–	–	–

Table 5.4b : Structure Function xF_3

$Q^2(GeV^2/c^2)$	x	xF_3	(i)	(ii)	(iii)	$R = 0.1$	$A = 1$
0.-.4	0.-.1	0.183 ± 0.127	−0.015	−0.011	−0.025	−0.000	−0.000
	.1-.2	0.733 ± 1.472	−0.148	+0.253	+0.466	−0.000	−0.001
	.2-.3	0.171 ± 3.058	+0.216	−0.171	+0.048	+0.000	−0.000
	.3-.4	2.613 ± 4.545	+0.173	−3.029	−0.257	−0.000	−0.001
	.4-.6	-6.459 ± 2.662	−5.676	+3.296	+0.252	+0.000	−0.001
	.6-1.	-	-	-	-	-	-
	Elastic	2.698 ± 5.294	+2.442	+3.164	+2.336	+0.000	−0.001
.4-1.	0.-.1	0.260 ± 0.098	−0.015	−0.113	−0.023	−0.001	−0.000
	.1-.2	0.982 ± 0.384	−0.057	+0.527	+0.105	−0.001	−0.001
	.2-.3	0.427 ± 0.896	+0.019	−1.392	+0.360	+0.000	−0.001
	.3-.4	1.905 ± 1.402	+0.063	−0.022	+0.021	−0.000	−0.001
	.4-.6	0.171 ± 0.999	+1.143	−0.130	+0.656	−0.000	−0.001
	.6-1.	-0.966 ± 0.528	−0.037	+0.636	−0.140	−0.000	−0.001
	Elastic	-2.053 ± 0.640	+0.307	+0.206	+0.550	−0.000	−0.001
1.-2.	0.-.1	0.519 ± 0.088	−0.005	+0.106	+0.001	−0.002	−0.000
	.1-.2	0.338 ± 0.154	+0.003	+0.029	+0.012	−0.001	−0.001
	.2-.3	0.660 ± 0.308	−0.024	−0.199	+0.035	−0.001	−0.001
	.3-.4	-0.233 ± 0.416	+0.038	+0.499	−0.242	−0.001	−0.001
	.4-.6	-0.223 ± 0.393	+0.182	+0.399	+0.210	−0.000	−0.001
	.6-1.	-0.060 ± 0.209	+0.007	−0.121	−0.138	−0.000	−0.000
	Elastic	-0.340 ± 0.114	−0.036	+0.064	+0.035	−0.000	−0.000
2.-4.	0.-.1	0.415 ± 0.077	−0.033	−0.058	−0.050	−0.003	−0.000
	.1-.2	0.893 ± 0.101	+0.002	+0.027	+0.016	−0.003	−0.001
	.2-.3	0.580 ± 0.129	+0.058	+0.045	+0.091	−0.001	−0.001
	.3-.4	0.813 ± 0.173	−0.086	−0.063	−0.022	−0.001	−0.001
	.4-.6	0.296 ± 0.139	−0.027	+.0792	+0.019	−0.000	−0.001
	.6-1.	0.072 ± 0.076	+0.024	+0.009	+0.016	−0.000	−0.000
	Elastic	-0.045 ± 0.025	+0.000	+0.005	+0.006	−0.000	−0.000

(i) Change due to using Buras and Gaemers Input Distributions
(ii) Change due to including Fermi Motion
(iii) Change due to including radiative corrections
No entry indicates a lack of data in this bin

Table 5.4b (cont.)

$Q^2(GeV^2/c^2)$	x	xF_3	(i)	(ii)	(iii)	$R = 0.1$	$A = 1$
4.–8.	0.–.1	0.571 ± 0.084	+0.009	−0.013	−0.037	−0.003	−0.000
	.1–.2	0.691 ± 0.074	+0.009	−0.019	+0.029	−0.004	−0.001
	.2–.3	0.806 ± 0.083	−0.022	+0.000	+0.017	−0.002	−0.001
	.3–.4	0.571 ± 0.086	−0.000	+0.028	+0.054	−0.001	−0.001
	.4–.6	0.258 ± 0.056	−0.010	−0.167	+0.003	−0.001	−0.001
	.6–1.	0.121 ± 0.031	+0.011	+0.035	+0.005	−0.000	−0.000
	Elastic	-0.005 ± 0.003	+0.002	+0.003	+0.004	−0.000	−0.000
8.–16.	0.–.1	0.755 ± 0.119	−0.051	−0.063	−0.098	−0.003	−0.000
	.1–.2	0.618 ± 0.072	+0.012	−0.052	+0.010	−0.004	−0.000
	.2–.3	0.683 ± 0.066	+0.018	+0.039	+0.015	−0.003	−0.001
	.3–.4	0.492 ± 0.057	−0.007	−0.000	−0.003	−0.002	−0.001
	.4–.6	0.261 ± 0.032	+0.003	−0.031	+0.022	−0.001	−0.001
	.6–1.	0.038 ± 0.013	+0.003	+0.005	+0.007	−0.000	−0.000
	Elastic	0.000 ± 0.001	−0.000	−0.001	+0.001	−0.000	−0.000
16.–64.	0.–.1	0.752 ± 0.161	−0.052	+0.030	−0.234	−0.003	−0.000
	.1–.2	0.710 ± 0.079	+0.012	+0.044	−0.045	−0.002	−0.000
	.2–.3	0.708 ± 0.057	+0.006	+0.059	−0.006	−0.003	−0.000
	.3–.4	0.563 ± 0.043	+0.007	+0.006	+0.007	−0.002	−0.001
	.4–.6	0.216 ± 0.019	−0.003	+0.004	+0.008	−0.001	−0.000
	.6–1.	0.033 ± 0.005	+0.001	−0.005	+0.003	−0.000	−0.000
	Elastic	-	-	-	-	-	-
64.–200.	0.–.1	-	-	-	-	-	-
	.1–.2	0.523 ± 0.359	+0.406	−0.220	+0.102	−0.002	−0.000
	.2–.3	0.590 ± 0.208	+0.019	+0.149	+0.012	−0.002	−0.000
	.3–.4	0.414 ± 0.094	+0.023	+0.005	−0.007	−0.031	−0.000
	.4–.6	0.210 ± 0.032	+0.002	−0.009	+0.007	−0.001	−0.000
	.6–1.	0.024 ± 0.005	−0.001	−0.002	+0.001	−0.000	−0.000
	Elastic	-	-	-	-	-	-

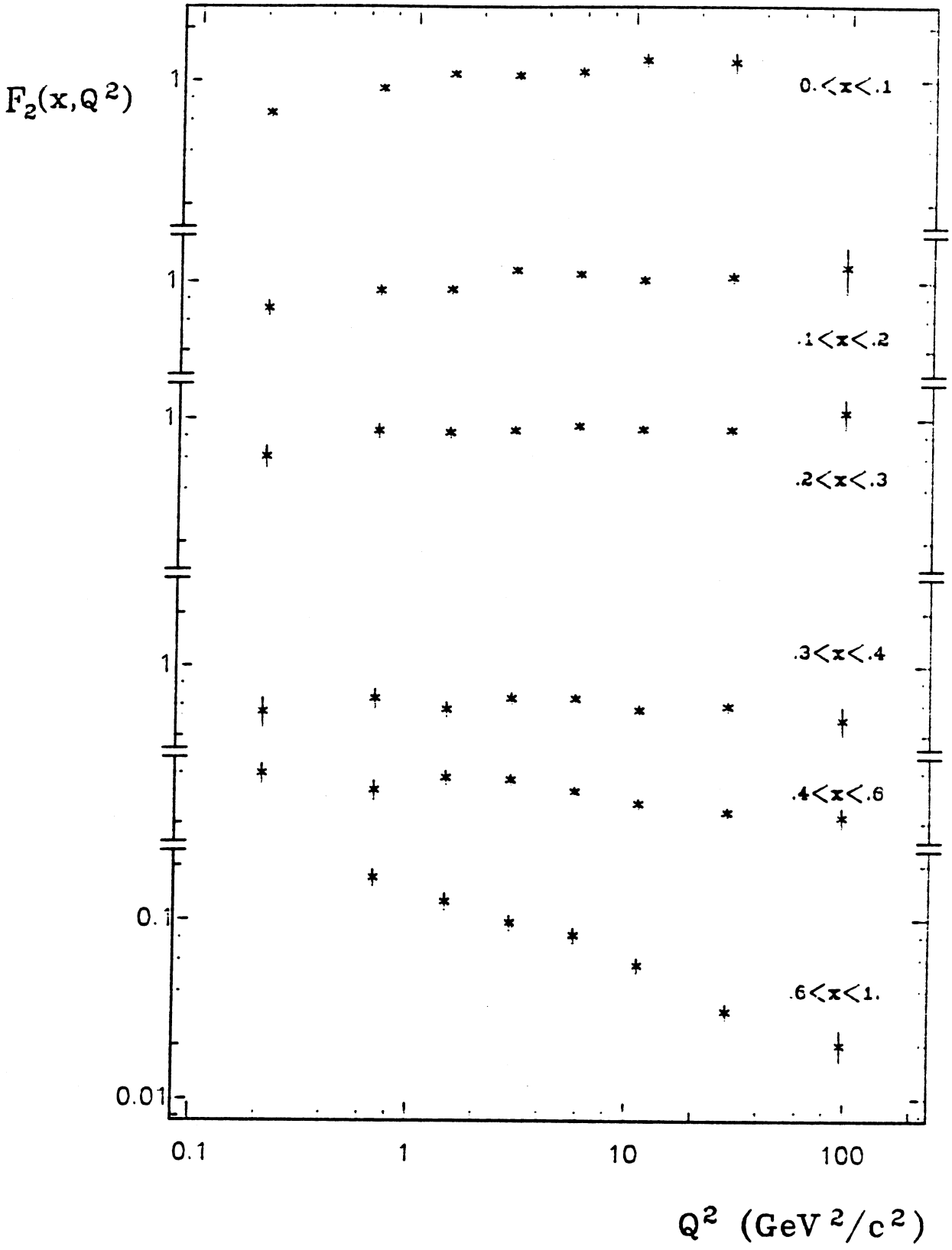

FIG 5.1a STRUCTURE FUNCTION $F_2(x,Q^2)$

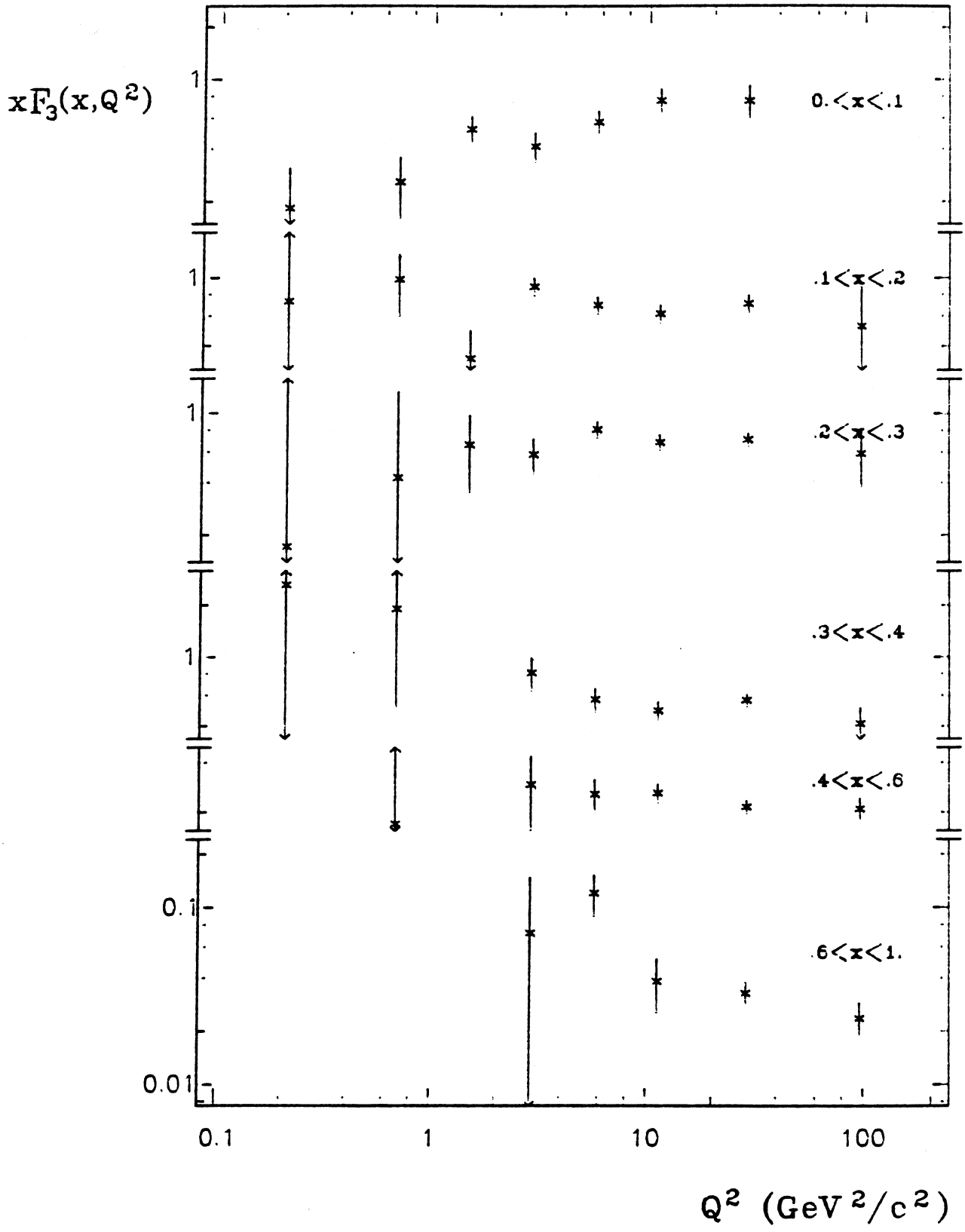

FIG 5.1b STRUCTURE FUNCTION $xF_3(x,Q^2)$

x and falling with Q^2 at high x. Questions of the exact details and cause of this scaling violation are left to the following Chapters.

5.3 SYSTEMATIC UNCERTAINTIES IN THE MEASUREMENT OF F_2 AND xF_3

The present method of extraction of structure functions suffers from two forms of systematic uncertainty, that introduced by the assumptions inherent in the Monte Carlo, which manifests itself through uncertainty in the unsmearing factors, and secondly, the necessity to assume a value for $R = \sigma_s/\sigma_T$. These two types of uncertainty are now considered.

5.3.1 UNCERTAINTIES IN THE UNSMEARING CALCULATION

Sources of uncertainty in the unsmearing calculation have been discussed previously in section 3.7.3, where the effect of varying several of the input assumptions in the Monte Carlo was investigated. The changes induced in the structure functions F_2 and xF_3 by these changes in the unsmearing factors are presented in the columns labelled (i) to (iii) of Tables 5.4a,b, and displayed graphically in Figs. 5.2a,b.

Consider first the effect of employing the parametrization of Buras and Gaemers. Over the region of the kinematic plane for which the true Buras and Gaemers Q^2 dependence was used in the CARLO program, $Q^2 > 1.8$ GeV^2/c^2 (see section 3.7.2), the change induced in both F_2 and xF_3 is almost exclusively less significant than the size of the statistical errors. For $Q^2 < 1.8$ GeV^2/c^2, where an extrapolation was used, the variation in the unsmearing factors for $x > .2$ which was noted in the discussion of section 3.7.3 is reflected in an increase in the value of F_2 of, in the most extreme case, 75%. For xF_3, the size of the statistical errors in this region is such that the effect of the change in the input distributions in this region is not clear. This is true also for the two other systematic effects now to be discussed.

When Fermi motion effects are enabled in the Monte Carlo, the only statistically significant changes induced in the structure functions are a decrease in the F_2 values in

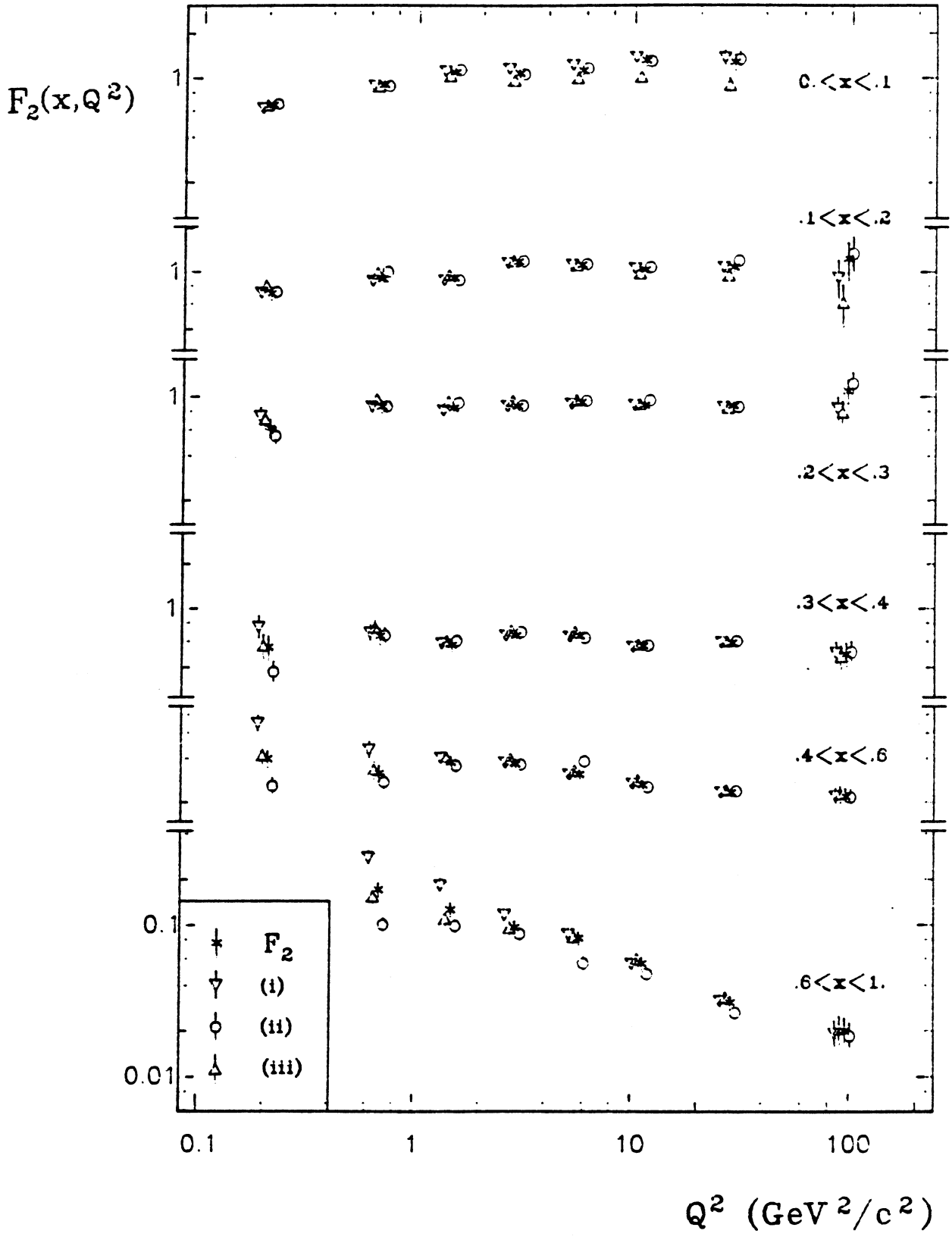

FIG 5.2a STRUCTURE FUNCTION $F_2(x,Q^2)$

SYSTEMATIC UNCERTAINTIES

(i) Buras and Gaemers

(ii) Fermi Motion

(iii) Radiative Corrections

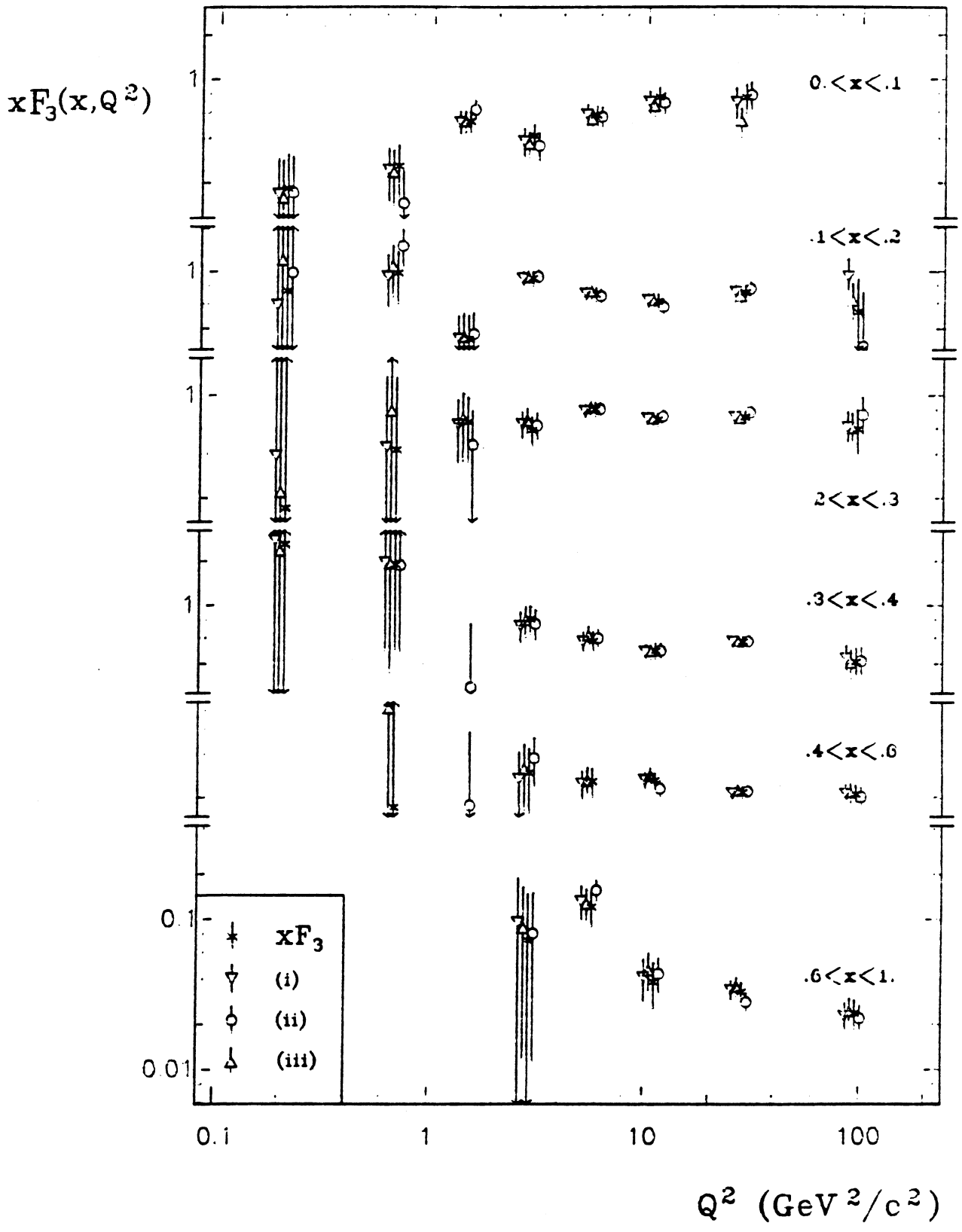

FIG 5.2b STRUCTURE FUNCTION $xF_3(x,Q^2)$

SYSTEMATIC UNCERTAINTIES

(i) Buras and Gaemers

(ii) Fermi Motion

(iii) Radiative Corrections

the high x bin x >.6. This decrease is of the order of 10 – 15% at high Q^2, but becomes as large as 40% for the bin .4 < Q^2 < 1. GeV^2/c^2, .6 < x < 1.

Inclusion of radiative corrections in the Monte Carlo produces a significant decrease in F_2 for low x, 0. < x < .1, varying from ~ 3% for .4 < Q^2 < 1. GeV^2/c^2 to ~ 30% for 16. < Q^2 < 64. GeV^2/c^2. For high Q^2 the effect can also be observed to some extent for x >.1. For xF_3 any systematic effect due to radiative corrections remains at the level of the statistical errors on the structure function.

The general conclusion drawn from the above discussion is that if restricted to the kinematic region Q^2 > 2. GeV^2/c^2, x <.6, systematic uncertainties in the extracted values of the structure functions are not large, with the exception that the effect of radiative corrections for low x and high Q^2 may play a role. For x > .6, unsmearing corrections are large and Fermi motion effects become important, with corresponding introduction of large systematic uncertainties in the structure functions. It may be possible to measure structure functions to higher x than .6 with greater control over the systematic uncertainties if the very high x region is excluded. This approach is in fact adopted below in comparison with another experiment, when the x region above .8 is omitted. For Q^2 < 2. GeV^2/c^2, especially for large x, systematic uncertainties dominate the structure function measurements, as was discussed in section 3.7.3 and is now evidenced by the values of F_2 and xF_3 given in Tables 5.4a,b. In the low W^2 region it will be noted that negative values of xF_3 are obtained (even considering the statistical errors), including the elastic structure functions. This is interpreted as being predominantly due to the inability of the CARLO program to model the production and possible subsequent reinteractions of dominant exclusive channels in this region, and both the F_2 and xF_3 data obtained in this region must therefore be questioned.

5.3.2 UNCERTAINTIES IN THE VALUE OF R

The structure functions presented in Tables 5.4a,b and Figs. 5.1a,b were extracted under the assumption $R = \sigma_s/\sigma_T = 0$. Some constraint relating $2xF_1$ and F_2 was necessary

in order to leave only two unknowns F_2 and xF_3 in the two equations embodied in (5.1). Motivation for such a choice is somewhat arbitrary, and equally reasonable choices have been made in the structure function analyses of other experiments (see section 5.4). The simple quark-parton model demands $A = 2xF_1/F_2 = 1$, a strict adherence to the Callan-Gross relation. From equation (5.3) it follows that $A = 1$ corresponds to choosing $R = Q^2/\nu^2$. Thus the two choices become equivalent for Q^2/ν^2 small. In the kinematic region accessible to the present experiment, however, the two choices lead to slightly differing results.

The simple quark-parton model is not expected to fully describe the scattering processes under consideration here, and in fact next to leading order QCD predicts a non-zero value for R [23]. Hence a choice for R such as 0.1 is not unreasonable. Unfortunately the value of R as a function of x and Q^2 is a quantity poorly determined from all existing data [45]. There is limited scope for determining R from the present data, and this will be discussed in Chapter 7.

In Tables 5.4a,b, the final two columns give the changes induced in the measured values of F_2 and xF_3 from the choices of $R = 0.1$ and $A = 1$ rather than $R = 0$. For F_2 the choice of $A = 1$ produces only very small changes in the measured structure function, at less than the 1% level over the entire kinematic region. The choice $R = 0.1$ induces significant changes only for low x and high Q^2, where an increase in F_2 is observed at a maximum level of 8% for the bin 64. $< Q^2 <$ 200. GeV^2/c^2, .1 $< x <$ .2. In general, however, the value of F_2 is less sensitive to the assumed value of R than to the unsmearing uncertainties discussed in the previous section. From Table 5.4b it is observed, as is expected, that the value of xF_3 is insensitive to the choice of R.

5.3.3 A COMMENT ON NORMALIZATION OF STRUCTURE FUNCTIONS

The structure functions presented in section 5.2 have been extracted using a normalization resulting entirely from the present experimental run. By this it is meant that in calculating the flux integrals using equations (5.6) and (5.7), the values for the total

numbers of neutrinos and antineutrinos $N^{\nu,\bar{\nu}}$ are those that follow from the fitting of the observed muon fluxes in the shielding obtained from the Wide Band beam during the period of the experiment. The structure functions thus obtained are therefore consistent with, and effectively normalized to, the total cross section values which were calculated in the previous chapter. There is therefore a correlated systematic uncertainty in the magnitude of F_2 and xF_3 of order 7% resulting from the uncertainty in the flux measurement.

An alternative and equally reasonable approach to the normalization of the structure functions would follow from the observation made in section 4.4 that significantly more precise values of the total neutrino and antineutrino cross sections exist from the CDHS and CCFRR experiments performed using Narrow Band beams. Use of these cross sections rather than those obtained form the present experiment to normalize the structure functions would result in a smaller systematic uncertainty in the absolute magnitude of the structure functions, and would effectively raise all values of F_2 and xF_3 by the order of 10-13%. This reflects the higher values of the world averages for the total cross sections in comparison with those obtained for the present experiment.

Since the determination of F_2 and xF_3 results effectively from the sum and difference respectively of neutrino and antineutrino data, variations in the total cross section ratio $R^{\nu,\bar{\nu}} = \sigma^{\bar{\nu}}/\sigma^{\nu}$ will result in variations in the relative overall normalization of these structure functions. However, as the value of $R^{\nu,\bar{\nu}}$ obtained in Chapter 4 for the present experiment is consistent within statistical and systematic errors with the world averaged value, the relative normalization of F_2 and xF_3 would not be affected significantly if the procedure of normalizing to world averaged total cross sections was adopted.

For the remainder of the present work, F_2 and xF_3 will continue to be normalized, for internal consistency, to the total cross sections obtained for the present experiment. The above comments should nevertheless be borne in mind.

5.4 COMPARISONS WITH PREVIOUS MEASUREMENTS

Two previous measurements of the isoscalar structure functions F_2 and xF_3 using bubble chambers exposed to the CERN neutrino beams were mentioned in the introduction. The first [3] was a combination of low energy data from the Gargamelle bubble chamber filled with freon and exposed to the PS Wide Band beam, with data from an exposure of BEBC filled with a 74% mole Ne/H_2 mixture to the SPS Narrow Band beam. For the remainder of this thesis this measurement will be referred to as the WA47/GGM data. The second measurement [4] was from an exposure of the GARGAMELLE chamber filled with a propane/freon mixture to the SPS Wide Band beam. This measurement shall henceforth be referred to as the GGM/SPS data. Table 5.5 compares the event numbers contributing to these measurements with those of the present measurement.

A point to note immediately from Table 5.5 is that the nature of the targets differs between the various experiments, from a comparatively light propane mixture in the GGM/SPS experiment to the heavy iron target of the CDHS counter experiment. The WA47/GGM analysis combines data from two targets, with the neon–hydrogen mixture of the WA47 experiment extremely similar to the target of the present experiment. As has been mentioned previously in Chapter 1, current experimental evidence indicates an A dependence (A referring here to atomic weight) for structure functions [46], and so in principle we may expect differences in the isoscalar structure functions measured by the various experiments. Such effects are likely however to be small, and given the limitations in statistics of the bubble chamber experiments, are not likely to be significant at the level of present measurements. To look for such effects with any confidence by comparison of different experiments would require detailed step by step control of the systematics of the two experiments throughout the analysis chain used to calculate the structure functions, and should not be attempted simply from the published data. In the comparisons that follow below, it is assumed that to a good approximation the structure functions measured from the different targets are expected to be the same.

In order to compare the present measurements with those of the above experiments, it should at first be noted that different assumptions have been made in each case as to the

Table 5.5 : Comparison of Experiments

Experiment		Target	Energy Range (GeV)	Event Numbers	
				ν	$\overline{\nu}$
WA47/GGM	GGM/PS	CF_3Br	2–12	3000	2000
	WA47/SPS	73% mol. Ne/H_2	5–210	3100	1120
	Total			6100	3120
GGM/SPS		90% mol. C_3H_8 10% mol. CF_3Br	15–350	3000	3800
WA59		75% mol. Ne/H_2	10–300	5970*	9577*
CDHS		Fe	20–300	130000	180000

* If the full fiducial volume is considered, these event numbers become 8016 (ν) and 12853 ($\overline{\nu}$)

relationship between $2xF_1$ and F_2. The WA47/GGM measurement was made assuming $A = 2xF_1/F_2 = 1$, with the effect of reducing A to 0.8 indicated. For the GGM/SPS measurement a value of $A = 0.9$ was used, and for CDHS, $R = 0.1$. The sensitivity of the current measurement to assumptions about this relationship was investigated in the previous section, and the variation found to be small over the accessible region of the kinematic plane. Nevertheless, in the following comparisons a value of A appropriate to the data with which comparison is being made was used.

5.4.1 THE WA47/GGM EXPERIMENT

Firstly, the present F_2 and xF_3 measurements are compared with those obtained by the WA47/GGM experiment. Figs. 5.3a,b show a comparison of F_2 and xF_3 for the two experiments. For the present experiment, $A = 1$ has been used in extracting the structure functions for comparison in keeping with the WA47/GGM assumption. Errors displayed are statistical only.

The overall level of agreement between the values of F_2 for the two experiments is very good. At low x, $x < .1$, there is a tendency for F_2 as measured by WA47/GGM to lie systematically above F_2 measured by the present experiment for intermediate Q^2 ($1. < Q^2 < 16.$ GeV^2/c^2). The significance of the discrepancy is lessened by considering the systematic normalization uncertainties in the two experiments, although a shift due to normalization, if present, should be observable over the whole kinematic plane. No similar behaviour is observed for xF_3 in the lowest x bin. In the region $Q^2 > 2$ GeV^2/c^2, $x > .4$, it is also observed that the WA47/GGM F_2 values are high in comparison with those of the present experiment. The WA47/GGM points in this region comprise data predominantly from the lower neutrino energy GARGAMELLE exposure, and the statistical precision with which both F_2 and xF_3 is determined in this region is considerably better than for WA59. It has been remarked previously in connection with the present structure function measurements in this region that the systematic uncertainties are large and the determination of the structure functions somewhat unreliable as a consequence. This fact may well account for part or all of the discrepancy.

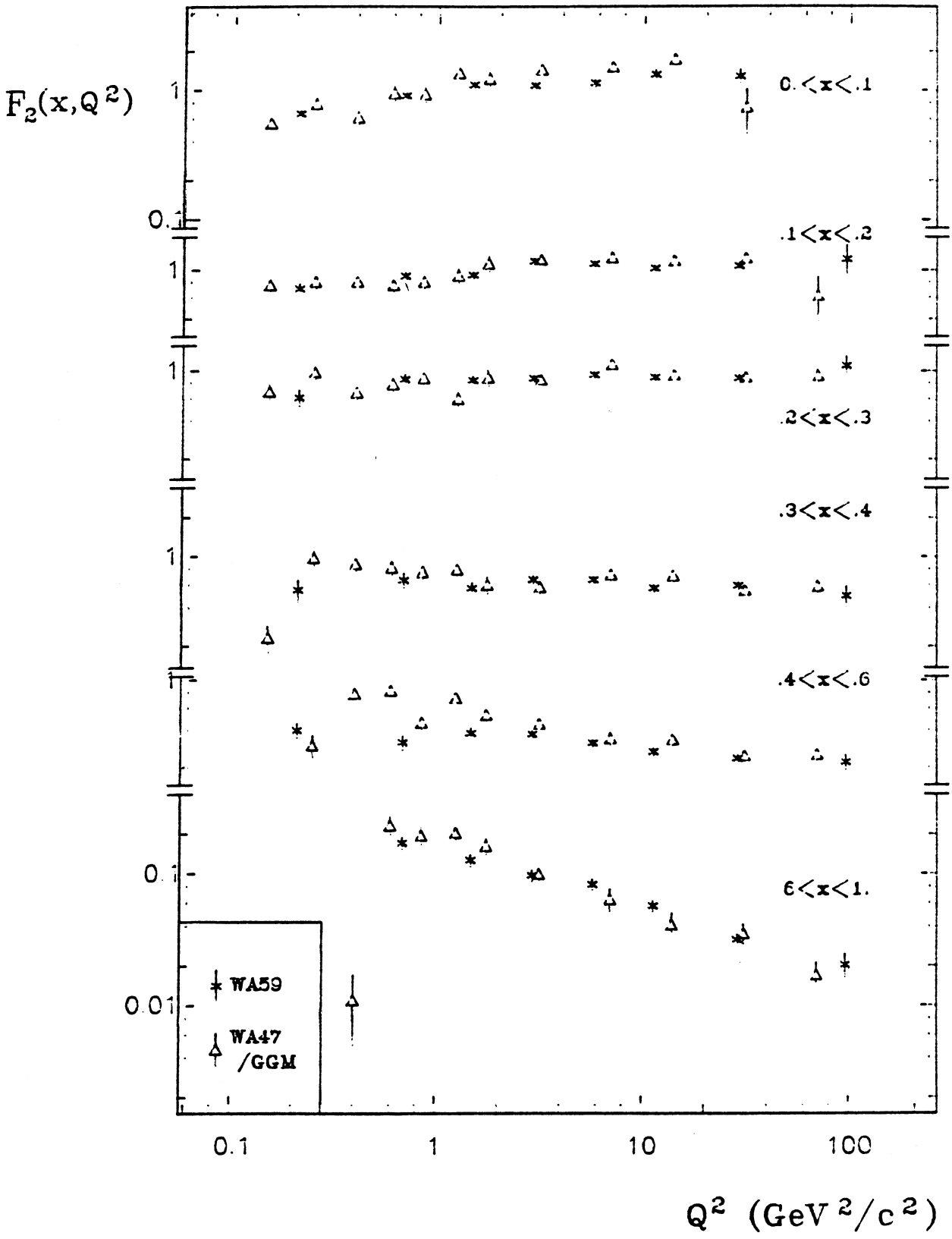

FIG 5.3a STRUCTURE FUNCTION $F_2(x,Q^2)$
COMPARISON OF WA59 AND WA47/GGM

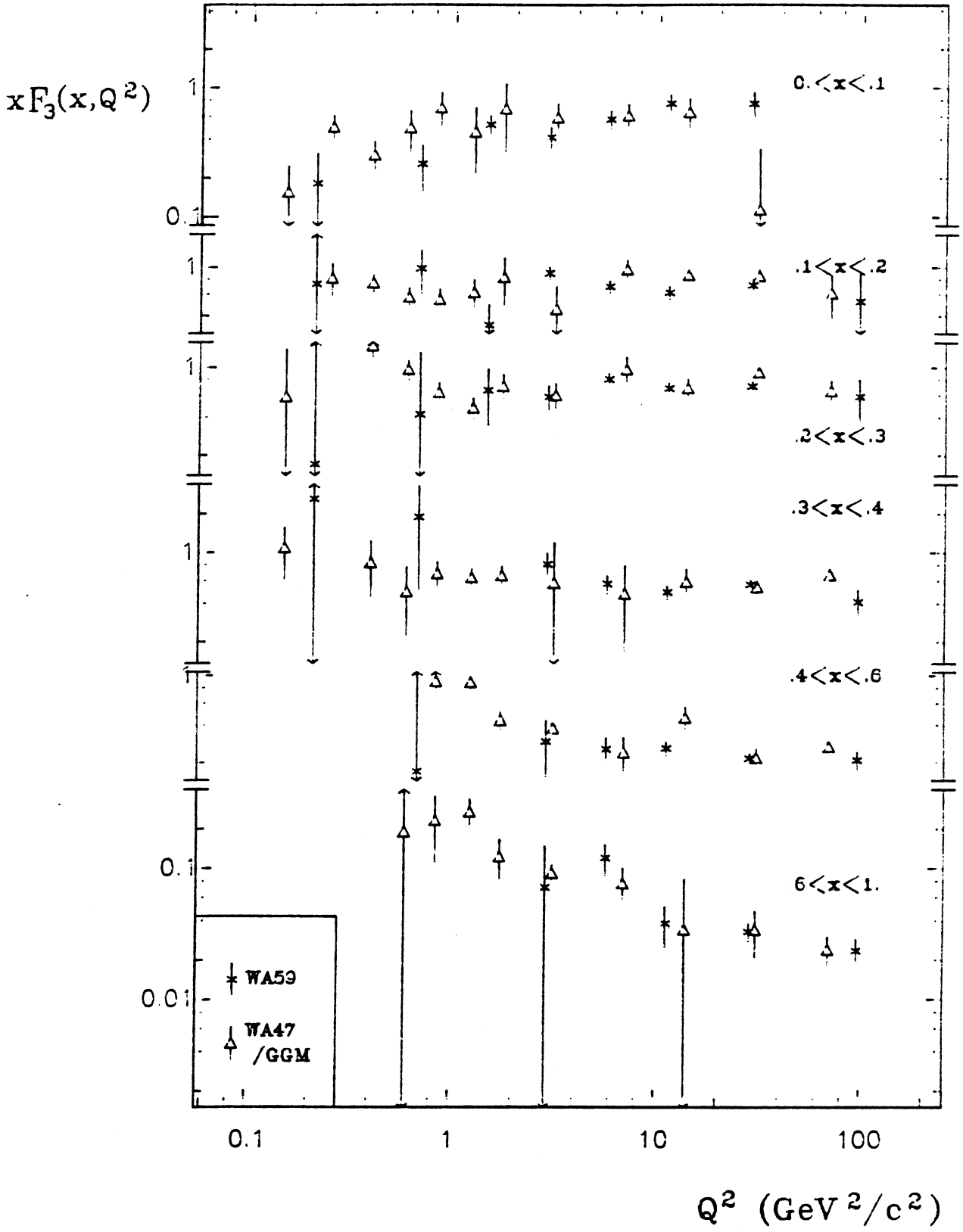

FIG 5.3b STRUCTURE FUNCTION $xF_3(x,Q^2)$
COMPARISON OF WA59 AND WA47/GGM

In comparing the measurements of xF_3 between the two experiments, we have a situation in which the statistical errors on the points are considerably larger for both experiments. Within these larger errors it would appear from Fig. 5.3b that the values of xF_3 obtained by the WA47/GGM experiment and the present one are consistent. xF_3 is determined with somewhat better statistical precision at high Q^2 by the present experiment, due mainly to a significantly larger antineutrino data set than that of the WA47 experiment (which contributes most of the high Q^2 data to the combined WA47/GGM analysis).

5.4.2 THE GGM/SPS EXPERIMENT

A comparison of F_2 and xF_3 with the GGM/SPS experiment is given in Figs. 5.4a,b. Note that in the GGM/SPS data the highest x bin for which structure functions are quoted extends from $x = 0.6$ to 0.8 only. In order to facilitate detailed comparison in this region with the present experiment, the structure functions were recalculated with data for $x > 0.8$ excluded. In the above figure the highest x bin plotted for the WA59 data is therefore $0.6 < x < 0.8$, corresponding to the binning of the GGM/SPS experiment. A value for A of 0.9 has been used.

The present experiment represents a distinct improvement in statistics in comparison with the GGM/SPS experiment. The published structure functions for GGM/SPS quote errors which have had a 10% systematic error added linearly to the statistical error. In order to present a more reasonable comparison of errors between the two experiments, this error has been removed from the structure function points displayed in Figs. 5.4a,b. A systematic error of similar magnitude exists for the present data, due to the flux uncertainties.

The general level of agreement between the two measurements appears to be good over the whole kinematic plane for both F_2 and xF_3. In the lowest x bin, $0. < x < 0.1$, there is some suggestion that the GGM/SPS data gives values for F_2 which are approximately 30-40% above those obtained from the present experiment. In view of the size of the systematic errors, which are not plotted, this discrepancy cannot be claimed to be significant,

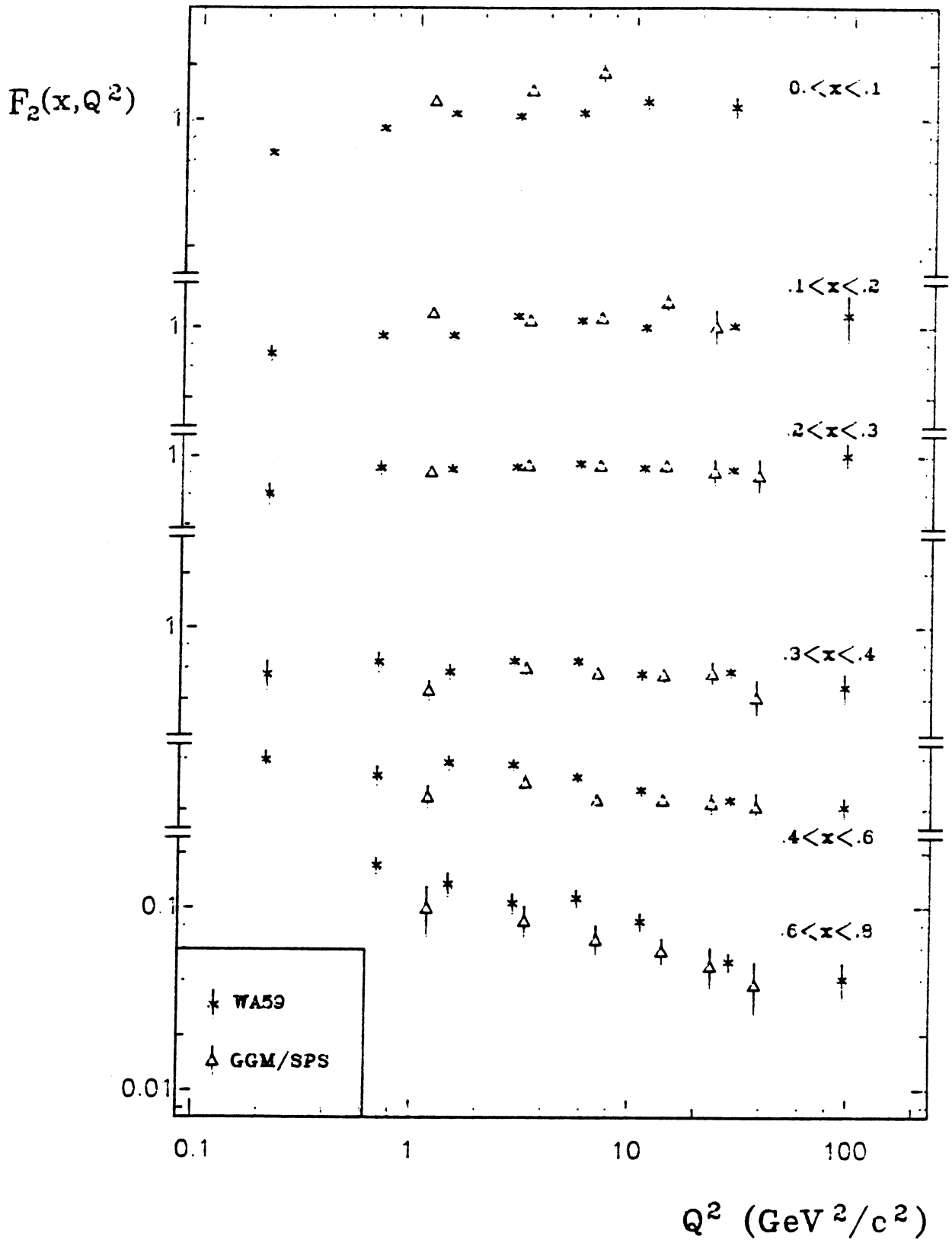

FIG 5.4a STRUCTURE FUNCTION $F_2(x,Q^2)$
COMPARISON OF WA59 AND GGM/SPS

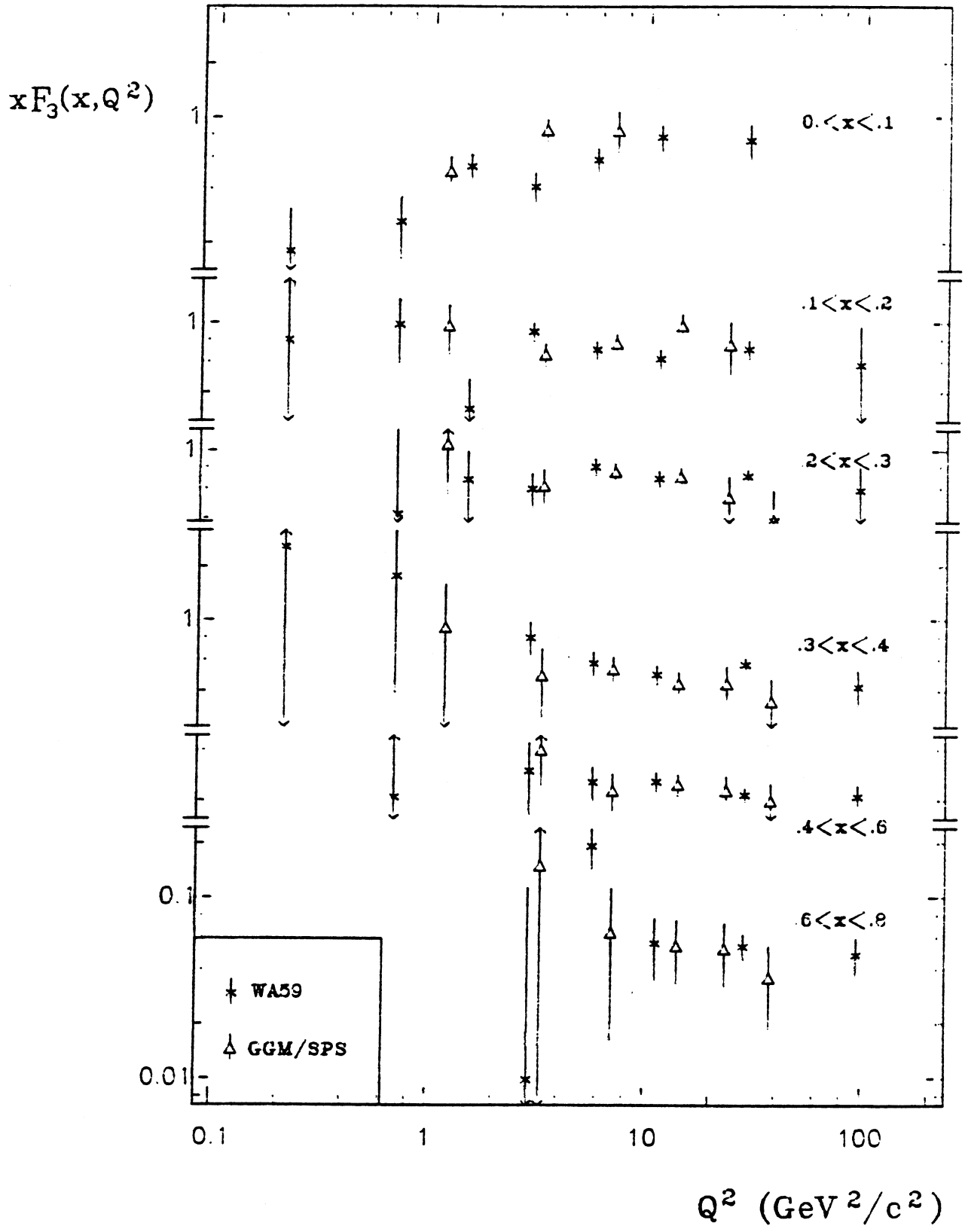

FIG 5.4b STRUCTURE FUNCTION $xF_3(x,Q^2)$
COMPARISON OF WA59 AND GGM/SPS

although a similar trend was observed in comparison with the WA47/GGM experiment. The general conclusion drawn from this comparison is that the two measurements of F_2 and xF_3 are consistent.

5.4.3 THE CDHS EXPERIMENT

In order to give an indication of how the structure functions obtained in this analysis compare with a typical neutrino counter experiment, an attempt is made at comparing with the published data on F_2 and xF_3 of the CDHS collaboration [5]. Neutrino counter experiments have a distinct advantage over bubble chamber experiments in terms of statistics, as a consequence of a much greater target mass. Weighed against this is the ability of the bubble chamber experiment to measure in kinematic regions of the $x-Q^2$ plane not accessible to the counter experiments, thus making the two types of experiment in some sense complimentary. This complimentarity is nowadays increased due to the differing nature of targets used in the two types of experiment, although as pointed out above, for the present naive comparisons it is assumed that all isoscalar targets are alike.

The CDHS collaboration have made very precise measurements of F_2 and xF_3 under the assumption that R =0.1. For purposes of comparison the present analysis was repeated under the same assumption, and in fact the values of the structure functions can be deduced from Tables 5.4a,b. It is difficult to conveniently compare the two sets of data, as the CDHS analysis is able due to statistics to bin more finely in x than is possible in the case of WA59. Nevertheless an attempt has been made to display the two sets of data on the same plot in Figs. 5.5a,b. Errors plotted for both experiments are statistical only. The bins $0.1 < x < 0.2$, $0.2 < x < 0.3$ and $0.3 < x < 0.4$ correspond almost exactly in terms of mean x to three of the bins used by CDHS, so here direct comparison can be made. If, as was done in the previous section for comparison with GGM/SPS, the structure functions are evaluated in the bin $0.6< x <0.8$, the mean x of this bin is 0.67, which is reasonably close to the mean of the highest CDHS bin. The highest x bin displayed for WA59 in Figs. 5.5a,b is therefore a bin from 0.6 to 0.8.

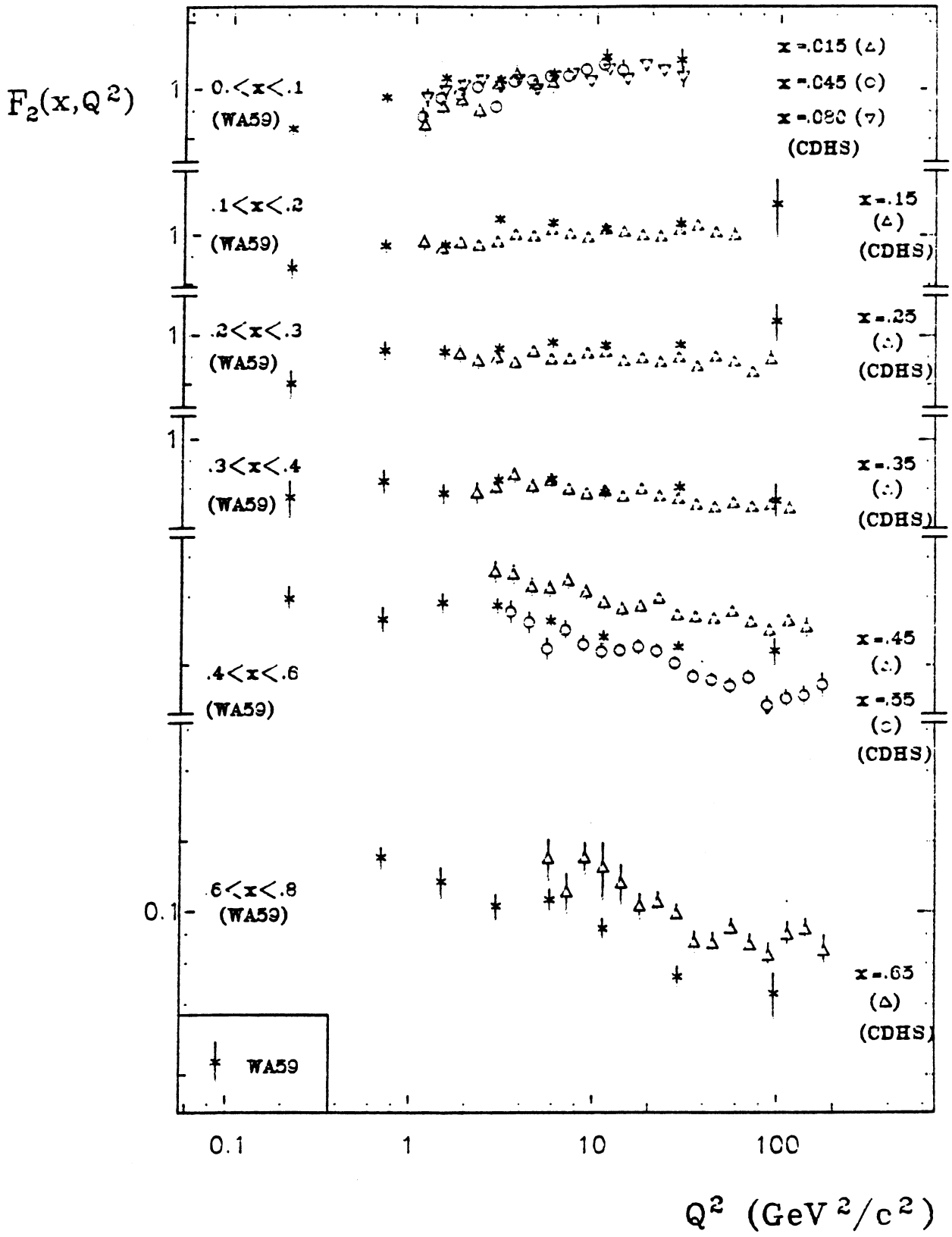

FIG 5.5a STRUCTURE FUNCTION $F_2(x,Q^2)$
COMPARISON OF WA59 AND CDHS

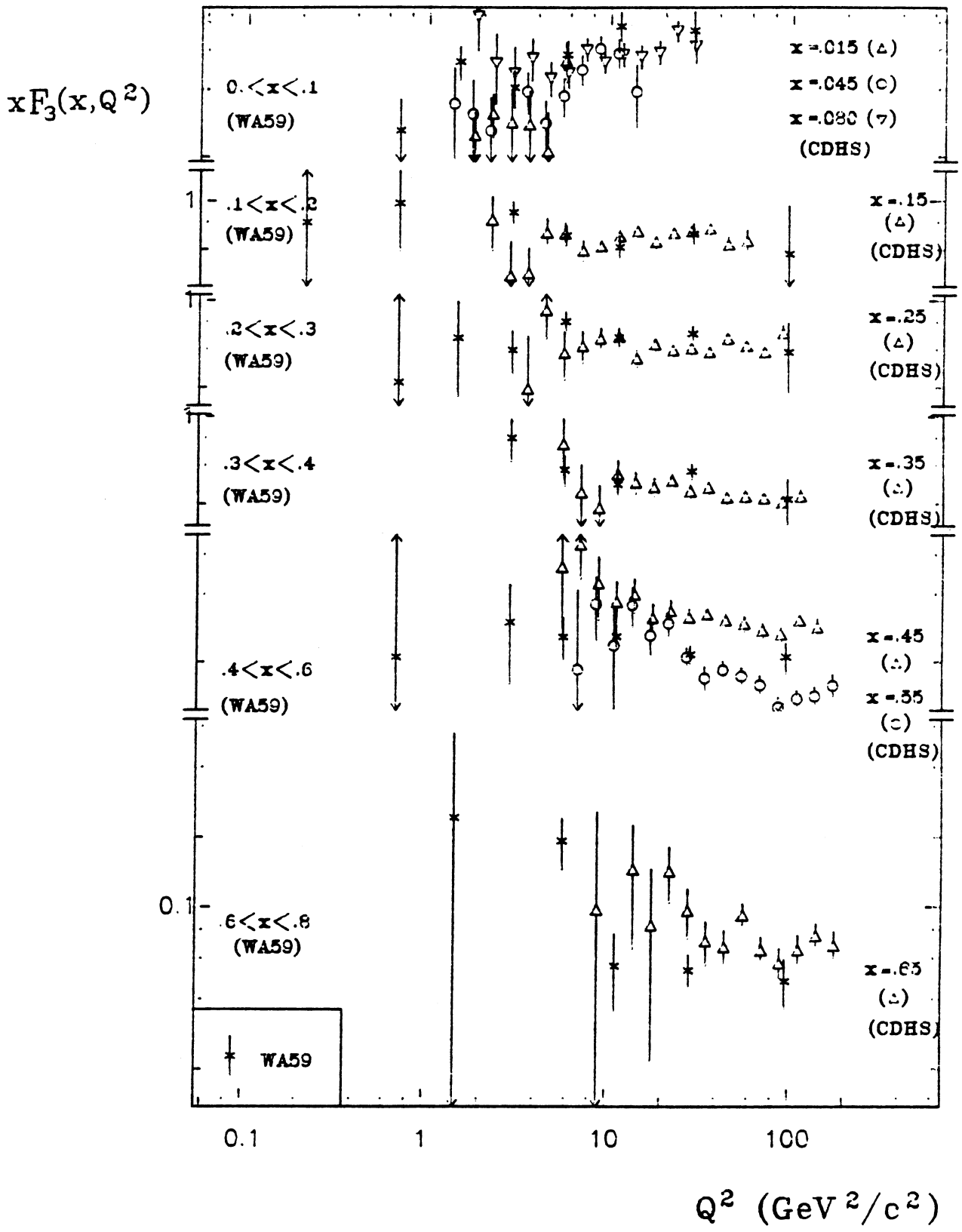

FIG 5.5b STRUCTURE FUNCTION $xF_3(x,Q^2)$
COMPARISON OF WA59 AND CDHS

Clearly due to the different binning any comparisons made here between the two experiments can only be qualitative. In the three bins with approximately equal mean x, agreement between the experiments appears to be obtained. The F_2 values of the present experiment in the bin $.4 < x < .6$, with mean 0.50, are qualitatively consistent with the CDHS values for $x = .45$ and $x = .55$. Overall a similar pattern of scaling violation to that observed by the CDHS collaboration is obtained for the present experiment.

Perhaps the most useful feature of Fig. 5.5 is to convey a visual impression of the differences remarked upon above in kinematic region covered and in statistics between counter and bubble chamber experiments.

Chapter 6

FURTHER ANALYSIS OF STRUCTURE FUNCTIONS

6.1 INTRODUCTION

In the previous chapter the extraction of the structure functions F_2 and xF_3 was described in some detail. In this chapter various topics related to these structure functions will be discussed. In section 6.2 the integrals over x of F_2 and xF_3 will be calculated and compared with those obtained from the total cross section measurements of Chapter 4. Quark and antiquark distributions will be extracted in section 6.3. Section 6.4 deals with the calculation of Cornwall-Norton and Nachtmann moments of F_2 and xF_3, for which QCD makes some predictions. Finally in section 6.5 some very preliminary remarks will be made on the use of the present measurements as a test of QCD.

6.2 STRUCTURE FUNCTION INTEGRALS

Using the notation introduced in equation (1.28), it can be seen that the integrals of F_2 and xF_3 over the range $0 < x < 1$ correspond to the second Cornwall–Norton moments of these structure functions

$$M_2^2(Q^2) = \int_0^1 F_2(x, Q^2)dx \tag{6.1}$$

$$M_3^2(Q^2) = \int_0^1 xF_3(x, Q^2)dx \tag{6.2}$$

In the limit of exact scaling, these integrals would be independent of Q^2. It has previously been noted in section 1.3 that within the framework of the quark-parton model, $\int_0^1 F_2(x)dx$ measures the fraction of the nucleon momentum carried by quarks and antiquarks. In the same scenario, $\int_0^1 xF_3(x)dx$ measures the fraction of the nucleon momentum carried by the valence quarks.

These integrals will now be evaluated as a function of Q^2 using the structure functions measured in Chapter 5. Since we have in effect measured structure functions bin averaged in Q^2, this will be done by summing over x bins i, for a fixed Q^2 bin j, the product of the structure function in that bin and the bin width, $\sum_i (F)_{ij}\Delta x_i$. Two practical difficulties arise in the calculation of this sum. The first concerns the highest Q^2 bin considered in this analysis, $64 < Q^2 < 200$ GeV^2/c^2, for which no data is available for x <.1 due to the finite neutrino energy range of the experiment. It is therefore not possible to evaluate the integral in this Q^2 bin. The second difficulty is one that is more evident at low Q^2, the inclusion of the elastic contribution to the integrals. This contribution is negligible for $Q^2 > 2$ GeV^2/c^2, but is sizeable at lower Q^2. It was seen in Chapter 5 that the elastic structure functions $F_2(Q^2)$ and $xF_3(Q^2)$ are poorly determined by the present data. The elastic contribution, which consists of a delta function at x =1, was therefore evaluated using the theoretically predicted [47] and experimentally verified [3] forms for the elastic structure functions

$$F_2(Q^2) = \frac{1}{2}\left\{\lambda^2 F_A(Q^2)^2 + \frac{(1+\beta^2 Q^2/4m^2)}{(1+Q^2/4m^2)} F_V(Q^2)^2\right\} \tag{6.3}$$

$$xF_3(Q^2) = \lambda\beta F_V(Q^2) F_A(Q^2) \tag{6.4}$$

where $F_V(Q^2)$ and $F_A(Q^2)$ are the dipole form factors

$$F_V(Q^2) = \frac{1}{\left(1+Q^2/{M_V}^2\right)^2} \tag{6.5}$$

$$F_A(Q^2) = \frac{1}{\left(1+Q^2/{M_A}^2\right)^2} \tag{6.6}$$

In these equations, $\lambda = 1.25$, $\beta = \mu_p - \mu_n + 1 = 4.71$, m is the nucleon mass, and M_V, M_A, which are not predicted theoretically, were taken to be .85 GeV/c^2 and .90 GeV/c^2 respectively.

Table 6.1 : Structure Function Integrals

$Q^2(GeV^2/c^2)$	$\int_0^1 F_2(x,Q^2)dx$	$\int_0^1 xF_3(x,Q^2)dx$	B
0.–.4	1.069±.018	1.419±.778	1.33±.73
.4–1.	.700±.016	.506±.337	.723±.482
1.–2.	.526±.013	.154±.127	.293±.242
2.–4.	.501±.011	.371±.048	.741±.097
4.–8.	.479±.010	.365±.023	.762±.051
8.–16.	.455±.013	.322±.018	.708±.048
16.–64.	.441±.017	.330±.020	.748±.054

Table 6.1 gives the values obtained for the integrals of F_2 and xF_3 as a function of Q^2, which are displayed graphically in Figs. 6.1a,b. The elastic contributions predicted by equations 6.3 and 6.4 are displayed in these figures also. Below $Q^2 \sim 2.$ GeV^2/c^2 it can be seen that the elastic contribution forms a significant fraction of the integrals. In the lowest Q^2 bin for xF_3 the elastic contribution exceeds the value quoted for the integral, due to the numerical value of xF_3 obtained at high x being negative. The large systematic uncertainties in extracting the structure functions in this region and the dominance of the elastic form factors precludes a reliable measurement of these integrals using the present data at low Q^2. For $Q^2 > 2.$ GeV^2/c^2, where the elastic contribution is small, the data is consistent with a slow falloff of both the integrals of F_2 and xF_3 with increasing Q^2. Such a falloff is predicted by QCD, due to an increasing fraction of the nucleon momentum being carried by gluons as Q^2 increases.

The above data on the structure function integrals should be compared with the values implied by the total cross section data of section 4.2, which were deduced assuming no Q^2 dependence for F_2 and xF_3. Considering the data for $\int_0^1 xF_3(x,Q^2)dx$, it would appear that a higher value for this quantity is implied by Table 6.1 than the value of .288 ± .008 given in Section 4.2 on the assumption of strict scaling.

To conclude this discussion, also presented in Table 6.1 and Fig. 6.1c is the ratio of the structure function integrals $B = \int_0^1 xF_3(x,Q^2)dx / \int_0^1 F_2(x,Q^2)dx$. The value quoted in

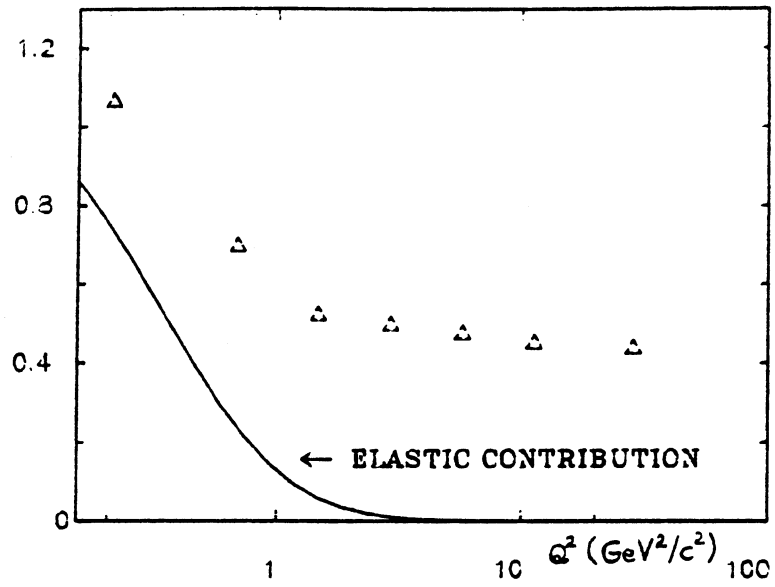

(a) $\int F_2(x,Q^2)dx$

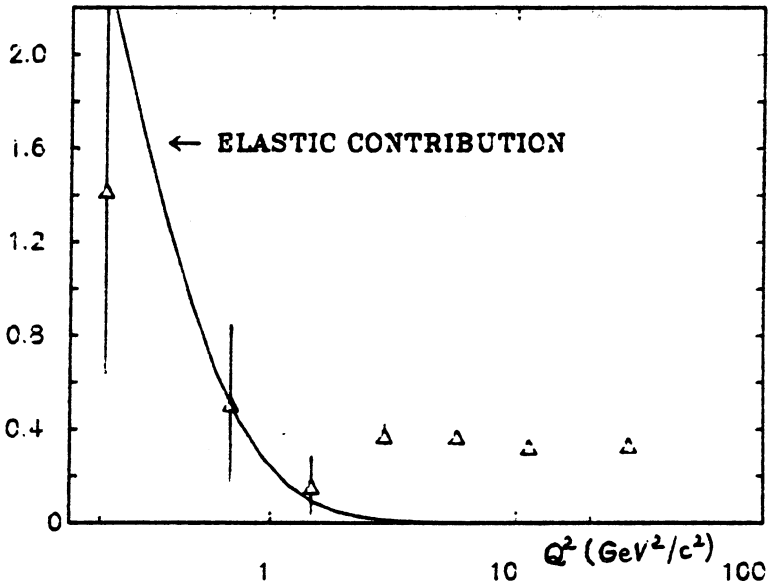

(b) $\int xF_3(x,Q^2)dx$

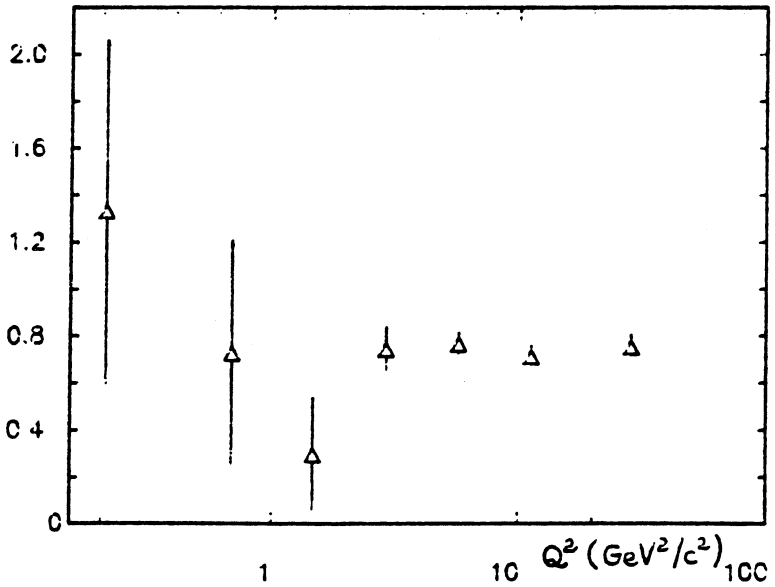

(c) $B = \int xF_3\,dx \;/\; \int F_2\,dx$

FIG 6.1 STRUCTURE FUNCTION INTEGRALS

section 4.2, once again using the total cross sections and assuming scaling, was $B = .660 \pm .019$. The data on B as a function of Q^2 suffers from large statistical uncertainties, but for $Q^2 > 2.$ GeV^2/c^2 would indicate a slightly higher value for B than that of Section 4.2, a refection of the higher value of the integral of xF_3 given above. The data cannot distinguish between a value of B flat in Q^2 in this region or slowly falling, the latter being predicted to be the case if more of the valence quark momentum at high Q^2 appears in quark-antiquark pairs as well as in gluons.

Measurements of the quantities discussed in this section, and indeed in the following sections, have been determined previously by the WA47/GGM experiment [3]. The results of the present measurements of $\int_0^1 F_2 dx$, $\int_0^1 xF_3 dx$ and B are broadly consistent with those obtained by the previous experiment. As in the case of the structure function xF_3 itself, the WA47/GGM experiment is better able to determine $\int_0^1 xF_3 dx$ (and hence B) at low Q^2 than is possible here.

6.3 QUARK AND ANTIQUARK DISTRIBUTIONS

The quark-parton model in relation to neutrino nucleon interactions was discussed in section 1.3. In particular, the differential cross sections for neutrino and antineutrino scattering from an isoscalar target were expressed in equation (1.25) in terms of the momentum distributions of quarks and antiquarks, $xq(x)$ and $x\bar{q}(x)$. If the strange and charmed quark momentum distributions in the sea are assumed to be identical ($s = c, \bar{s} = \bar{c}$), equation (1.25) becomes

$$\frac{d^2\sigma^{\nu}}{dxdy} = \frac{G^2 mE}{\pi}\left(\frac{{m_W}^2}{{m_W}^2 + Q^2}\right)^2 x\left\{q(x,Q^2) + (1-y)^2\bar{q}(x,Q^2)\right\} \tag{6.7}$$

$$\frac{d^2\sigma^{\bar{\nu}}}{dxdy} = \frac{G^2 mE}{\pi}\left(\frac{{m_W}^2}{{m_W}^2 + Q^2}\right)^2 x\left\{\bar{q}(x,Q^2) + (1-y)^2 q(x,Q^2)\right\} \tag{6.8}$$

where a possible dependence of q and $\bar{q}$ on Q^2 is indicated. These two equations were solved in bins of x and Q^2 for the distributions $xq(x,Q^2)$, $x\bar{q}(x,Q^2)$ in a manner entirely analogous to that used in Chapter 5 for extracting the structure functions F_2 and xF_3. In extracting these distributions, attention was limited to the region $Q^2 > 2$ GeV^2/c^2, where

non–perturbative higher twist effects are believed to be less important and quark–parton model ideas may be expected to approximately hold.

The results of this calculation of $xq(x,Q^2)$ and $x\bar{q}(x,Q^2)$ are displayed in Tables 6.2a,b. In Figure 6.2a–d the x distributions of xq and $x\bar{q}$ are given for the various Q^2 bins. The final Figure 6.2f and entry in the tables gives the above distributions averaged over the entire Q^2 region $Q^2 > 2.$ GeV^2/c^2.

The form of the distributions for xq and $x\bar{q}$ are qualitatively as expected from quark-parton model ideas. In particular it is noted that the contribution of antiquarks is negligible for $x >\sim .3$. If the integrals over x are formed for $Q^2 > 2.$ GeV^2/c^2, it is found that $\int_0^1 xqdx = .379\pm.015$, and $\int_0^1 x\bar{q}dx = .070\pm.009$, where the errors are statistical. The ratio $\int_0^1 x\bar{q}dx / \int_0^1 (xq + x\bar{q})dx$, giving the fraction of total quark momentum carried by anti-quarks, therefore has the value $.156\pm.022$. A previous measurement of this quantity by the WA47/GGM experiment [3], in the range $3. < Q^2 < 100.$ GeV^2/c^2, gave the value $.113\pm.030$, which is consistent with the present value.

6.4 MOMENTS OF THE STRUCTURE FUNCTIONS F_2 AND xF_3

Structure function moments were introduced briefly in Chapter 1. In attempts to test QCD predictions using lepton–nucleon scattering data, moments analyses have featured strongly [25] [48]. They have also been open to criticism [21] on the basis that few if any experimental data sets cover a sufficient x range to completely determine the moments, which theoretically are defined as integrals over the complete range $0 < x < 1$. The relative merits of the moments versus evolution equation techniques for confronting QCD, described in Section 1.4, have not been resolved to the satisfaction of everyone.

We here calculate the Cornwall-Norton and Nachtmann moments of F_2 and xF_3 as measured for the present data set.

Definitions for the Cornwall-Norton moments of a given structure function $F_i(x,Q^2)$

Table 6.2a : Quark Momentum Distribution $xq(x, Q^2)$

		Q^2 (GeV^2/c^2)					
		2.–4.	4.–8.	8.–16.	16.–64.	64.–200.	$Q^2 > 2GeV^2/c^2$
	0.–.1	0.746±0.058	0.850±0.067	1.032±0.101	1.010±0.146	–	0.836±0.032
	.1–.2	1.035±0.070	0.904±0.056	0.827±0.057	0.891±0.066	0.883±0.285	0.917±0.012
x	.2–.3	0.723±0.081	0.864±0.059	0.783±0.052	0.792±0.048	0.844±0.180	0.798±0.030
	.3–.4	0.733±0.104	0.612±0.058	0.528±0.043	0.573±0.036	0.458±0.086	0.580±0.010
	.4–.6	0.331±0.078	0.285±0.035	0.262±0.023	0.225±0.015	0.214±0.029	0.251±0.006
	.6–1.	0.085±0.041	0.100±0.018	0.046±0.008	0.032±0.004	0.022±0.005	0.040±0.000

Table 6.2b : Antiquark Momentum Distribution $x\bar{q}(x, Q^2)$

		Q^2 (GeV^2/c^2)					
		2.–4.	4.–8.	8.–16.	16.–64.	64.–200.	$Q^2 > 2GeV^2/c^2$
	0.–.1	0.332±0.029	0.280±0.031	0.280±0.042	0.262±0.050	–	0.302±0.019
	.1–.2	0.144±0.036	0.214±0.025	0.210±0.025	0.185±0.029	0.357±0.216	0.197±0.013
x	.2–.3	0.143±0.052	0.059±0.028	0.101±0.021	0.084±0.018	0.254±0.093	0.092±0.014
	.3–.4	-0.077±0.071	0.043±0.032	0.036±0.018	0.014±0.012	0.041±0.030	0.028±0.009
	.4–.6	0.036±0.062	0.027±0.022	0.002±0.010	0.009±0.005	0.005±0.008	0.024±0.005
	.6–1.	0.013±0.035	-0.019±0.013	0.009±0.005	-0.001±0.001	-0.002±0.001	0.007±0.001

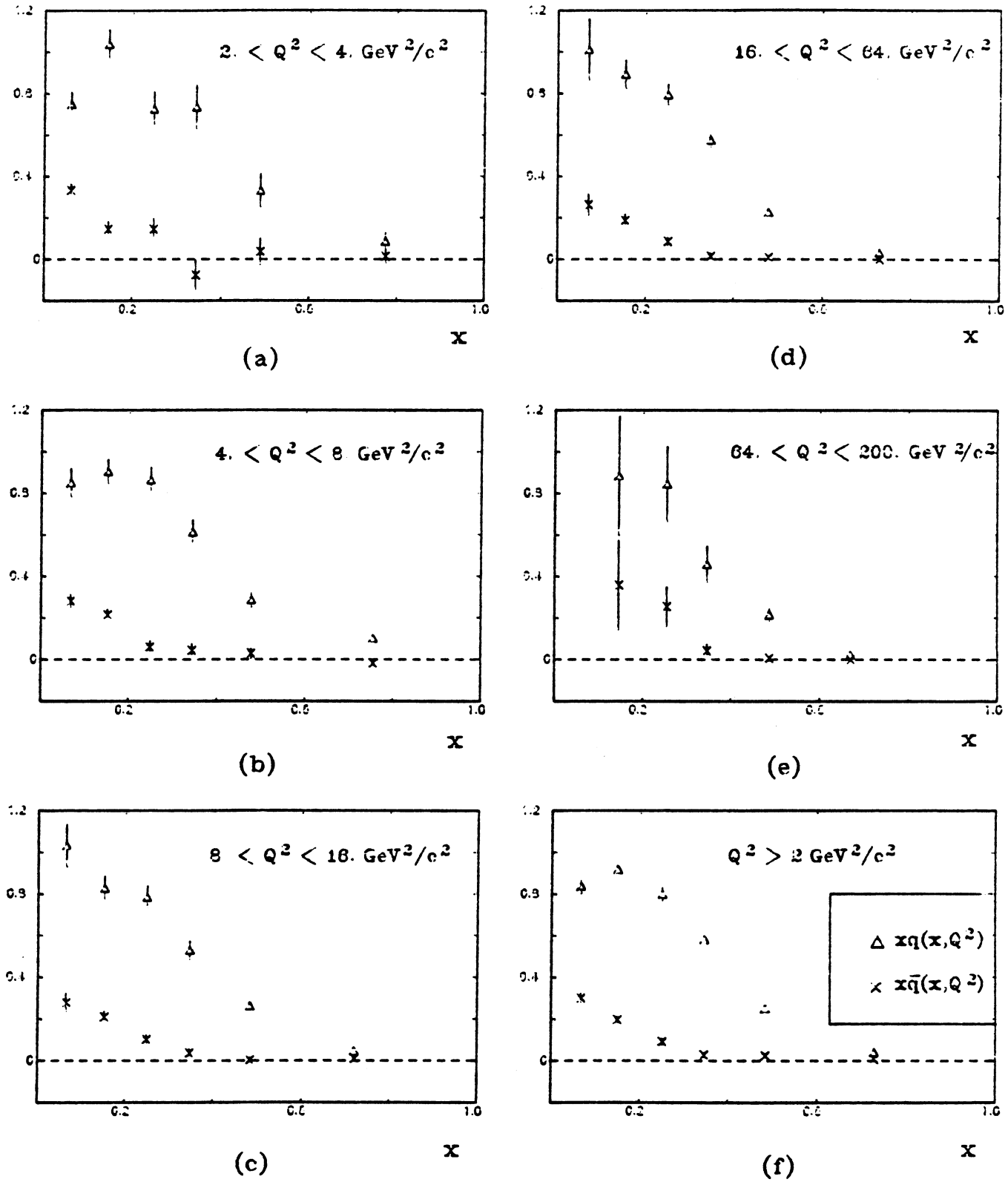

FIG 6.2 QUARK AND ANTIQUARK MOMENTUM DISTRIBUTIONS

have previously been given in equation (1.28), which is repeated here

$$M_i^n(Q^2) = \int_0^1 x^{n-2} F_i(x, Q^2) dx \qquad n = 2, 3, \ldots \tag{6.9}$$

The Nachtmann moments of F_2 and xF_3, which are preferred theoretically for correctly taking into account target mass effects (see Section 1.5), are given by the expressions

$$M_2^n(Q^2) = \int_0^1 \frac{\xi^{n+1}}{x^3} F_2(x, Q^2) \frac{(n^2+2n+3) + 3(n+1)\sqrt{1+4m^2x^2/Q^2} + n(n+2)4m^2x^2/Q^2}{(n+2)(n+3)} dx \tag{6.10}$$

$$M_3^n(Q^2) = \int_0^1 \frac{\xi^{n+1}}{x^3} xF_3(x, Q^2) \frac{1 + (n+1)\sqrt{1+4m^2x^2/Q^2}}{(n+2)} dx \tag{6.11}$$

where ξ has been defined previously by equation (1.32).

The second Cornwall-Norton moments of F_2 and xF_3 have already been encountered in section 6.2, where the structure function integrals were calculated. The higher moments are calculated here in an entirely analogous manner, by summing over x bins at a fixed Q^2 the product of the appropriate function of x and Q^2 evaluated at the mean x of the bin, the bin averaged structure function and the bin width. The elastic contribution at $x = 1$ is added to the sum using the theoretically predicted form for the appropriate structure function given by equations (6.3) to (6.6).

For the same reasons discussed in section 6.2 for the structure function integrals, the moments for $Q^2 < 2$ GeV^2/c^2 will not be considered. The systematic uncertainties at low Q^2 and high x which gave trouble for the $n = 2$ moments become even more important for higher moments, where the contribution from the high x region dominates the values of the moments as n increases.

In Figs. 6.3a,b the Cornwall–Norton moments of F_2 and xF_3 are plotted as a function of Q^2, for $n = 2$ to 10. The $n = 2$ moments are not given for the highest Q^2 bin due to a lack of data at low x. For higher moments the contribution from low x becomes small due to the presence of the x^{n-2} term, and moments can be calculated with small error despite the lack of data at low x.

The corresponding Nachtmann moments are plotted in Figs. 6.4a,b.

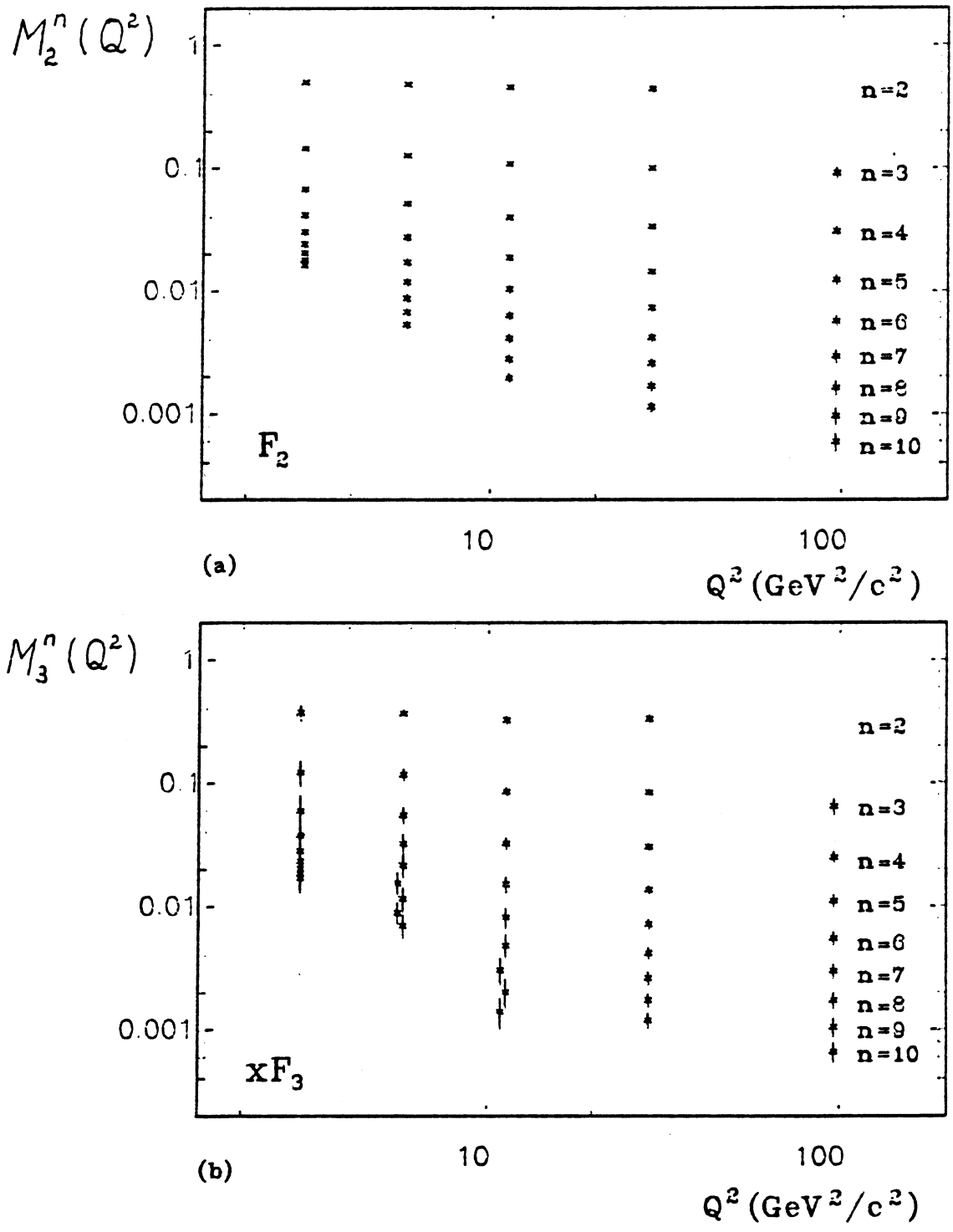

FIG 6.3 CORNWALL-NORTON MOMENTS

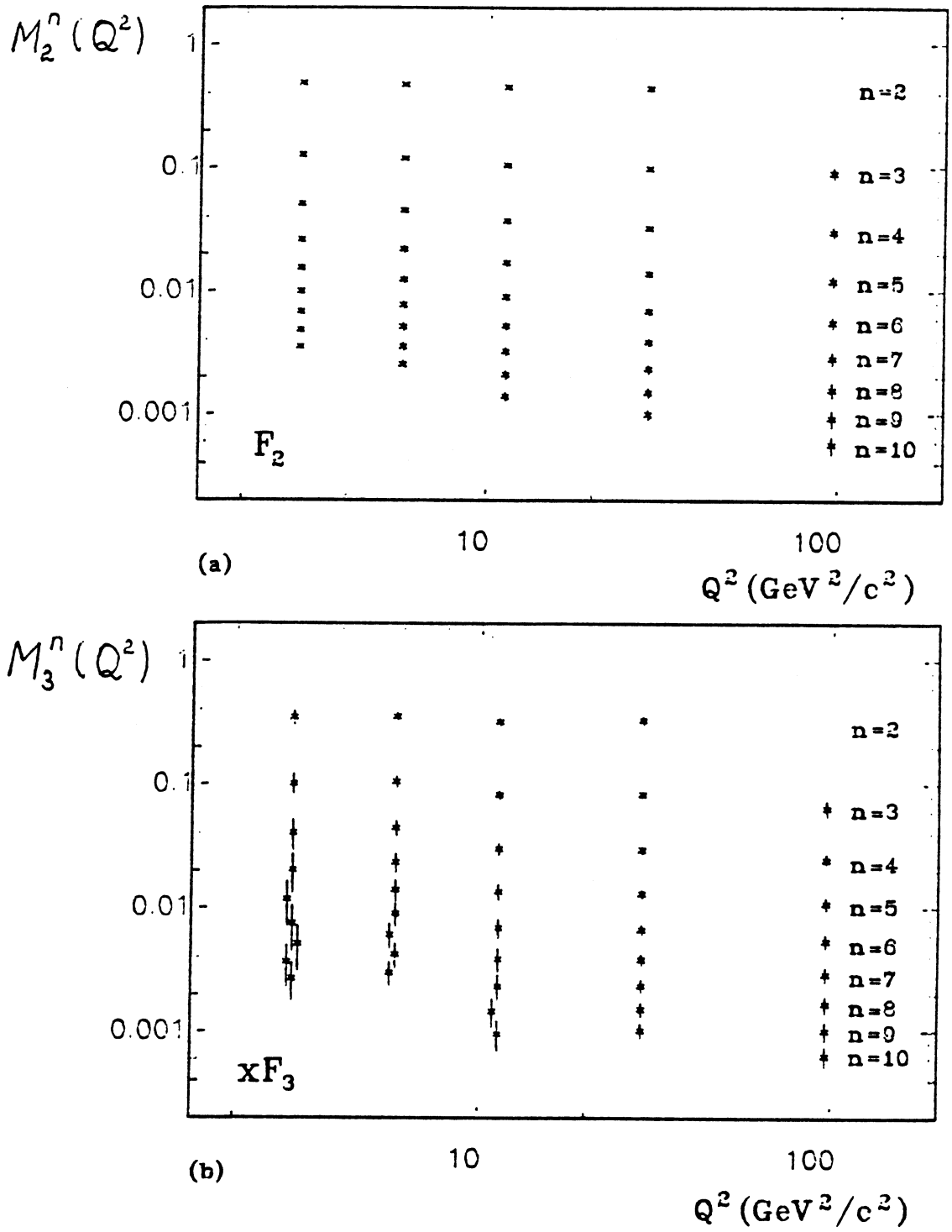

FIG 6.4 NACHTMANN MOMENTS

6.5 A PILOT STUDY FOR A DIRECT QCD ANALYSIS

In Chapter 1 a very brief discussion of the methods which have been used in an attempt to test the predictions of QCD with structure function data was given. Putting aside phenomenological fits of the Buras and Gaemers type, the two broad methods of attack are the moments analysis, referred to in the previous section, and what may be termed the "direct" or evolution equation approach. In this section the latter method is considered in relation to the present data. A full analysis of this type requires very detailed consideration of the systematics of the structure function measurement, and of other possible sources for any observed scaling violation. The results presented here represent a preliminary study of the present data on the assumption that the observed scaling violation is entirely due to perturbative QCD. Other explanations for the deviations from scaling are discussed in the following Chapter.

6.5.1 DESCRIPTION OF METHOD

The method employed here follows almost exactly that used in reference [49], and in fact makes use of a computer program developed for that analysis. What follows is a brief description of the method, and the reader is referred to [49] and references therein for more detail.

QCD predicts a definite form for the way in which scaling in neutrino–nucleon interactions is violated. As mentioned in section 1.4, the structure functions satisfy the integro–differential Altarelli–Parisi equations, given here for both F_2 and xF_3.

$$Q^2\frac{dF_2(x,Q^2)}{dQ^2} = \frac{\alpha_s(Q^2)}{2\pi}\int_x^1 \frac{x}{w^2}dw\left[F_2(w,Q^2)P_{qq}\left(\frac{x}{w}\right) + 2N_F G(x,Q^2)P_{Gq}\left(\frac{x}{w}\right)\right] \quad (6.12)$$

$$Q^2\frac{d\left(xF_3(x,Q^2)\right)}{dQ^2} = \frac{\alpha_s(Q^2)}{2\pi}\int_x^1 \frac{x}{w^2}dw w F_3(w,Q^2)P_{qq}\left(\frac{x}{w}\right) \quad (6.13)$$

P_{qq} and P_{Gq} are explicitly calculable in QCD. N_F is the number of active quark flavours, assumed to be 4, and $G(x,Q^2)$ the gluon structure function. $\alpha_s(Q^2)$ is the running coupling constant of QCD and must be calculated perturbatively in powers of $ln(Q^2/\Lambda^2)$. Λ is a free

parameter determining the size of the scaling violations, is dependent on the renormalization scheme under which calculations are performed, and must be determined from the data. It is a quantity which is canonically measured to be in the range 0 – 600 MeV/c.

Once $\alpha_s(Q^2)$ is calculated to a given order, equations (6.12) and (6.13) can be solved numerically in order to determine the appropriate structure function, provided a boundary condition is specified. Given a measured set of structure functions, the usual method adopted to determine whether the Q^2 dependence of the structure functions is consistent with the form predicted by (6.12) and (6.13), and to determine Λ, is the following. A functional form in x for the structure functions at some reference $Q^2 = Q_0^2$ is chosen (the boundary condition), and the integro–differential equations solved numerically and fitted to the measured structure functions in order to determine both the parameters specifying the chosen functions and Λ. It can be noted from the forms of (6.12) and (6.13) that this procedure is simplified in the case of the flavour non–singlet structure function xF_3 in comparison to that for the flavour singlet structure function F_2, as equation (6.12) involves also the gluon structure function $G(x, Q^2)$, which is not measured experimentally and for which some functional form must be chosen.

The analysis of reference [49] utilises the $\overline{MS}$ renormalization scheme and employs an expansion of $\alpha_s(Q^2)$ to second (or next to leading, NLO) order. The forms chosen for the structure functions at the reference Q_0^2 were

$$xF_3(x, Q_0^2) = Ax^{\alpha}(1-x)^{\beta}(1+\gamma x) \tag{6.14}$$

in the non–singlet case and

$$F_2(x, Q_0^2) = Ax^{\alpha}(1-x)^{\beta}(1+\gamma x) + A_s(1-x)^{n_s} \tag{6.15}$$

in the singlet case, with the gluon structure function given by

$$xG(x, Q_0^2) = A_G(1-x)^{n_G} \tag{6.16}$$

A is determined by the Gross–LLewellyn–Smith (GLS) sum rule, equation (1.27), and A_G by the Momentum Sum rule, $\int_0^1 \{F_2(x, Q^2) + G(x, Q^2)\}\, dx = 1$

Not all of the observed scaling violation is expected to be due to perturbative QCD, described by equations (6.12) and (6.13). In the regions of the kinematic $x - Q^2$ plane where the quantity $4m^2x^2/Q^2$ is non-negligible, non-perturbative target mass effects (a consequence of the finite non-zero nucleon mass), affect the pattern of Q^2 evolution of the structure functions. These effects are calculable, and corrected for in the analysis of reference [49] in the manner of reference [23].

6.5.2 NON-SINGLET FITS

The above method is now applied to the present data. Initially attention is restricted to the simpler case of the non–singlet structure function xF_3. A reference value of $Q_0^2 =$ 1 GeV^2/c^2 was chosen, and only data with $Q^2 >$ 2 GeV^2/c^2 considered, in order to select that region of the $x - Q^2$ plane most likely to be free of non–perturbative effects. The highest x bin used was from 0.6 to 0.8, leaving out the data at very high x for which the systematic uncertainties were believed to be large. These restrictions left a total of 29 data points. The parameter γ in the equation for $xF_3(x, Q_0^2)$ was fixed to be 0, and the GLS sum rule was not imposed, allowing A, α and β to be varied independently. A next to leading order fit was then performed to determine $\Lambda_{\overline{MS}}$, α, β and A', where A' is defined by (with γ =0 and B the Euler beta function)

$$A' = \frac{1}{3}\int_0^1 \frac{xF_3(x, Q_0^2)}{x} dx = \frac{1}{3} AB(\alpha, \beta + 1)$$

Thus the GLS sum rule would imply A' =1.

From the resulting fit a value for $\Lambda_{\overline{MS}}$ of 76 ± 106 MeV/c was obtained. Values for the other parameters were α =.943±.082, β =4.05±.43 and A' =.74±.10. The χ^2/NDF obtained was 1.42. A point should be made about the χ^2/NDF of this and subsequent fits. The errors used on the structure function points for the fits were statistical only, and did not take into account any systematic uncertainties which clearly must exist. A χ^2/NDF such as that obtained here is therefore not considered unreasonable.

It is noted from the value of A' obtained that the GLS sum rule does not appear to be satisfied. One possible explanation for this would lie in the systematic uncertainty in

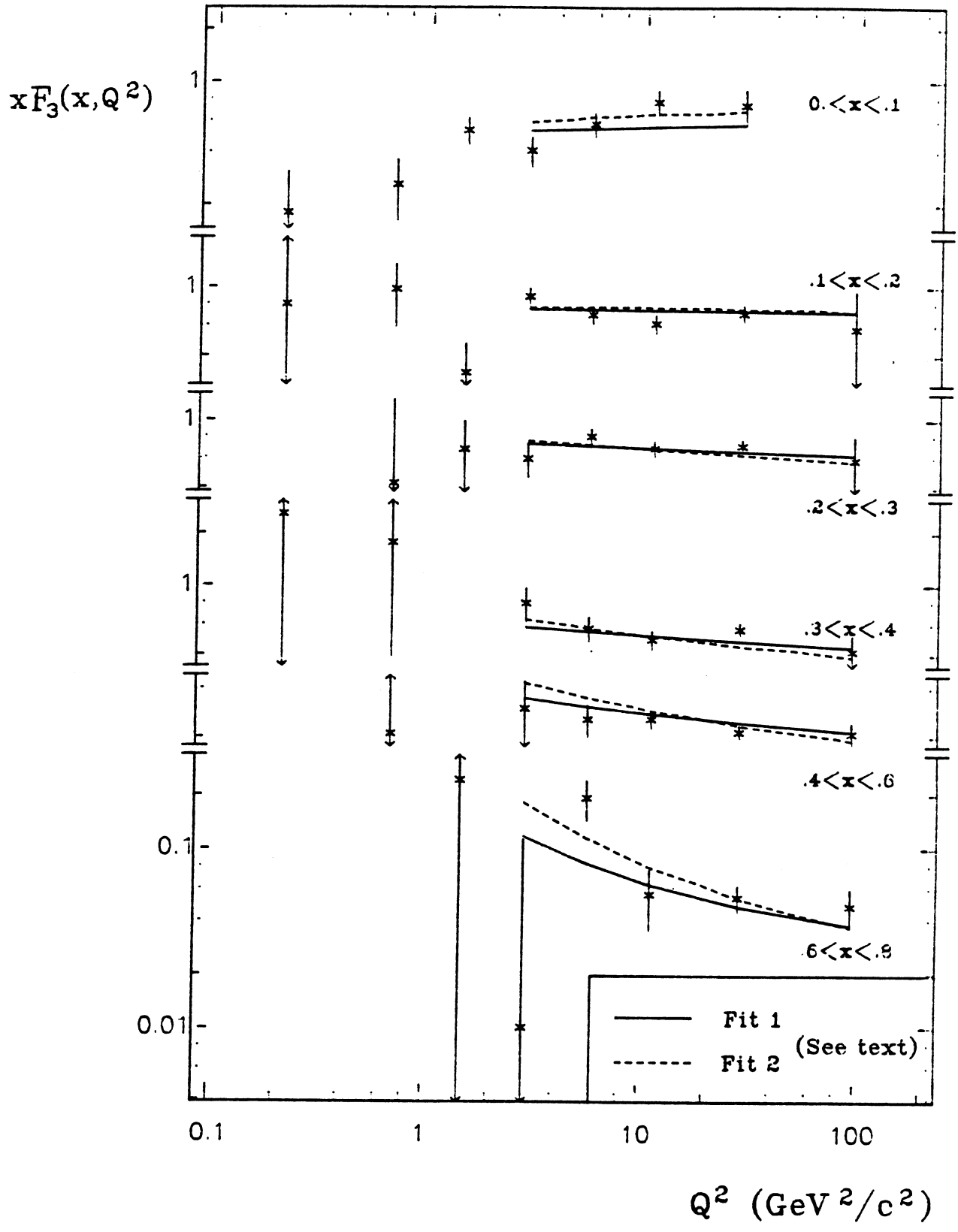

FIG 6.5 NON-SINGLET FITS TO $xF_3(x,Q^2)$

the normalization of the structure functions. To explore this further, the above fit was repeated with the GLS sum rule imposed by fixing A' =1. The results obtained were $\Lambda_{\overline{MS}}$ =484±58 MeV/c, α =.818±.117, and β =3.24±.48, with χ^2/NDF = 1.70. The value of $\Lambda_{\overline{MS}}$ from this and the previous fit appear discrepant. xF_3 is plotted with the two fits superimposed in Fig. 6.5. Whilst the χ^2/NDF for the second fit is worse than that of the first, it would appear on the basis of Fig. 6.5 that qualitatively both fits are equally reasonable representations of the data. This would lead to the conclusion that both a $\Lambda_{\overline{MS}}$ value of less than 100 MeV/c and one of ~ 500 MeV/c are capable of describing the data, and that this data is therefore not capable of constraining the value of $\Lambda_{\overline{MS}}$.

Before turning attention to the singlet fits to the structure functions, however, the question of normalization will be taken further. In section 5.3.3 it was remarked that normalization of the structure functions could equally well be carried out to the precise cross section measurements of, for example, the CDHS collaboration as to those obtained in the present experiment. The two sets of cross sections display some systematic differences in normalization, as was found in Chapter 4. F_2 and xF_3 were therefore recalculated normalized to the CDHS cross section measurements, and the above two fits repeated. With A' allowed to be free, it was found that $\Lambda_{\overline{MS}}$ =161±119 MeV/c, α =.938±.083, β =3.95±.42 and A' =.92±.13, with a χ^2/NDF of 1.43. Although larger by 85 MeV/c, this value for $\Lambda_{\overline{MS}}$ is compatable within errors with the value obtained in the first fit above. The value of A' is now found to be compatable with the GLS sum rule. When A' =1 was imposed on the fit, it was found that $\Lambda_{\overline{MS}}$ =274±75 MeV/c, α =.898±.098, and β =3.73±.39, for χ^2/NDF = 1.40. The discrepancy between the $\Lambda_{\overline{MS}}$ values for the second pair of fits is considerably less than that for the first pair, and they are compatable given the large errors. The value for $\Lambda_{\overline{MS}}$ for the final fit is not compatable with that of the second fit, for which A' =1 was also imposed.

Considering the above four fits as a whole, the following explanation for the large discrepancy in the values of $\Lambda_{\overline{MS}}$ between the first two fits is conjectured. Due to a substantial systematic error in the magnitude of the structure functions, and therefore in the magnitude of the integrals of the structure functions, strictly imposing the GLS

sum rule in fitting to the structure functions is unreasonable, and will distort the shape of the fitted structure function and therefore the observed degree of scaling violation. Since the shape and not the magnitude of the structure functions is of primary importance in determining the amount of scaling violation, the GLS sum rule should not be imposed on the fit but rather allowed to "absorb" the systematic uncertainty in overall magnitude of the structure functions. This possibility will be tested for the singlet fits below.

The results of the above four fits are summarised in Table 6.5.

6.5.3 SINGLET FITS

In the case of a singlet fit to the measured structure functions both F_2 and xF_3 data are used as well as both evolution equations (6.12) and (6.13). The number of parameters to be determined by the fit is now increased, and the added complication of the gluon structure function is present. To counter this, the better precision with which F_2 is determined may allow a better constraint on the value of $\Lambda_{\overline{MS}}$.

A next to leading order fit was performed to the combined F_2 and xF_3 data above $Q^2 =$ 2 GeV^2/c^2, a total of 58 data points. As in the non–singlet fits of the previous section, (and in fits which follow unless stated otherwise) Q_0^2 was set to 1 GeV^2/c^2, γ to 0 and target mass corrections were included. The parameter n_G specifying the hardness of the gluon distribution was set to 4. A' was allowed to be free. The resulting fit produced a value for $\Lambda_{\overline{MS}}$ of 92±51 MeV/c and A' =.79±.05, with χ^2/NDF = 1.47. The remaining parameters are given in the first entry (Fit 1) of Table 6.6. Both the value of $\Lambda_{\overline{MS}}$ and that of A' are consistent with those obtained by Fit 1 in the non–singlet case, and the nominal errors have halved in magnitude.

In the spirit of the previous section the fit was repeated with A' fixed to the value 1. In this case (Fit 2) it was found that $\Lambda_{\overline{MS}}$ =130±54 MeV/c, with χ^2/NDF = 1.68. Fits 1 and 2 are displayed in Figs. 6.6a,b. The dramatic rise in $\Lambda_{\overline{MS}}$ observed in the non–singlet case is not observed here, and although a higher value is obtained, it remains consistent within errors with the value obtained by Fit 1. The value of $\Lambda_{\overline{MS}}$ therefore

Table 6.3 : Summary of Non-Singlet Fits to Structure Functions

Fit	$\Lambda(MeV/c)$	α	β	A'	χ^2/DF	Description
1	76±106	.943±.082	4.05±.43	.74±.10	1.42	A' free
2	484±58	.818±.117	3.24±.48	1	1.70	A' fixed
3	161±119	.938±.083	3.95±.42	.92±.13	1.43	A' free, CDHS normalization
4	274±75	.898±.098	3.73±.39	1	1.40	A' fixed, CDHS normalization

Unless otherwise stated, all fits are NLO fits to xF_3, with $Q_0^2 = 1GeV^2/c^2$,
A' free, and Target mass corrections.

Table 6.4 : Summary of Singlet Fits to Structure Functions

Fit	$\Lambda(MeV/c)$	α	β	A'	A_s	n_s	χ^2/DF	Description
1	92±51	.882±.076	3.95±.14	.79±.05	.592±.109	4.50±.88	1.47	A' free
2	130±54	.697±.114	3.68±.11	1	.373±.069	3.49±.79	1.68	A' fixed
3	96±51	.858±.077	3.94±.15	.95±.06	.648±.134	4.96±1.12	1.46	A' free, CDHS normalization
4	107±51	.818±.044	3.87±.11	1	.593±.092	4.86±1.07	1.45	A' fixed, CDHS normalization
5	155±57	.823±.074	3.68±.13	.84±.06	.559±.111	4.36±.93	1.80	No target mass corrections
6	90±51	.904±.084	3.59±.15	.71±.05	.517±.111	4.28±.95	1.42	Leading order fit
7	73±48	.877±.077	3.95±.15	.78±.05	.670±.106	4.42±.74	1.50	$R = 0.1$
8	101±50	1.02±.07	4.17±.15	.72±.04	.384±.081	3.34±.78	2.06	Radiative Corrections
9	147±84	.773±.084	3.88±.16	.86±.08	.653±.143	4.88±1.01	1.49	$Q^2 > 4GeV^2/c^2$, $Q_0^2 > 2GeV^2/c^2$
10	74±47	.877±.076	3.97±.14	.78±.05	.656±.108	4.59±.82	1.49	$n_G = 8$ (softer gluons)
11	400	.970±.083	3.77±.15	.87±.05	.428±.132	4.41±1.53	2.03	Λ fixed

Unless otherwise stated, all fits are NLO fits to F_2 andxF_3, with $Q_0^2 = 1GeV^2/c^2$, $n_G = 4$,
A' free, and Target mass corrections.

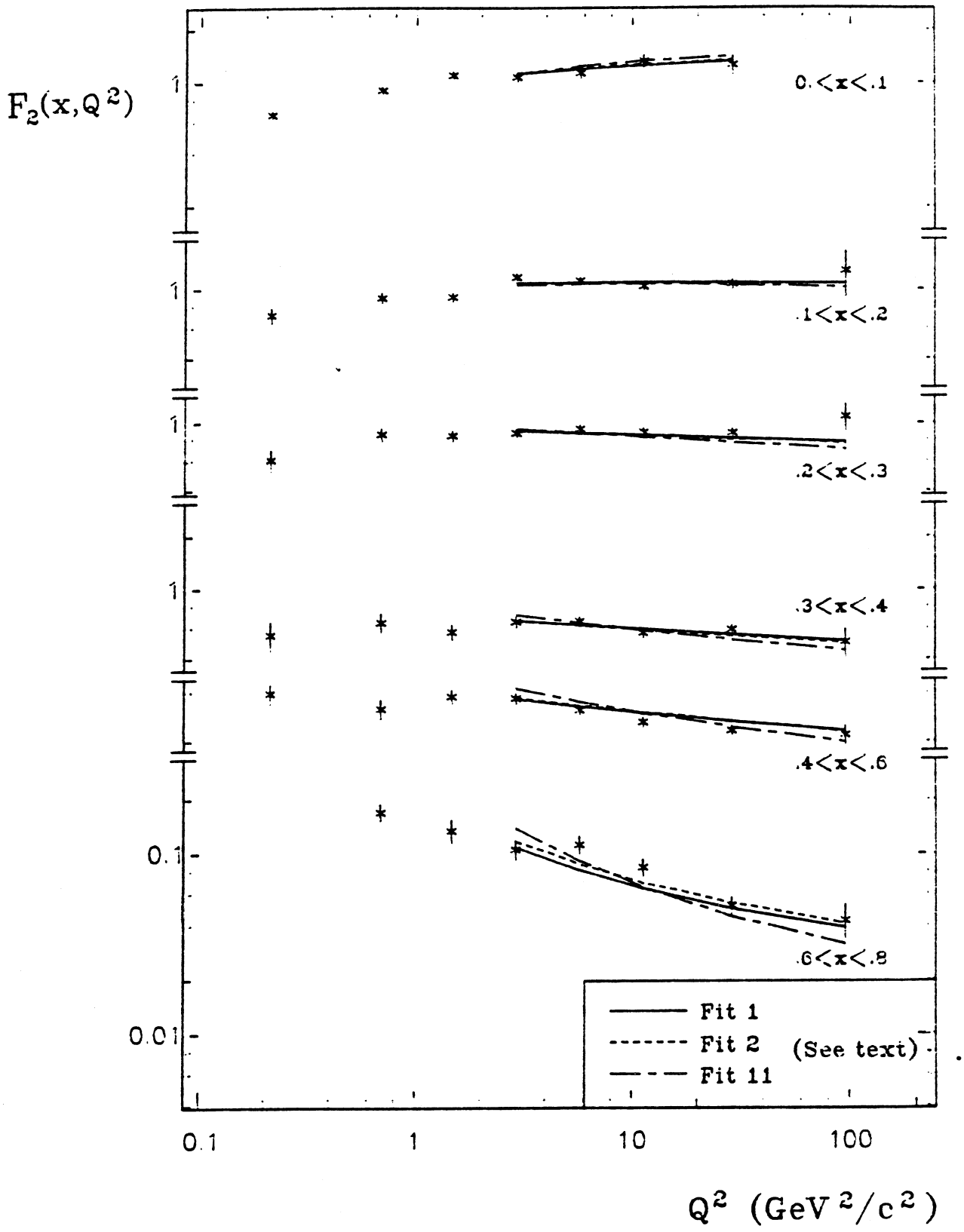

FIG 6.6a SINGLET FITS TO $F_2(x,Q^2)$ AND $xF_3(x,Q^2)$

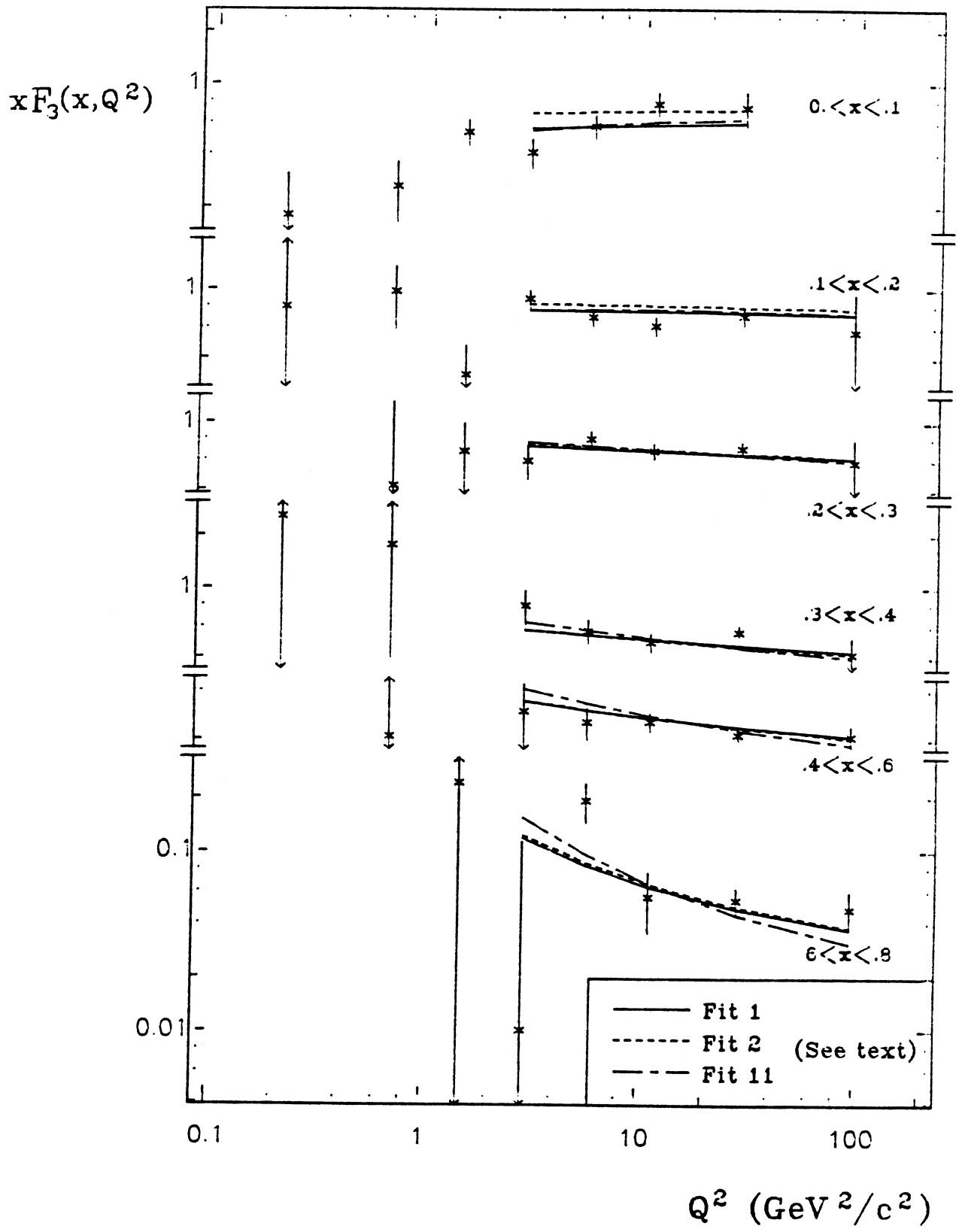

FIG 6.6b SINGLET FITS TO $F_2(x,Q^2)$ AND $xF_3(x,Q^2)$

appears to be less sensitive to the overall normalization than in the nonsinglet case. To confirm this, the above two fits were performed to the structure functions calculated with normalization fixed by the CDHS cross sections. With A' free (Fit 3), it was found that $\Lambda_{\overline{MS}}$ =96±51 MeV/c and A' =.95±.06 (χ^2/NDF = 1.46), and with A' =1 (Fit 4) a value for $\Lambda_{\overline{MS}}$ of 107±51 was obtained (χ^2/NDF = 1.45). All four fits are consistent with respect to the value of $\Lambda_{\overline{MS}}$ produced. Whilst the trends induced in the non–singlet case by normalization uncertainties are present here, they occur at a much less significant level, and a stable value of $\Lambda_{\overline{MS}}$ is produced.

The effect of target mass corrections on the singlet fit was investigated by repeating Fit 1 with these corrections excluded. The value of $\Lambda_{\overline{MS}}$ obtained was somewhat higher, $\Lambda_{\overline{MS}}$ =155±57 MeV/c, and the quality of the fit somewhat poorer with χ^2/NDF = 1.80. This is Fit 5 in Table 6.6. A degree of sensitivity to these corrections is a reflection of the size of the quantity $4m^2x^2/Q^2$, which governs differences between x and the Nachtmann variable ξ in the kinematic region under consideration.

Fit 6 in Table 6.6 is the result of a leading order (LO) singlet fit to F_2 and xF_3, producing Λ_{LO} =90±51 MeV/c with χ^2/NDF = 1.42. As shown originally in [50], the leading order value of Λ is subject to an ambiguity in definition and is not a useful quantity for comparison between different physical processes. Here it agrees very closely with the next to leading order value. For the remainder of this section we continue with next to leading order fits.

Sensitivity of the fit to assumptions as to the value of $R = \sigma_s/\sigma_T$ was investigated by fitting to the structure functions recalculated using a value of R = 0.1 (Fit 7). This resulted in a value for $\Lambda_{\overline{MS}}$ of 73±48 MeV/c with χ^2/NDF = 1.50, which is completely consistent with the value obtained assuming R = 0.0.

As a result of the analysis of Chapter 5 of systematic uncertainties in the structure function measurements, the effect which would appear to have potentially the most effect on fits to structure functions above Q^2 = 2 GeV^2/c^2 is that of radiative corrections. Inclusion of this correction produced significant corrections to the values of the structure

functions at low x and high Q^2. A fit was therefore performed to F_2 and xF_3 with this correction applied (Fit 8). A significantly poorer χ^2/NDF of 2.06 was obtained due to the inability of the fit to follow the decrease in F_2 and xF_3 induced at low x and high Q^2 by the radiative corrections. The value of $\Lambda_{\overline{MS}}$ obtained was 101±50 MeV/c, which remains consistent with the value obtained in Fit 1 with no radiative corrections.

All fits presented above have been made to data with $Q^2 > 2$ GeV^2/c^2 and $Q_0^2 = 1$ GeV^2/c^2. To investigate the effect of varying this cut a fit was performed only including data with $Q^2 > 4$ GeV^2/c^2 and $Q_0^2 = 2$ GeV^2/c^2. This would be expected to reduce the effect of any higher twist or target mass corrections to the structure function evolution. With this more stringent cut imposed a total of 46 data points remain. A value of $\Lambda_{\overline{MS}}$ =147±84 MeV/c resulted, with χ^2/NDF = 1.49. This represents an increase of 55 MeV/c in the value of $\Lambda_{\overline{MS}}$ over that obtained with a Q^2 cut of 2 GeV^2/c^2, but remains consistent with that value.

In reference [49] it is noted that in performing singlet fits to structure functions there is a strong correlation between the magnitude of $\Lambda_{\overline{MS}}$ and the hardness of the gluon distribution assumed in the fit. As mentioned at the beginning of this section, a value of n_G =4 has been used in all singlet fits to date. To test for sensitivity of $\Lambda_{\overline{MS}}$ to the gluon distribution, a softer distribution was assumed by setting n_G =8 and Fit 1 repeated. As predicted by reference [49], a smaller value of $\Lambda_{\overline{MS}}$ of 74±47 MeV/c (χ^2/NDF = 1.49) was obtained corresponding to the softer gluon distribution. The decrease, however, is not significant.

Finally in this section on singlet fits, the question raised in the non–singlet case regarding the ability of the data to distinguish between low (~100 MeV/c) and high (~400 – 500 MeV/c) values of $\Lambda_{\overline{MS}}$ is considered. It can be seen from inspection of Table 6.6 that all fits discussed above have produced a value for $\Lambda_{\overline{MS}}$ lying in the range 60 – 160 MeV/c. Fit 1 of this table typifies these fits, with a value of $\Lambda_{\overline{MS}}$ of 92±51 MeV/c. This fit was repeated fixing the value of $\Lambda_{\overline{MS}}$ to be 400 MeV/c. The χ^2/NDF obtained (Fit 11 of Table 6.6) was considerably poorer at 2.06. The fit is compared with that produced

by Fit 1 with $\Lambda_{\overline{MS}}$ free in Figs. 6.7a,b. Qualitatively the fit with $\Lambda_{\overline{MS}} = 400$ MeV/c does not represent the data as well as fits producing a lower value. However it is difficult to exclude the higher value for $\Lambda_{\overline{MS}}$ on the basis of this fit alone.

6.5.4 CONCLUSIONS

The above discussion has presented many fits to the structure functions F_2 and xF_3. We here attempt to summarise the results of the study and draw conclusions regarding a direct analysis of the present data in terms of QCD.

In the case of non–singlet fits to xF_3 alone, qualitative agreement is observed with the form of scaling violation predicted by QCD. The data does not appear to have the statistical precision necessary to allow constraints on the value of $\Lambda_{\overline{MS}}$ to be established with any reliability. Both values of order 100 MeV/c and of order 400 MeV/c for $\Lambda_{\overline{MS}}$ are consistent with the xF_3 data. The value of this quantity obtained from non–singlet fits appears sensitive to the overall normalization uncertainties present in the determination of xF_3.

Singlet fits to the combined F_2 and xF_3 data are also broadly compatable with the QCD form for scaling violation, and allow more scope for constraining the value of $\Lambda_{\overline{MS}}$. The magnitude of the scaling violation appears to favour a value for $\Lambda_{\overline{MS}}$ of the order of 100 MeV/c, although higher values are not ruled out at this stage. Leading order and next to leading order values for Λ agree within errors. Within the degree of precision with which $\Lambda_{\overline{MS}}$ can be determined, there seems to be no strong dependence on target mass corrections, normalization uncertainties of structure functions, or assumptions concerning R. The inclusion of radiative corrections to the structure functions produces problems in fitting the Q^2 evolution which require further investigation. The exact shape of the gluon distribution does not strongly influence the value of $\Lambda_{\overline{MS}}$. This last point can be restated in the form that the present data is unable to distinguish between a hard and soft gluon distribution.

The above discussion would indicate that there is potential for studying QCD using the present data. However a more detailed investigation of systematic uncertainties than has been made in this preliminary study is required. This is particularly true if the higher x data is to be included, for which systematic uncertainties are large. A study confronting QCD must also address the question of whether the observed form of scaling violation can be explained by other means, such as higher twist. This has been ignored in the above study. The problems involved in looking for higher twist effects in the present structure function data will be discussed in a little more detail in the following Chapter.

Chapter 7

DISCUSSION

In some respects the analysis which has been presented in this thesis must be termed a progress report. The primary motivation for measuring structure functions in deep inelastic neutrino nucleon scattering, as was stressed at the beginning, is to study the structure of the nucleon, and, in the course of this study, to determine to what extent the theory of Quantum Chromodynamics, which describes the dynamics of the strong interaction, is able to describe the structure observed. We are faced with a two step problem, the purely experimental question of measuring the structure functions as reliably as possible within the constraints of the experiment, and the interpretation of these structure functions once measured. This thesis has primarily addressed the first step, and touched only briefly on the second. The purpose of this Chapter is to indicate firstly ways in which the analysis presented here may be extended and improved, and secondly to explore what lies ahead in the interpretation of the measured structure functions.

In terms of the present analysis, we first return to the data set itself. One of the primary problems with locating events by visual scanning of bubble chamber film is that the scanning efficiency for this process is topology dependent, and in order to prevent the introduction of biases in the inclusive distributions which we would like to study, the scanning efficiency must be reliably determined. This has been achieved in the case of the present experiment, but only within a reduced "sector scan" fiducial volume. Approximately 25% of the total number of scanned and measured events from this experiment are

excluded from the present analysis because they lie outside the sector scan volume and therefore have unreliably determined scanning efficiencies. A detailed comparison of the properties of events within and without the sector scan volume may indicate how these events can be included without bias, thus increasing the statistics. In similar vein, the requirement that only events be used which occurred during periods of stable flux conditions removes a further percentage of the total event sample, particularly in the case of the neutrino sample which is already statistically inferior to the antineutrino sample. Comparison of the properties of the "good flux" and "bad flux" samples may allow these to be combined with another gain in statistics. Finally, this event hunting expedition may extend to the inclusion of the antineutrino data of the three laboratories with problems with event rates and scanning efficiencies, although how to proceed in this case is less than clear. It should perhaps be added that the gain in statistics that would result from the above improvements is unlikely to significantly enhance the power of the larger data set to make statements concerning QCD above that of the data set used here.

We now turn to a second major component of the structure function determination, the unsmearing calculation and the Monte Carlo used to perform it. In general terms the CARLO program used in this analysis is an excellent description of both the neutrino and antineutrino data samples. In the region of low W^2, however, which implies high x and low Q^2, the hadron final state is dominated by resonance production and decay, and overlap occurs of the elastic and inelastic event sample due to nuclear reinteraction processes. It has been observed that the CARLO program has difficulty in accurately modelling event topology distributions in this region, with subsequently large uncertainties in unsmearing factors and the elastic and inelastic structure functions. Whilst a study of the details of the reinteraction model and better tuning of this model to the observed multiplicity distributions could lead to improvements, it would seem that a major step towards reproducing the observed event distributions in this region would follow from the inclusion of the $\Delta(1232)$ resonances in the CARLO program, which form the dominant exclusive channels in this region. Unfortunately with regard to the high x region in general ($x > 0.8$), which could give in theory the best indication of the level of scaling violation,

unsmearing factors must remain large and consequently rather unreliable. Fermi motion effects aside, this problem of determination of structure functions at high x is essentially a resolution problem and not related to the particular Monte Carlo used.

The next point to be considered concerns assumptions made in the extraction of F_2 and xF_3, notably the value of $R = \sigma_s/\sigma_T$, which relates the structure functions F_2 and $2xF_1$ through equation (5.3). In the present analysis it was assumed that $R = 0$, with the sensitivity to this choice checked by looking at the alternative assumptions $R = 0.1$ and $R = 4m^2x^2/Q^2$ (the quark-parton model prediction). Since this quantity has not been measured in a dedicated experiment, such determinations of it as exist have large uncertainties. Different experiments obtain different estimates of the x dependence of R [44], those at high Q^2 tending to agree with the form predicted by QCD and those at lower Q^2 tending to obtain larger values. To the author's knowledge R has not been measured precisely as a function of x and Q^2. Clearly the situation must benefit from better experimental measurements of this quantity.

Whilst unable to provide a precise measurement, it is possible that the present experiment may be able to extract some information on the value of R, by utilising the y information of the events, which has been ignored in the work presented in this thesis. Consider equation (5.4) for the differential cross sections. Dividing both sides of this equation by the neutrino energy E and expressing the result in terms of the independent variables x, Q^2 and y gives

$$\frac{d^2\sigma^{\nu,\bar{\nu}}}{dxdy} = \frac{G^2mE}{\pi}\left(\frac{{m_W}^2}{{m_W}^2+Q^2}\right)^2 \times \left\{F_2(x,Q^2)\left[1-y+\left(\frac{(1+4m^2x^2/Q^2)}{(1+R(x,Q^2))}-\frac{2m^2x^2}{Q^2}\right)\frac{y^2}{2}\right] \pm xF_3(x,Q^2)y\left(1-\frac{y}{2}\right)\right\} \tag{7.1}$$

where a possible dependence of R on x and Q^2 has been indicated. By addition and subtraction of the two equations given by (7.1) the following combinations are obtained

$$\frac{1}{2E}\left\{\frac{d^2\sigma^{\nu}}{dxdy}+\frac{d^2\sigma^{\bar{\nu}}}{dxdy}\right\} = \frac{G^2m}{\pi}\left(\frac{{m_W}^2}{{m_W}^2+Q^2}\right)^2 \times F_2(x,Q^2)\left\{1-y+\left[\frac{(1+4m^2x^2/Q^2)}{(1+R(x,Q^2))}-\frac{2m^2x^2}{Q^2}\right]\frac{y^2}{2}\right\} \tag{7.2}$$

$$\frac{1}{2E}\left\{\frac{d^2\sigma^{\nu}}{dxdy}-\frac{d^2\sigma^{\bar{\nu}}}{dxdy}\right\} = \frac{G^2m}{\pi}\left(\frac{{m_W}^2}{{m_W}^2+Q^2}\right)^2 xF_3(x,Q^2)y\left(1-\frac{y}{2}\right) \tag{7.3}$$

If the neutrino and antineutrino data is binned in the variables x, Q^2 and y, the left hand side of equations (7.2) and (7.3) is calculable in terms of the observed event distributions in these variables and the flux. In a chosen bin of x and Q^2, the y distributions thus obtained can be fitted with a functional form in y given by the right hand side of these equations, with the parameters of the fit being $F_2(x,Q^2)$ and $R(x,Q^2)$ in the case of equation (7.2) and $xF_3(x,Q^2)$ in the case of equation (7.3). This clearly represents an alternative method of extracting the structure functions F_2 and xF_3, in addition to estimating $R(x,Q^2)$. It suffers from the practical difficulties of a more complicated unsmearing problem in terms of three variables x, Q^2 and y, and the limitation of the technique to the low x and high Q^2 region of the kinematic plane. At high x and low Q^2, due to the lower limit on the neutrino energy in the present experiment, the y distribution of events is restricted to low values of y and no fit is possible. A method of investigation of the Callan–Gross relation similar to that described above has been employed in fairly coarse bins of x and Q^2 by the WA47/GGM collaboration in reference [3].

We now come to considering the second step identified above, the interpretation of the measured structure functions. In Chapter 6 a preliminary study of the evolution equation technique of fitting to the structure functions F_2 and xF_3 with the form of scaling violation predicted by perturbative QCD was discussed. It was found that above Q^2 of 2 $\mathrm{GeV^2/c^2}$, qualitative agreement with the QCD predictions could be observed, and a value of $\Lambda_{\overline{MS}}$ extracted from the data. However, this is not the only method of testing QCD, and it is essential that a moments analysis of the structure functions be performed in addition to the evolution equation study, and the results of the two analyses compared. The moments of F_2 and xF_3 from the present experiment were calculated in section 6.4, and may form a starting point for such an analysis.

The problem which has not been addressed in this thesis is that of alternative explanations to perturbative QCD for the scaling violations observed in the structure functions. Although it is relatively straightforward to demonstrate that the shape of the observed structure functions is consistent with QCD predictions, it is less straighforward to demonstrate that the shape is consistent only with QCD. A likely candidate for alternative

explanations for scaling violation is so–called "higher twist". Higher twist is a collective term for a variety of non–perturbative coherent effects such as di–quark scattering, resonance production, elastic scattering and transverse momentum of quarks. These effects are not calculable within our present knowledge of strong interaction dynamics, although they are expected to break scaling in the form of a power series in $1/Q^2$. They are therefore predicted to be most important at low Q^2 and at high x (although the exact x dependence is unknown). The form for xF_3 given in equation (6.15) is expected in the presence of higher twist effects to take the form [21]

$$xF_3(x,Q_0^2) = Ax^{\alpha}(1-x)^{\beta}\left[1+\sum_{j=1}^{\infty}\left(\frac{\mu_j^2}{Q_0^2(1-x)}\right)^j\right] \tag{7.4}$$

while moments as specified in equation (1.29) would now take the form

$$M_3^n(Q^2) = \frac{C}{\ln(Q^2/\Lambda^2)^{d_n}}\left[1+\sum_{j=1}^{\infty}\left(\frac{\mu_j^2 n}{Q^2}\right)^j A_j\right] \tag{7.5}$$

Here the magnitude of μ_j is unknown, and A_j is a function of $\ln Q^2/\Lambda^2$. The method of attack for looking for higher twist contributions follows from equations of the form of (7.4) and (7.5). In the case of a moments analysis, instead of fitting to the moments with equation (1.29), one truncates equation (7.5) at the first term (the "twist 4" term) in the series and fits to the form

$$M_3^n(Q^2) = A_n\left[1+\frac{nC_T(n)}{Q^2}\right] \tag{7.6}$$

where we have used the notation of the WA47/GGM collaboration [25], who have performed such fits. A_n can be a constant if fitting purely higher twist, or the QCD prediction for M_3^n if fitting a combination of perturbative QCD and higher twist. $C_T(n)$ is a parameter to be determined by the fit, and sets the magnitude and sign of the higher twist contribution. For a direct analysis, a fit is performed with a form for $xF_3(x,Q_0^2)$ of, for example

$$xF_3(x,Q_0^2) = Ax^{\alpha}(1-x)^{\beta}\left[1+\frac{Cx}{(1-x)Q_0^2}\right] \tag{7.7}$$

with C an extra parameter to be determined by the fit.

The reason for discussing higher twist in some detail here is that the WA59 experiment was in part proposed to study this very problem. The two previous bubble chamber

structure function analyses mentioned in this thesis, those of the WA47/GGM collaboration and the GGM/SPS collaboration have both studied higher twist contributions to their data by performing non–singlet fits to the structure functions with a form given by equation (7.7) for the boundary condition at $Q^2 = Q_0^2$ [25] [51]. The two analyses arrive at opposite signs for the parameter C in equation (7.7). This has the consequence that the value of Λ that is obtained from such a fit increases as Q_0^2 is lowered for C positive (WA47/GGM analysis) and decreases as Q_0^2 is lowered for C negative (GGM/SPS analysis). In principle the WA59 experiment can perform the same analysis without the need to combine data sets from two experiments, and with increased statistics. The ability to achieve this would benefit from reducing the minimum Q^2 considered below the 2 GeV^2/c^2 that has been considered "safe" in the present analysis, in order to become more sensitive to the higher twist contributions. However, it is felt that the systematic uncertainties in the structure functions at low Q^2 and high x that were discussed in Chapter 5 preclude such an extension at this time, until the systematics in this region are better understood.

The present data set is very likely the last to be obtained from neutrino scattering from an isoscalar target suitable for a structure function analysis of the type discussed here, and it is important to learn as much as possible from it. It appears clear from the present study, however, that the advantages obtained in performing a bubble chamber neutrino experiment such as the present one with increased statistics are offset by the entering of a domain in which systematic effects become more important than statistical ones, a somewhat novel situation in neutrino bubble chamber physics. Whether this new domain severely limits the ability of the present data set to address the questions for which it was designed remains to be discovered.

LIST OF WA59 PUBLICATIONS

P. Marage et al.,
Study of μe Events Produced in Antineutrino Interactions
Zeitschrift fur Physik **C21** (1984) 307.

P. Marage et al.,
Observation of Coherent Diffractive Charged Current Interactions of Antineutrinos on Neon Nuclei
Physics Letters **140B** (1984) 137.

A.M. Cooper et al.,
An Investigation of the EMC Effect Using Antineutrino Interactions in Deuterium and Neon
Physics Letters **141B** (1984) 133.

G. Gerbier et al.,
Dilepton and Trilepton Production by Antineutrinos and Neutrinos in Neon
To be published in Zeitschrift fur Physik **C**

REFERENCES

[1] S.L. Glashow, Nucl. Phys. **22** (1961) 579.
S. Weinberg, Phys. Rev. Lett. **19** (1967) 1264.
A. Salam, in "Elementary Particle Theory", ed. N. Svartholm (Stockholm: Almqvist, Forlag A.B.) 1968, p.367.

[2] R.P. Feynman, Photon Hadron Interactions (Benjamin, New York, 1972).

[3] P.C. Bosetti et al., Nucl. Phys. **B142** (1978) 1.

[4] J. Morfin et al., Phys. Lett. **104B** (1981) 235.

[5] H. Abramowicz et al., Z. Phys. **C17** (1983) 283.

[6] F. Bergsma et al., Phys. Lett. **123B** (1983) 269.

[7] D.B. MacFarlane et al., Z. Phys. **C26** (1984) 1.

[8] F. Close, An Introduction to Quarks and Partons (Academic Press, London, 1979).

[9] J.D. Bjorken, Phys. Rev. **179** (1969) 1547.

[10] D.G. Gross and C.H. Llewellyn Smith, Nucl. Phys. **B14** (1969) 337.

[11] C.G. Callan and D.G. Gross, Phys. Rev. Lett. **21** (1968) 211.

[12] Particle Data Group. Rev. Mod. Phys. **56** No. 2 Part II. April 1984.

[13] T. Bolognese et al., Phys. Rev. Lett. **50** (1983) 224.

[14] T. Eichten et al., Phys. Lett. **46B** (1973) 274.

[15] See for example, A.J. Buras, Rev. Mod. Phys. **52** (1980) 199.

[16] E.M. Riordan et al., SLAC-PUB-1634 (1975).

[17] Y. Watanabe et al., Phys. Rev. Lett. **35** (1975) 898.

[18] J.M. Cornwall and R.E. Norton, Phys. Rev. **177** (1969) 2584.

[19] A.J. Buras and K.J.F. Gaemers, Nucl. Phys. **B132** (1978) 249.

[20] G. Altarelli and G. Parisi, Nucl. Phys. **B126** (1977) 298.

[21] L.F. Abbott and R. Michael Barnett, Ann. of Phys. **125** (1980) 276.

[22] K. G. Wilson, Phys. Rev. **179** (1969) 1499.

[23] H. Georgi and H.D. Politzer, Phys. Rev. Lett. **36** (1976) 1281.

[24] O. Nachtmann, Nucl. Phys. **B63** (1973) 237; **B78** (1974) 455.

[25] P.C. Bosetti et al., Nucl. Phys. **B203** (1982) 362.

[26] J.J. Aubert et al., Phys. Lett. **123B** (1983) 275.

[27] R.G. Arnold et al., Phys. Rev. Lett. **52** (1984) 727.

[28] A.M. Cooper et al., Phys. Lett. **141B** (1984) 133.

[29] R. Giles, Ph. D. Thesis, Oxford University, 1981.

[30] E. Heijne, CERN Yellow Report 83-06.

[31] C. Brand et al., Nucl. Instr. and Meth. **136** (1976) 485.
R. Beuselinck et al., Nucl. Instr. and Meth. **154** (1978) 445.

[32] R.A. Sansum, Private Communication.

[33] S.E. Derenzo and R.H. Hildebrand, Nucl. Instr. and Meth. **69** (1969) 287.

[34] G. Myatt, CERN/ECFA/72-4 Vol. II (1972) p.117.

[35] D.C. Colley et al., Z. Phys. **C2** (1979) 187.

[36] P. Kasper, WA59 internal note.

[37] D.H. Perkins, P.Schreiner and W.G. Scott, Phys. Lett. **67B** (1977) 347.

[38] A. De Rújula, R. Petronzio and A. Savoy-Navarro,
Nucl. Phys. **B154** (1979) 394.

[39] W.G. Scott, CERN/EP/NPC/N 82-1.

[40] A. Bodek and J.L. Ritchie, Phys. Rev. **D23** (1981) 1070; **D24** (1981) 1400.

[41] A.M. Cooper-Sarkar, Private Communication.

[42] H. Wachtsmuth, Private Communication.

[43] CDHS Collaboration, Contribution to International Europhysics
Conference on High Energy Physics, Bari, July 1985.

[44] J. Colas, Proceedings of the International Europhysics Conference
on High Energy Physics, Brighton, July 1983.
(Rutherford Appleton Laboratory) p.461.

[45] A. Bodek, Proceedings of the XIth International Conference on Neutrino
Physics and Astrophysics at Nordkirchen near Dortmund, 1984
(World Scientific) p.643.

[46] P.E. Bosted, Proceedings of the Nineteenth Recontre de Moriond 1984,
Vol. 2 (ed. J. Tran Thanh Van), p.601.

[47] C.H. Llewellyn-Smith, Phys. Rep. **C3** (1972) 263.

[48] D.W.Duke and R.G. Roberts, Nucl. Phys. **B166** (1980) 243.

[49] A. Devoto, D.W. Duke, J.F. Owens and R.G. Roberts, Phys. Rev. **D27** (1983) 508.

[50] M. Bacé, Phys. Lett. **78B** (1978) 132.

[51] J.G. Morfin et al., Phys. Lett. **107B** (1981) 450.